FOURIER TRANSFORM MICROWAVE SPECTROSCOPY OF SOME METAL-CONTAINING COMPOUNDS PRODUCED BY LASER ABLATION

By

Kaley Anne Walker

B. Sc. (Chemistry) University of Waterloo

A THESIS SUBMITTED IN PARTIAL FULFILLMENT OF

THE REQUIREMENTS FOR THE DEGREE OF

DOCTOR OF PHILOSOPHY

IN

THE FACULTY OF GRADUATE STUDIES

CHEMISTRY

We accept this thesis as conforming

to the required standard

THE UNIVERSITY OF BRITISH COLUMBIA

1998

In presenting this thesis in partial fulfilment of the requirements for an advanced degree at the University of British Columbia, I agree that the Library shall make it freely available for reference and study. I further agree that permission for extensive copying of this thesis for scholarly purposes may be granted by the head of my department or by his or her representatives. It is understood that copying or publication of this thesis for financial gain shall not be allowed without my written permission.

Chemistry
The University of British Columbia
2075 Wesbrook Place
Vancouver, Canada
V6T 1Z1

Date:

January 20 1998.

Abstract

A laser ablation source has been constructed for a pulsed jet cavity Fourier transform microwave (FTMW) spectrometer. This source is mounted in one of the microwave cavity mirrors and includes a mechanism for rotating and translating the target metal rod. Seven metal-containing species, namely MgS, MgBr, AlBr, MgNC, AlNC, YF and YBr, have been prepared using this apparatus and their pure rotational spectra have been measured by FTMW spectroscopy.

The first laser ablation-FTMW measurement of a metal sulfide, MgS, has been made. The $J = 1 - 0$ transition near 16 GHz has been measured for 4 isotopomers in the ground vibrational state, as well as for the main isotopomer in the first excited vibrational state. ^{25}Mg nuclear hyperfine structure has been observed and the nuclear quadrupole coupling constant has been determined.

The pure rotational spectra of magnesium monobromide and aluminium monobromide have been measured between 9.3 and 20.1 GHz. For MgBr, this is the first report of such a spectrum. Rotational, fine structure and several Br hyperfine parameters have been obtained for this radical and an accurate equilibrium bond length has been determined. From the nuclear quadrupole and magnetic hyperfine constants MgBr has been found to be highly ionic, with the unpaired electron residing almost entirely on Mg. For AlBr, accurate hyperfine parameters have been obtained, including the first values for the Al^{81}Br isotopomer. These, too, are consistent with highly ionic bonding. The calculated ionic characters follow trends predicted from electronegativity values: MgBr

exhibits more covalent character than Ca and heavier alkaline earth monobromide species and AlBr shows less covalent character than GaBr.

Pure rotational spectra of aluminium isocyanide and magnesium isocyanide have been measured in the frequency range 11.9 - 23.9 GHz. The hyperfine structure in MgNC caused by the ^{14}N nucleus has been measured and the nuclear quadrupole coupling, Fermi contact and dipole-dipole interaction constants have been obtained. From the measured transitions of AlNC, nuclear quadrupole coupling constants and nuclear spin-rotation constants have been determined for both the ^{14}N and the ^{27}Al nuclei along with an Al-N nuclear spin-spin constant. The degree of *sp*-hybridisation of the bonding orbitals of AlNC and MgNC have been estimated from the nuclear quadrupole coupling constants. Comparisons have been made to similar linear metal isocyanide and metal monohalide species.

The first high resolution spectrum of yttrium monobromide has been measured between 7.4 and 22.5 GHz. In addition, nuclear spin-rotation splitting has been observed in the spectrum of yttrium monofluoride. Equilibrium rotational parameters have been determined for YBr and used to calculate an equilibrium bond distance. Hyperfine structure due to the bromine nuclei has been observed and nuclear quadrupole and nuclear spin-rotation constants have been determined. From them, YBr has been found to be highly ionic and very similar in behaviour to the alkali metal bromide species. The FTMW results for YF have been combined with data from other pure rotational studies to determine the nuclear spin rotation constant.

Contents

List of Tables

List of Figures

Acknowledgement

I would like to thank my research supervisor Mike Gerry for his patience and encouragement during the past five years. I would also like to thank my co-workers for their assistance. I thank Wolfgang Jäger, Yunjie Xu and Kristine Hensel for teaching me how to use the spectrometer, Mark Barnes and Thomas Brupbacher for many, many discussions during the construction and testing of the laser ablation system, Holger Müller for answering my Pickett questions, and Jürgen Preußer for attempting to improve my German pronunciation. I would like to thank Beth Gatehouse for being my friend and partner in crime (and leak detecting) for the last five years. Thank you also to Peggy Athanassenas, Dave Gillett, Chris Kingston, Greg Metha, and Jim Peers.

I also wish thank my friends and family far and near for their support during this thesis work. Specifically, I would like to thank Kate McInturff, Meredith Browne and Mark Salter for taking me to the movies, keeping me in touch with the world outside of science and trying to convince me that "there is a law that says: you can only be in the lab for 12 hours per day". I would like to thank Almira Blazek for many fabulous theatre outings. Thank you also to Sean Walker and Taunya Boughtflower for going to see some very bad films and making sure that I remembered to eat. Finally, I would like to thank my parents for their support, understanding and encouragement throughout the years.

This thesis is dedicated to

Dr. E. E. W. Walker

(1888-1978)

Chapter 1

Introduction

Microwave spectroscopy is primarily the study of pure rotational transitions of gas phase molecules possessing permanent dipole moments. The development of sources and detectors for microwave radar during World War II made possible the beginning of microwave spectroscopy. As the field has grown over the past fifty years, many molecules have been characterised *via* their microwave spectra [1–3]. Radioastronomical observations have identified, *via* their microwave spectra, many species present in interstellar space and have contributed to the understanding of interstellar chemistry [4–7].

The development of pulsed jet cavity Fourier transform microwave (FTMW) spectroscopy over the past two decades has improved the sensitivity and resolution possible in microwave measurements [8–10]. The spectra of reactive or otherwise unstable molecules can be measured because the pulsed jet expansion stabilises transient species. Narrow line widths are obtained in these experiments and the resolution is, thus, very high. The very precise rotational constants obtained can provide accurate molecular geometries. Nuclear hyperfine structure, including very small hyperfine contributions caused by nuclear spin-rotation and spin-spin interactions, can easily be resolved by this technique.

Hyperfine interactions provide detailed information about the electronic structures of molecules. One of the major contributions to these interactions is nuclear quadrupole

coupling. This has been used to investigate bonding in many molecules [2] by providing a method of probing the electric field gradients in the molecule. In the spectra of paramagnetic molecules, a second major contribution is magnetic hyperfine coupling between the spin of the unpaired electron(s) and the nuclear spin(s) in the molecule. From this coupling, the unpaired electron spin density in the molecule can be probed [11,12]. The information obtained can be used to draw conclusions about the bonding in the species under investigation.

In this thesis, pure rotational spectra of several diatomic and linear triatomic metal-containing molecules are presented. From these spectra, geometries have been calculated and bond characteristics have been investigated through the hyperfine parameters. Gas phase samples of the species of interest were prepared using a newly built laser ablation source and their spectra were measured by FTMW spectroscopy. The laser ablation apparatus is mounted in one of the FTMW cavity mirrors and incorporates a mechanism for translating and rotating the target metal rod. The development of this system is described in Chapter 4.

The laser ablation apparatus was tested by measuring the spectra of four isotopomers of magnesium sulfide, including species of low abundance. These experiments, described in Chapter 5, are the first FTMW measurement of the spectrum of a metal sulfide produced by reacting ablated metal with a source of sulfur. An equilibrium bond length has been obtained for MgS along with the ^{25}Mg nuclear quadrupole coupling constant.

Chapter 6 describes the pure rotational spectroscopy of magnesium monobromide and aluminium monobromide. For MgBr, this represents the first complete rotational analysis. Accurate rotational and centrifugal distortion constants have been determined as well as new fine and hyperfine parameters. In addition, an accurate equilibrium bond length has been obtained. For AlBr, the nuclear quadrupole structure in the spectrum

of the ^{81}Br isotopomer has been observed for the first time. As well, improved nuclear quadrupole coupling constants have been obtained for Al^{79}Br and nuclear spin-rotation and spin-spin constants have been determined for both isotopomers. The bonding in magnesium and aluminium monobromide has been found to follow the trends predicted from electronegativities; MgBr exhibits more covalent character than the corresponding Ca and heavier alkaline earth monobromides and AlBr exhibits less covalent character than GaBr.

The FTMW spectra of aluminium isocyanide and magnesium isocyanide are discussed in Chapter 7. This is the first measurement of the hyperfine interactions in these molecules. The FTMW results obtained for MgNC were combined with those of an earlier millimetre wave study to determine an improved set of rotational constants. Nuclear quadrupole and magnetic hyperfine parameters have been determined for AlNC and MgNC. From the nuclear quadrupole coupling constants, the *sp*-hybridisation of the bonding orbitals of both molecules has been investigated. Similarities in the bond properties of aluminium and magnesium isocyanide have been found with those of other linear metal isocyanides and metal monohalides.

Chapter 8 describes the pure rotational spectroscopy of two yttrium monohalide molecules, YBr and YF. For the former, this work is the first high resolution spectroscopic study of any kind. Rotational and centrifugal distortion constants have been determined and an accurate equilibrium bond length has been calculated. The vibration frequency of YBr has been estimated and has been found to agree well with results obtained by low resolution laser induced fluorescence spectroscopy. The ionic character of the Y-Br bond has been estimated from the Br nuclear quadrupole coupling constant; it has been found to be very similar to that of the alkali metal bromide species. Nuclear spin-rotation splitting has been measured in the spectrum of yttrium monofluoride.

The ^{19}F spin-rotation coupling constant has been determined by combining the FTMW results with the results from other pure rotational studies.

To aid the reader, the tables of data and results are collected at the end of every chapter. The figures, however, are located in the body of the text near where they are first cited.

Chapter 2

Theory

This chapter outlines the theory pertinent to the spectral assignment and analysis of the microwave spectra of the diatomic and linear triatomic molecules described in this thesis. The Hamiltonian appropriate for these systems is

$$\hat{H} = \hat{H}_{\text{rot}} + \hat{H}_{\text{distort}} + \hat{H}_{\text{fine}} + \hat{H}_{\text{hyperfine}} \tag{2.1}$$

where $\hat{H}_{\text{rot}}$, $\hat{H}_{\text{distort}}$, $\hat{H}_{\text{fine}}$ and $\hat{H}_{\text{hyperfine}}$ are the rotational, centrifugal distortion, fine and hyperfine Hamiltonians. Each of these contributions is discussed separately. A through treatment of pure rotational spectroscopy is available from several standard textbooks [1, 2, 13]. The calculation of bond distances from rotational constants and the interpretation of hyperfine parameters are also discussed in this chapter.

2.1 Molecular Rotation

2.1.1 Rigid Rotor Approximation

The gross features of the rotational spectrum of a molecule can be described by the rigid rotor model. The general rigid rotor Hamiltonian is given as:

$$\hat{H}_{\text{rot}} = B_x \hat{R}_x^2 + B_y \hat{R}_y^2 + B_z \hat{R}_z^2 \tag{2.2}$$

where x, y, and z are the principal inertial axes of the molecule and $\hat{R}_g$ $(g = x, y, z)$ are the components of the rotational angular momentum about each of the principal axes. The molecular rotational constants, B_g are related to the moments of inertia, I_g, by

$$B_g = \frac{h}{8\pi^2 I_g}. \tag{2.3}$$

For linear molecules the z-axis is taken to be along the molecular bond axis. There is no rotational angular momentum about this axis and the moments of inertia about the other two axes are equal($I_z = 0$ and $I_x = I_y = I$). Thus the rigid rotor Hamiltonian for a linear molecule can be expressed as

$$\hat{H}_{rot} = B(\hat{R}_x^2 + \hat{R}_y^2) \tag{2.4}$$

$$= B\mathbf{R^2} \tag{2.5}$$

where $B_x = B_y = B$. The rotational energy levels obtained from this equation are, in frequency units,

$$E_{rot} = BR(R+1) \tag{2.6}$$

where R is the rotational quantum number.

2.1.2 Selection Rules

Pure rotational transitions are induced by the interaction of electromagnetic radiation with the permanent electric dipole moment of a molecule, μ. The probability of a transition from one state $|RM\rangle$ to another state $|R'M'\rangle$ in unit time, $p_{RM\rightarrow R'M'}$, is

$$p_{RM\rightarrow R'M'} = \rho(\nu_{RMR'M'})B_{RM\rightarrow R'M'} \tag{2.7}$$

where $\rho(\nu_{RMR'M'})$ is the density of radiation oscillating with frequency $\nu_{RMR'M'}$ and $B_{RM\rightarrow R'M'}$ is the Einstein coefficient of absorption for the $|RM\rangle \rightarrow |R'M'\rangle$ transition.

In microwave experiments, plane polarised radiation is used which is arbitrarily chosen to be polarised along the space-fixed Z-axis, hence

$$B_{RM\rightarrow R'M'} = \left(\frac{8\pi^3}{3h^2}\right)|\langle RM|\mu_Z|R'M'\rangle|^2. \quad (2.8)$$

The matrix element of μ_Z has to be non-zero for a transition to occur. The molecule-fixed components of the molecular dipole moment, μ_x, μ_y and μ_z, are related to the space-fixed component μ_Z by the direction cosines, Φ_{Zg},

$$\mu_Z = \mu_x\Phi_{Zx} + \mu_y\Phi_{Zy} + \mu_z\Phi_{Zz}. \quad (2.9)$$

In the diatomic and linear triatomic molecules considered here, the permanent electric dipole lies along the z axis, so $\mu_x = \mu_y = 0$ and therefore

$$\langle RM|\mu_Z|R'M'\rangle = \mu_z\langle RM|\Phi_{Zz}|R'M'\rangle. \quad (2.10)$$

Non-zero direction cosine matrix elements are tabulated in Ref. 2 and from these the rotational selection rules for these linear species are found to be

$$\Delta R = \pm 1 \quad (2.11)$$

$$\Delta M = 0. \quad (2.12)$$

2.1.3 Vibrating Rotor

The rigid rotor approximation provides a general description of the molecular rotational energy levels. However molecules are not rigidly bound; the bonds are flexible. Two contributions to the rotational energies result from these molecular vibrations. As the molecule rotates, it distorts as a result of centrifugal distortion. In addition, the rotational constant decreases with vibrational excitation because of vibration-rotation interaction effects [14, 15].

The centrifugal distortion Hamiltonian for a linear molecule is

$$\hat{H}_{\text{distort}} = -D(\mathbf{R}^2)^2 + H(\mathbf{R}^2)^3 + ... \tag{2.13}$$

where D and H are the quartic and sextic centrifugal distortion constants, respectively, and $\mathbf{R}$ is the rotational angular momentum operator. Combining the rotational and centrifugal distortion Hamiltonians

$$\hat{H}_{\text{vib-rot}} = \hat{H}_{\text{rot}} + \hat{H}_{\text{distort}} \tag{2.14}$$

the vibration-rotation Hamiltonian results. The vibration-rotation energy expression is given as

$$E_{\text{vib-rot}} = B_v R(R+1) - D_v R^2(R+1)^2 \tag{2.15}$$

where B_v and D_v are the rotational and quartic centrifugal distortion constants, respectively, for the vth vibrational state and R and v are the rotational and vibrational quantum numbers, respectively. The energy expression is truncated following the quartic centrifugal distortion constant because higher order distortion constants were not required to fit the data obtained in these studies.

The vibrational dependence of the rotational and centrifugal distortion constants is due to vibration-rotation interaction. For a diatomic molecule, this is given by

$$B_v = B_e - \alpha_e\left(v+\frac{1}{2}\right) + \gamma_e\left(v+\frac{1}{2}\right)^2 + ... \tag{2.16}$$

$$D_v = D_e + \beta_e\left(v+\frac{1}{2}\right) + ... \tag{2.17}$$

In these equations, α_e, γ_e and β_e are vibration-rotation interaction constants and B_e and D_e are the equilibrium rotational and centrifugal distortion constants, respectively. These are the values of these parameters at the minimum of the potential energy surface. To calculate these constants, rotational transitions must be measured in at least two

vibrational states. Measurements were made in the ground and first excited vibrational states for four diatomic species discussed in this thesis and from these data B_e and α_e were determined. Equilibrium constants were not determined for the two linear triatomic species studied because transitions were measured in the ground vibrational state only. Vibration-rotation effects in the centrifugal distortion constant were found to be smaller than the uncertainty in the determined parameter.

The rotational energy expression for a linear triatomic molecule is identical to Eq. (2.15). In this case, however, the vibrational dependence of the rotational and centrifugal distortion constants must include contributions from each of the vibrational modes of the molecule. Thus, the expressions are

$$B_v = B_e - \sum_i \alpha_i \left(v_i + \frac{d_i}{2} \right) \tag{2.18}$$

$$D_v = D_e + \sum_i \beta_i \left(v_i + \frac{d_i}{2} \right) \tag{2.19}$$

where v_i is the vibrational quantum number of the ith vibrational mode, d_i is the degeneracy and α_i and β_i are the vibration-rotation interaction constants for the ith vibrational mode.

2.1.4 Rotational Quantum Numbers

So far in the discussion of rotational energy levels, the rotational angular momentum **R** has been used. This has been done to simplify the initial discussion. At this point, the coupling of electronic and rotational angular momenta will be brought into the picture. **R** is the rotational angular momentum of the molecule which can couple to the electron orbital angular momentum **L** to produce **N**. Then rotational angular momentum including **L** can couple with the electron spin angular momentum **S** to produce **J**, the total rotational angular momentum excluding nuclear spin angular momentum. This scheme

can be expressed as

$$\mathbf{R} + \mathbf{L} = \mathbf{N} \tag{2.20}$$

$$\mathbf{N} + \mathbf{S} = \mathbf{J}. \tag{2.21}$$

All the molecules investigated in this work have Σ ground electronic states, for which there is no electron orbital angular momentum, so $\Lambda = 0$, and thus, $N \equiv R$. Also most are diamagnetic species, with $S = 0$, so $N \equiv J$ and thus the rotational energy expression is

$$E_{\text{vib-rot}} = B_v J(J+1) - D_v J^2(J+1)^2 \tag{2.22}$$

and the selection rules are $\Delta J = \pm 1$.

Two of the molecules studied are paramagnetic; these have $^2\Sigma^+$ ground electronic states. Since $S = \frac{1}{2}$, $N \neq J$ and the rotational energy expression for these species is

$$E_{\text{vib-rot}} = B_v N(N+1) - D_v N^2(N+1)^2. \tag{2.23}$$

The selection rules are $\Delta N = \pm 1$ and $\Delta J = 0, \pm 1$.

2.2 Fine Structure

2.2.1 Electron Spin-Rotation Coupling

For molecules having $^2\Sigma^+$ ground electronic states, an electron spin-rotation term must also be added to the vibration-rotation Hamiltonian. The unpaired electron spin interacts with the magnetic field generated by the rotation of the molecule giving rise to fine structure in the spectrum. The Hamiltonian for this interaction is

$$\hat{H}_{\text{fine}} = \gamma_v \mathbf{N} \cdot \mathbf{S} \tag{2.24}$$

where γ_v is the electron spin-rotation constant for the vth vibrational state. This doubles each of the molecular rotational levels, so $J = N \pm \frac{1}{2}$ for $N > 0$. The resulting vibration-rotation energy expressions, including fine structure, are

$$E_{\text{vib-rot}}\left(J = N + \frac{1}{2}\right) = B_v N(N+1) - D_v N^2(N+1)^2 + \frac{\gamma_v}{2}N \quad (2.25)$$

$$E_{\text{vib-rot}}\left(J = N - \frac{1}{2}\right) = B_v N(N+1) - D_v N^2(N+1)^2 - \frac{\gamma_v}{2}(N+1). \quad (2.26)$$

2.3 Nuclear Hyperfine Structure

Interactions involving nuclear spin angular momentum, **I**, are referred to as hyperfine interactions. The nuclear spin angular momentum can couple to the total rotational angular momentum, **J**, to form **F**, the total angular momentum,

$$\mathbf{I} + \mathbf{J} = \mathbf{F}. \quad (2.27)$$

For molecules with two nuclei having non-zero spin, two coupling schemes are possible. If the coupling energies of the two nuclei are equal or nearly so, then the "parallel" scheme is employed; the two nuclear spins couple to form a resultant nuclear spin angular momentum, **I**, which then couples to **J**,

$$\mathbf{I_1} + \mathbf{I_2} = \mathbf{I} \quad (2.28)$$

$$\mathbf{I} + \mathbf{J} = \mathbf{F}. \quad (2.29)$$

The "series" scheme is employed if the coupling energy of one nucleus is much greater than that of the other. The first nuclear spin, $\mathbf{I_1}$, couples to **J** to form the intermediate $\mathbf{F_1}$; then the second nuclear spin, $\mathbf{I_2}$, couples to $\mathbf{F_1}$,

$$\mathbf{I_1} + \mathbf{J} = \mathbf{F_1} \quad (2.30)$$

$$\mathbf{I_2} + \mathbf{F_1} = \mathbf{F}. \quad (2.31)$$

The "series" scheme best describes the hyperfine interactions observed for the metal-containing species with two magnetic nuclei studied in this thesis.

Nuclear hyperfine interactions occur *via* electrostatic and magnetic means. The observed hyperfine structure can be classified into three types,

$$\hat{H}_{\text{hyperfine}} = \hat{H}_{\text{quadrupole}} + \hat{H}_{\text{spin-rotation}} + \hat{H}_{\text{spin-spin}} \tag{2.32}$$

where $\hat{H}_{\text{quadrupole}}$ describes the nuclear electric quadrupole interaction and $\hat{H}_{\text{spin-rotation}}$ and $\hat{H}_{\text{spin-spin}}$ describe the magnetic nuclear spin-rotation and spin-spin interactions, respectively.

2.3.1 Nuclear Quadrupole Coupling

Nuclear quadrupole hyperfine structure arises from the interaction of a nuclear electric quadrupole moment with the electric field gradient at that nucleus. The nucleus must have a spin, $I \geq 1$, to possess a nuclear quadrupole moment.

The Hamiltonian for the nuclear quadrupole coupling of a single quadrupolar nucleus can be written as the product of two second rank tensors,

$$\hat{H}_{\text{quadrupole}} = -\frac{1}{6}\mathbf{Q} : \nabla\mathbf{E} \tag{2.33}$$

$$= \frac{1}{6}\sum_{i,j=x,y,z} Q_{i,j}V_{i,j} \tag{2.34}$$

where $\mathbf{Q}$ and $\nabla\mathbf{E}$ are the nuclear electric quadrupole moment and electric field gradient tensors, respectively, and $V_{i,j} = -\nabla E_{i,j}$. For a diamagnetic molecule, the matrix elements of this Hamiltonian are given by [2]

$$\langle J'IF|\hat{H}_{\text{quadrupole}}|JIF\rangle = \frac{(-1)^{J+I+F}}{4}\begin{Bmatrix} F & I & J' \\ 2 & J & I \end{Bmatrix} \times \begin{pmatrix} J & 2 & J' \\ J & 0 & -J \end{pmatrix}^{-1} \begin{pmatrix} I & 2 & I \\ -I & 0 & I \end{pmatrix}^{-1} eQq_{J'J} \tag{2.35}$$

where the $6j$ and $3j$ symbols can be evaluated using formulae given in Ref. 16. $eQq_{J'J}$ are the nuclear quadrupole coupling constants in the space fixed axis system; these are transformed into the molecule fixed system by [2]

$$\begin{aligned} eQq_{J'J} &= (-1)^J [(2J+1)(2J'+1)]^{\frac{1}{2}} \\ &\times \begin{pmatrix} J & 2 & J' \\ J & 0 & -J \end{pmatrix} \begin{pmatrix} J & 2 & J' \\ 0 & 0 & 0 \end{pmatrix} eQq_0 \end{aligned} \tag{2.36}$$

where eQq_0 is the molecular nuclear quadrupole coupling constant.

The matrix elements for the nuclear quadrupole interaction in a linear paramagnetic molecule in a $^2\Sigma$ state can be calculated from [12]

$$\begin{aligned} \langle N'SJ'IF|\hat{H}_{\text{quadrupole}}|NSJIF\rangle &= \frac{(-1)^{2J+I+F+S+2N'}}{4} \\ &\times [(2J+1)(2J'+1)(2N+1)(2N'+1)]^{\frac{1}{2}} \\ &\times \left[\frac{(I+1)(2I+1)(2I+3)}{I(2I-1)}\right]^{\frac{1}{2}} \begin{pmatrix} N' & 2 & N \\ 0 & 0 & 0 \end{pmatrix} \\ &\times \begin{Bmatrix} I & J' & F \\ J & I & 2 \end{Bmatrix} \begin{Bmatrix} N' & J & S \\ J & N & 2 \end{Bmatrix} eQq_0. \end{aligned} \tag{2.37}$$

The Hamiltonian for coupling due to two nuclei coupled in "series" is

$$\hat{H}_{\text{quadrupole}} = \hat{H}_Q(1) + \hat{H}_Q(2) \tag{2.38}$$

where $\hat{H}_Q(1)$ and $\hat{H}_Q(2)$ are the nuclear quadrupole Hamiltonians for nuclei I_1 and I_2, respectively. The matrix elements for the more strongly coupled spin, I_1, are identical to those of the singly coupled nucleus [2]

$$\begin{aligned} \langle J'I_1F_1|\hat{H}_Q(1)|JI_1F_1\rangle &= \frac{(-1)^{J+I_1+F_1}}{4} \begin{Bmatrix} F_1 & I_1 & J' \\ 2 & J & I_1 \end{Bmatrix} \\ &\times \begin{pmatrix} J & 2 & J' \\ J & 0 & -J \end{pmatrix}^{-1} \begin{pmatrix} I_1 & 2 & I_1 \\ -I_1 & 0 & I_1 \end{pmatrix}^{-1} eQq_{J'J}(1). \end{aligned} \tag{2.39}$$

The matrix elements for the more weakly coupled spin, I_2, are then evaluated in the coupled basis $|JI_1F_1I_2F\rangle$ [2]

$$\begin{aligned}\langle J'I_1F_1'I_2F|\hat{H}_Q(2)|JI_1F_1I_2F\rangle \;=\; & \\ & \frac{(-1)^{J'+I_1+I_2+2F_1+F}}{4}[(2F_1+1)(2F_1'+1)]^{\frac{1}{2}} \\ & \times\begin{Bmatrix} J' & F_1' & I_1 \\ F_1 & J & 2 \end{Bmatrix}\begin{Bmatrix} F & I_2 & F_1' \\ 2 & F_1 & I_2 \end{Bmatrix} \\ & \times\begin{pmatrix} J & 2 & J' \\ J & 0 & -J \end{pmatrix}^{-1}\begin{pmatrix} I_2 & 2 & I_2 \\ -I_2 & 0 & I_2 \end{pmatrix}^{-1} eQq_{J'J}(2) \qquad (2.40)\end{aligned}$$

In Eqs. (2.39) and (2.40), $eQq_{J'J}(i)$ can be determined using Eq. (2.36).

For paramagnetic species, the matrix elements for the more strongly coupled nucleus are [12]

$$\begin{aligned}\langle N'SJ'I_1F_1|\hat{H}_Q(1)|NSJI_1F_1\rangle \;=\; & \frac{(-1)^{2J+I_1+F_1+S+2N'}}{4} \\ & \times[(2J+1)(2J'+1)(2N+1)(2N'+1)]^{\frac{1}{2}} \\ & \times\left[\frac{(I_1+1)(2I_1+1)(2I_1+3)}{I_1(2I_1-1)}\right]^{\frac{1}{2}}\begin{pmatrix} N' & 2 & N \\ 0 & 0 & 0 \end{pmatrix} \\ & \times\begin{Bmatrix} I_1 & J' & F_1 \\ J & I_1 & 2 \end{Bmatrix}\begin{Bmatrix} N' & J & S \\ J & N & 2 \end{Bmatrix} eQq_0(1). \qquad (2.41)\end{aligned}$$

Then the matrix elements of the more weakly coupled nucleus can be evaluated from [12]

$$\begin{aligned}\langle N'SJ'I_1F_1'I_2F|\hat{H}_Q(2)|NSJI_1F_1I_2F\rangle \;=\; & \frac{(-1)^{2J+I_1+I_2+2F_1+S+2N'+2}}{4} \\ & \times[(2J+1)(2J'+1)(2N+1)(2N'+1)]^{\frac{1}{2}} \\ & \times[(2F+1)(2F'+1)]^{\frac{1}{2}}\begin{Bmatrix} I_1 & J' & F_1' \\ 2 & F_1 & J \end{Bmatrix} \\ & \times\left[\frac{(I_2+1)(2I_2+1)(2I_2+3)}{I_2(2I_2-1)}\right]^{\frac{1}{2}}\begin{pmatrix} N' & 2 & N \\ 0 & 0 & 0 \end{pmatrix}\end{aligned}$$

$$\times \begin{Bmatrix} I_2 & F_1' & F \\ F_1 & I_2 & 2 \end{Bmatrix} \begin{Bmatrix} N' & J & S \\ J & N & 2 \end{Bmatrix} eQq_0(2). \quad (2.42)$$

The molecular nuclear quadrupole coupling constant, eQq, is related to the electric field gradient at the nucleus, q, and the nuclear quadrupole moment, Q. This field gradient can be considered to be due only to the electron configuration in the valence p-shell of the coupling atom. Thus the experimentally determined quadrupole coupling constant can be interpreted in terms of "unbalanced" p-electrons. The Townes-Dailey model relates the molecular nuclear quadrupole coupling constant to the quadrupole coupling constant of an electron in an np-orbital [17]

$$eQq(\text{mol}) = \left(n_z - \frac{n_x + n_y}{2}\right) eQq_{n10}(\text{atom}) \quad (2.43)$$

where n_x, n_y and n_z are the numbers of electrons in the np_x, np_y and np_z orbitals, respectively. Values of eQq_{n10}(atom) are listed in Ref. 2. By relating n_x, n_y and n_z to the molecular orbital populations, this model can be used to estimate bonding characteristics such as ionic character and orbital hybridisation.

2.3.2 Nuclear Spin-Rotation Coupling

The nuclear magnetic dipole moment of one of the atoms in a molecule can interact with the magnetic field generated by the rotating molecule to give rise to nuclear spin-rotation splitting. This interaction is analogous to electron spin-rotation splitting which was described in Sec. 2.2.1. The Hamiltonian for this interaction, in diamagnetic species, is

$$\hat{H}_{\text{spin-rotation}} = C_J \mathbf{I} \cdot \mathbf{J} \quad (2.44)$$

where C_J, the nuclear spin-rotation constant in the Jth rotational state, equals

$$C_J = \frac{1}{J(J+1)} \left(C_{xx}\langle J_x^2 \rangle + C_{yy}\langle J_y^2 \rangle + C_{zz}\langle J_z^2 \rangle \right). \quad (2.45)$$

For a linear molecule with no resultant angular momentum about the molecular axis, $J_z = 0$ and symmetry makes $C_{xx} = C_{yy} = C_I$, so that

$$C_J = \frac{1}{J(J+1)} C_I \langle \mathbf{J}^2 \rangle \tag{2.46}$$

$$\equiv C_I. \tag{2.47}$$

The nuclear spin-rotation constant, C_I, is equal to

$$C_I = -g_I \mu_N h_{xx} \tag{2.48}$$

where g_I is the nuclear g-factor for the magnetic nucleus, μ_N is the nuclear magneton and h_{xx} is the component of the magnetic field perpendicular to the molecular bond axis. The nuclear spin-rotation energy expression is given by

$$E_{\text{spin-rot.}} = \frac{C_I}{2}[F(F+1) - J(J+1) - I(I+1)]. \tag{2.49}$$

The nuclear spin-rotation Hamiltonian for a molecule with a $^2\Sigma^+$ ground electronic state is

$$\hat{H}_{\text{spin-rotation}} = C_I \mathbf{I} \cdot \mathbf{N} \tag{2.50}$$

This expression is identical to that described above for diamagnetic molecules; however the operator for rotational angular momentum minus electron spin, **N**, must be used instead of **J**. The matrix elements of this Hamiltonian are given in Refs. 12, 18.

2.3.3 Spin-Spin Coupling

Electron Spin-Nuclear Spin Interaction

The Hamiltonian for the magnetic interaction between a nuclear spin, **I**, and an electron spin, **S**, in a molecule with a $^2\Sigma^+$ ground electronic state is

$$\hat{H}_{\text{spin-spin}} = b_F \mathbf{I} \cdot \mathbf{S} + c\left(I_z S_z - \frac{1}{3}\mathbf{I} \cdot \mathbf{S}\right) \tag{2.51}$$

where I_z and S_z are the components of **I** and **S** along the internuclear axis, respectively, and b_F and c are the Fermi contact and dipole-dipole interaction constants, respectively. Matrix elements of this Hamiltonian can be found in Refs. 12, 19. The Fermi contact and dipole-dipole interaction constants were defined by Frosh and Foley [20], and have the form:

$$b_F = \frac{8\pi}{3} g_e g_N \mu_B \mu_N |\Psi(0)|^2 \tag{2.52}$$

and

$$c = \frac{3}{2} g_e g_N \mu_B \mu_N \left\langle (3\cos^2\Theta - 1)/r^3 \right\rangle \tag{2.53}$$

where g_e and g_N are the electronic and nuclear g-factors and μ_B and μ_N are the Bohr and nuclear magnetons, respectively; $|\Psi(0)|^2$ is the probability of the unpaired spin at the magnetic nucleus; r is the distance between the magnetic nucleus and the unpaired electron, and Θ is the angle between the r-vector and the molecular axis.

The non-zero nuclear spin of an atom in a molecule with a $^2\Sigma^+$ ground electronic state can be used as a probe of the unpaired electron spin density in the atomic orbitals of that atom. For the paramagnetic molecules studied, the unpaired electron spin densities, $\rho(s)$ and $\rho(p)$ for an s-type and p-type orbital, respectively, were calculated from [21]

$$\rho(s) = \frac{|\Psi(0)|^2(\text{mol})}{|\Psi(0)|^2(\text{atom})} \tag{2.54}$$

$$\rho(p) = \frac{\langle (3\cos^2\Theta - 1)/r^3 \rangle(\text{mol})}{\langle (3\cos^2\Theta - 1)/r^3 \rangle(\text{atom})} \tag{2.55}$$

where $|\Psi(0)|^2(\text{mol})$ and $\langle (3\cos^2\Theta - 1)/r^3 \rangle(\text{mol})$ were calculated from the experimental b_F and c values, respectively, and $|\Psi(0)|^2(\text{atom})$ and $\langle (3\cos^2\Theta - 1)/r^3 \rangle(\text{atom})$ were calculated for the appropriate s and p orbitals, respectively, using atomic parameters taken from Morton and Preston [22].

Nuclear Spin-Nuclear Spin Interaction

Nuclear spin-spin coupling arises from the interaction of the nuclear magnetic dipole moments of two nuclei in a molecule. The interaction of two nuclear magnetic moments can be described using the Hamiltonian:

$$\hat{H}_{\text{spin-spin}} = c_4 \mathbf{I_1} \cdot \mathbf{I_2} + 3c_3 \left(I_{1z} I_{2z} - \frac{1}{3} \mathbf{I_1} \cdot \mathbf{I_2} \right) \tag{2.56}$$

where c_4 and c_3 are the scalar and tensor contributions to the nuclear spin-spin interaction. The form of this equation is identical to the Hamiltonian for the electron spin-nuclear spin interaction. The magnitude of the nuclear spin-spin interaction, however, is 4 to 5 orders of magnitude smaller than that observed for the electron spin-nuclear spin interaction. The scalar constant, c_4, is very small, on the order of 10 Hz for most molecules. It could not be determined for the species studied and so will not be discussed further.

There are two contributions to the tensor constant, c_3

$$c_3 = c_3(\text{dir.}) + c_3(\text{ind.}). \tag{2.57}$$

The first arises from the direct dipole-dipole interaction and can be calculated from the geometry of the molecule. The second contribution is due to an electron-coupled interaction. In this, the nuclear spin interacts magnetically with the electron spin of its own atom. This causes the electron spin to align antiparallel to the nuclear spin. The second nuclear spin interacts similarly with the electron spin of its own atom. Because the ground electronic state is a singlet state, the two electron spins have to be aligned antiparallel and thus the two nuclear spins also must be aligned antiparallel. This mechanism couples the two nuclear spins *via* the electron spins.

The direct contribution dominates the tensor spin-spin constant. For most molecules containing light atoms the indirect contribution can be neglected [23–25] and this has

been done for the molecules examined in this thesis. The tensor spin-spin constant $3c_3$ has been approximated to equal α_{12}, the direct nuclear spin-spin constant. For a linear molecule, α_{12} is defined as [26]:

$$\alpha_{12} = \frac{-3\mu_N^2 g_1 g_2}{r_{12}^3}. \tag{2.58}$$

where μ_N is the Bohr magneton, r_{12} is the internuclear distance, and g_1 and g_2 are the nuclear g-factors for nuclei 1 and 2, respectively.

2.4 Bond Length Determination

The precise rotational constants obtained from microwave spectroscopy can be used to determine geometrical parameters. The internuclear bond length, r_{12}, of a diatomic molecule can be determined from the rotational constant, B, given in frequency units,

$$B = \frac{h}{8\pi^2 \mu r_{12}^2} \tag{2.59}$$

where the reduced mass, μ, is

$$\mu = \frac{m_1 m_2}{m_1 + m_2} \tag{2.60}$$

and m_1 and m_2 are the atomic masses of the two atoms in the molecule. The effective bond length in the ground vibrational state, r_0, can be determined by using B_0 in Eq. (2.59). Its accuracy is limited by zero-point energy contributions. These vibrational contributions can be accounted for by calculating an equilibrium rotational constant, B_e (from Eq. (2.16)) using rotational constants obtained in two or more vibrational states; then r_e can be determined from B_e. This is the bond length for the hypothetical vibrationless state at the minimum of the potential energy curve.

The ground state rotational constants obtained for different isotopomers can also be used to obtain an r_e distance. Costain showed that for a diatomic molecule [27]

$$r_e = 2r_s - r_0 \tag{2.61}$$

where r_s is the substitution bond length. Using Costain's method [27], the distance of an atom, i, from the centre of mass, z_i, in a diatomic molecule is given as:

$$z_i^2 = \left(\frac{1}{\mu_s}\right)\Delta I_B^0 \tag{2.62}$$

where

$$\Delta I_B^0 = I_B^{0\prime} - I_B^0 \tag{2.63}$$

is the difference in the ground vibrational state moment of inertia between the substituted molecule, $I_B^{0\prime}$, and the parent molecule, I_B^0. The substitution reduced mass is

$$\mu_s = \frac{M\Delta m}{M + \Delta m} \tag{2.64}$$

where M is the mass of the parent molecule and Δm is the change in mass upon isotopic substitution. If isotopic substitutions are made at both atoms, r_s can be calculated from $z_1 + z_2$.

In these two methods only vibrational contributions have been taken into account. Electronic contributions can also be important when precise rotational constants from microwave spectroscopy are used to calculate r_e. In the Born-Oppenheimer approximation, the nuclear and electronic motions are taken to be separable; the electrons in the molecule are assumed to adjust immediately to any movement of the nuclei because the electrons are much lighter than the nuclei and are assumed to move much more quickly. However, in real molecules, the electrons do not adapt instantaneously to the movement of the nuclei.

Corrections need to be made to r_e to account for deviations from the Born-Oppenheimer approximation. The first and largest contribution arises from the reduced mass used to calculate r_e; the reduced mass expression (Eq. (2.60)) employs atomic masses for which the electrons associated with each atom were assumed to be concentrated at the nucleus.

A better description is that the electrons are arranged in a spherical distribution around each of the nuclei and that this distribution is distorted to some degree by bonding. For ionic species, such as the metal diatomic molecules studied, the charge displacement due to bonding can be quite significant. The second contribution arises from the interaction of the rotational and electronic motions. This causes the rotating nuclear frame to wobble and thus induces distortions along the internuclear axis. Corrections to account for both of these electronic effects are described in Refs. 28–30. As the precision of spectroscopic measurements has increased over the past several years, further improvements have been made to the treatment of the breakdown of the Born-Oppenheimer approximation by Bunker [31, 32] and Watson [33, 34]. In the r_e calculations discussed in this thesis, (see Sec. 6.5.1 and Sec. 8.5.1), the uncertainty in the calculated r_e value has been examined by estimating the effect of the non-spherical charge distribution. This has been done by calculating r_e using ion masses instead of atomic masses. Also theoretical results from Watson [33] and Bunker [31] have been used to provide a second estimate for the uncertainty in the equilibrium bond distance.

2.5 Interpretation of Hyperfine Parameters

Hyperfine parameters, such as nuclear quadrupole and electron spin-nuclear spin coupling constants, can be used to investigate the electronic structures of molecules. For the metal-containing species discussed in this thesis, the bonding can be described as mostly ionic with some covalent character. This bond character can be examined semi-quantitatively using a molecular orbital picture. This approach also can be used to investigate orbital hybridisation.

Consider as a model system, the singly bonded molecule, AB, with valence molecular

orbitals

$$\psi_\sigma = a\psi_A + \sqrt{1-a^2}\psi_B \tag{2.65}$$

and

$$\psi_{\sigma^*} = \sqrt{1-a^2}\psi_A - a\psi_B. \tag{2.66}$$

where a^2 and $(1-a^2)$ are the fractional weights of the atomic orbitals ψ_A and ψ_B in the bonding molecular orbital ψ_σ, respectively. Gordy and Cook [2] have related the ionic character, i_c, of the A-B bond to the difference in the fractional weights of ψ_A and ψ_B in the molecular orbital, ψ_σ,

$$\begin{aligned} i_c &= |a^2 - (1-a^2)| \\ &= |2a^2 - 1|. \end{aligned} \tag{2.67}$$

For a purely covalent bond, there are equal contributions to ψ_σ from ψ_A and ψ_B; therefore $a^2 = 0.5$ and $i_c = 0$. Similarly for a purely ionic interaction, $i_c = 1$ and a^2 is either zero or one, depending on whether it is the positive or negative pole of the A-B bond, respectively. The ionic character of the A-B bond can be calculated by relating a^2 to an experimentally determinable quantity.

2.5.1 Nuclear Quadrupole Coupling Constants

Consider AB to be a metal halide molecule where A is the quadrupolar halogen nucleus. Using the Townes-Dailey model (Eq. (2.43)), the nuclear quadrupole coupling constant of A can be related to the p-orbital occupation of atom A. This expression is repeated here

$$eQq(\mathrm{A}) = \left(n_z - \frac{n_x + n_y}{2}\right) eQq_{n10}(\mathrm{A}). \tag{2.68}$$

The z axis is taken to be the molecular axis. The valence shell configuration of A is ns^2np^5; the np_x and np_y orbitals will be filled, so $n_x = n_y = 2$. The occupation of the np_z orbital depends on the participation of $\psi_A(= \psi_{np_z})$ in the molecular orbital ψ_σ. So n_z equals $2a^2$, the fraction of the ψ_σ bond pair of electrons associated with atom A. Substituting these values into Eq. (2.68) results in

$$\begin{aligned} eQq(\mathrm{A}) &= \left(2a^2 - \frac{2+2}{2}\right) eQq_{n10}(\mathrm{A}) \\ &= \left(2a^2 - 2\right) eQq_{n10}(\mathrm{A}). \end{aligned} \tag{2.69}$$

Since A is the negative pole of the AB bond, $a^2 > 0.5$ and

$$a^2 = \frac{i_c + 1}{2}. \tag{2.70}$$

This result can be combined with Eq. (2.69) and then an expression for i_c can be obtained

$$i_c = 1 + \frac{eQq(\mathrm{A})}{eQq_{n10}(\mathrm{A})} \tag{2.71}$$

where the term $\frac{eQq(\mathrm{A})}{eQq_{n10}(\mathrm{A})}$ is negative and less than one. From this equation it can be seen that the observed nuclear quadrupole coupling constant decreases as the ionic character of the A-B bond increases; as $i_c \rightarrow 1$ $eQq(\mathrm{A}) \rightarrow 0$.

So far in this discussion, the effects of nuclear screening and orbital hybridisation have been neglected. The screening of the halogen nucleus is increased as the ionic character of the A-B bond increases. This can be accounted for by a multiplicative factor [1]. Including the correction for nuclear screening, Eq. (2.71) becomes

$$i_c = 1 + \frac{eQq(\mathrm{A})(1 + i_c\varepsilon)}{eQq_{n10}(\mathrm{A})} \tag{2.72}$$

where ε values are tabulated in Ref. 1. Neglecting the effects of nuclear screening changes the calculated ionic character by only $\sim 1.5\%$. This difference is not significant for the metal halide species studied. There should be no significant orbital hybridisation on

the halogen on the negative pole of the AB bond, because the dipole moment should suppress the hybridisation [2,35]. Orbital hybridisation, however, could not be ignored for all species studied.

The most important contribution to orbital hybridisation was *sp*-hybridisation. Considering *sp* orbital hybridisation on the quadrupolar nucleus A, the atomic orbital ψ_A will be

$$\psi_A = a_s\psi_s + \sqrt{1-a_s^2}\psi_{pz} \tag{2.73}$$

and the counterhybridised orbital will be

$$\psi_A{}' = \sqrt{1-a_s^2}\psi_s - a_s\psi_{pz} \tag{2.74}$$

where a_s^2 is the fractional weight of the *s*-orbital in the *sp*-hybrid. This *sp*-hybridisation must be accounted for in the Townes-Dailey model. The number of electrons in the np_z orbital will be

$$n_z = M(1-a_s^2) + Na_s^2 \tag{2.75}$$

where M and N are the number of electrons in the hybridised and counterhybridised orbitals, respectively. Since ψ_A is part of the molecular orbital ψ_σ, M will equal $2a^2$, the fraction of the ψ_σ bond pair associated with the atomic orbital ψ_A. The value of N depends on the occupation of $\psi_A{}'$. So when *sp*-hybridisation is included Eq. (2.68) becomes

$$eQq(\mathrm{A}) = \left(2a^2(1-a_s^2) + Na_s^2 - \frac{n_x+n_y}{2}\right) eQq_{n10}(\mathrm{A}) \tag{2.76}$$

where a^2 can be related to the ionic character of the AB bond using Eq. (2.67). Eq. (2.76) relates two unknown parameters, the degree of *sp*-hybridisation, a_s^2, and the ionic character (through a^2), to one measurable parameter, eQq(A). By finding an alternate method of determining i_c, the orbital hybridisation on the A nucleus can be calculated.

The electronegativity, x, describes the ability of an atom to attract electrons to itself in a chemical bond. The difference in electronegativity values should then be related to the ionic character of the bond. This relation has been investigated for many halogen-containing diatomic molecules [2, 35]. As a first approximation, this simple expression can be used to calculate i_c

$$i_c = \frac{|x_M - x_X|}{2}, \tag{2.77}$$

where $|x_M - x_X| \leq 2$ [35]. By fitting to the experimental results, a more exact relation for ionic character was derived,

$$i_c = 1.15 \exp\left[-\frac{1}{2}(2 - \Delta x)^2\right] - 0.15 \tag{2.78}$$

where $\Delta x = |x_M - x_X| \leq 2$ [2].

2.5.2 Electron Spin-Nuclear Spin Coupling Constants

The ionic character of a paramagnetic molecule can be investigated qualitatively *via* the electron spin-nuclear spin hyperfine constants b_F and c. These parameters are related to the unpaired electron spin density in the atomic orbitals of the atom with non-zero nuclear spin. The method for calculating these spin densities is described in Sec. 2.3.3.

Consider a $^2\Sigma^+$ ground electronic state molecule AB where atom A has a non-zero nuclear spin. The valence molecular orbitals are the same as those given in Eqs. (2.65) and (2.66)

$$\begin{aligned} \psi_\sigma &= a\psi_A + \sqrt{1 - a^2}\psi_B \\ \psi_{\sigma^*} &= \sqrt{1 - a^2}\psi_A - a\psi_B \end{aligned}$$

where the ψ_σ bonding orbital has a bond pair of electrons and the unpaired electron is in the $\psi_{\sigma*}$ antibonding orbital. The valence atomic orbitals for A are sp-hybridised (Eqs.

(2.73) and (2.74)),

$$\begin{aligned} \psi_A &= a_s\psi_s + \sqrt{1-a_s^2}\psi_{pz} \\ \psi'_A &= \sqrt{1-a_s^2}\psi_s - a_s\psi_{pz} \end{aligned}$$

where a_s^2 is the fractional weight of the s-orbital in the sp-hybrid. The unpaired electron spin densities for s and p atomic orbitals on atom A, $\rho(s)$ and $\rho(p)$ respectively, are proportional to

$$\rho(s) \propto (1-a^2)a_s^2 \tag{2.79}$$

$$\rho(p) \propto (1-a^2)(1-a_s^2) \tag{2.80}$$

where $(1-a^2)$ is the fractional weight of ψ_A in the antibonding orbital $\psi_{\sigma*}$ and a_s^2 and $(1-a_s^2)$ are the fractional weights of ψ_s and ψ_{pz} in the atomic orbital ψ_A, respectively. If both $\rho(s)$ and $\rho(p)$ are small, the $(1-a^2)$ must be small (and a^2 large). Therefore the ionic character of the A-B bond must be large, since from Eq. (2.71)

$$i_c = |2a^2 - 1|.$$

As $i_c \to 1$ then $\rho(s) \to 0$ and $\rho(p) \to 0$. So the smaller the unpaired electron spin densities in the atomic orbitals on atom A, the larger the ionic character of AB.

Chapter 3

Experimental Technique

3.1 Introduction

The experiments described in this thesis were performed using a cavity pulsed jet Fourier transform microwave (FTMW) spectrometer. This type of spectrometer was developed by Balle and Flygare as a method of measuring the spectra of weakly bound species [8,9]. The spectrometer consists of a microwave cavity into which a molecular sample is introduced as a supersonic expansion. A pulse of microwave radiation is coupled into the cavity where it interacts with the molecules travelling through the cavity inducing a macroscopic polarisation in the molecular sample. Once the microwave pulse decays, the coherent molecular emission is recorded in the time domain and then is Fourier transformed to obtain the spectrum. The introduction of the FTMW technique has caused a renaissance in microwave spectroscopy; currently there are at least fifteen research groups worldwide using these instruments. This chapter outlines the theory describing pulsed excitation experiments and the operation of the FTMW spectrometer.

3.2 Theoretical Description of FTMW Experiment

In an FTMW experiment, a pulse of microwave energy interacts with the dipole moments of the molecules in the gas sample to create a macroscopic polarisation. The molecules

emit radiation at the characteristic transition frequency after the microwave excitation pulse has ended. As the molecules relax to thermal equilibrium, the molecular emission signal decays. A theoretical description of an FTMW experiment can be made using the time dependent Schrödinger equation in density matrix formalism [36]. The derivation given here is based on the work of McGurk *et al.* [37] and Dreizler [10,38].

The molecules in the gas sample can be considered as an ensemble of two-level particles, each with rotational wavefunction

$$|\Psi\rangle = c_1|\phi_1\rangle + c_2|\phi_2\rangle \tag{3.1}$$

where ϕ_1 and ϕ_2 are eigenfunctions of the time independent molecular rotational Hamiltonian,

$$\hat{H}_{\rm rot}\phi_i = E_i\phi_i \qquad \text{for } i = 1,2. \tag{3.2}$$

The density operator for one of these particles is

$$\hat{\rho} = |\Psi\rangle\langle\Psi| \tag{3.3}$$

$$= (c_1|\phi_1\rangle + c_2|\phi_2\rangle)(c_1^*\langle\phi_1| + c_2^*\langle\phi_2|) \tag{3.4}$$

and the density matrix is

$$\hat{\rho} = \begin{bmatrix} c_1c_1^* & c_1c_2^* \\ c_2c_1^* & c_2c_2^* \end{bmatrix} \tag{3.5}$$

such that

$$\rho_{ij} = c_ic_j^*. \tag{3.6}$$

For an ensemble comprised of N two level molecules, the density matrix is

$$\rho_{ij} = \frac{1}{N}\sum_{k=1}^{N} c_i^k c_j^{*k}. \tag{3.7}$$

The microwave excitation pulse can be considered as a time dependent perturbation of this ensemble of molecules. The Hamiltonian for this system is given by

$$\hat{H} = \hat{H}_{\text{rot}} + \hat{H}_{\text{perturbation}}. \tag{3.8}$$

$\hat{H}_{\text{perturbation}}$ describes the time dependent interaction of the molecular dipole moment operator, $\hat{\mu}$, with the applied microwave field,

$$\hat{H}_{\text{perturbation}} = -2\hat{\mu}\varepsilon\cos(\omega t + \phi). \tag{3.9}$$

where 2ε, ω and ϕ are the amplitude, angular velocity and phase, respectively, of the field.

In the $\{\phi_1, \phi_2\}$ basis, the matrices of the operators in Eq. (3.8) are:

$$\hat{H}_{\text{rot}} = \begin{bmatrix} E_1 & 0 \\ 0 & E_2 \end{bmatrix} \tag{3.10}$$

and

$$\hat{H}_{\text{perturbation}} = \begin{bmatrix} 0 & -2\mu_{12}\varepsilon\cos(\omega t + \phi) \\ -2\mu_{12}\varepsilon\cos(\omega t + \phi) & 0 \end{bmatrix}. \tag{3.11}$$

The time dependence of the system is calculated from

$$i\hbar\frac{\partial\hat{\rho}}{\partial t} = \left[\hat{H}, \hat{\rho}\right]. \tag{3.12}$$

The resulting time dependent matrix elements are

$$\dot{\rho}_{11} = i(\rho_{21} - \rho_{12})x\cos(\omega t + \phi) \tag{3.13}$$

$$\dot{\rho}_{22} = -i(\rho_{21} - \rho_{12})x\cos(\omega t + \phi) \tag{3.14}$$

$$\dot{\rho}_{12} = i(\rho_{22} - \rho_{11})x\cos(\omega t + \phi) + i\rho_{12}\omega_0 \tag{3.15}$$

$$\dot{\rho}_{21} = -i(\rho_{22} - \rho_{11})x\cos(\omega t + \phi) - i\rho_{21}\omega_0 \tag{3.16}$$

where $x = 2\mu_{12}\varepsilon/\hbar$ and $\omega_0 = (E_2 - E_1)/\hbar$, the angular frequency of the rotational transition. The matrix elements, ρ_{ij}, can then be transformed into a "rotating" coordinate system using

$$\rho_{11} = \tilde{\rho}_{11} \tag{3.17}$$

$$\rho_{22} = \tilde{\rho}_{22} \tag{3.18}$$

$$\rho_{12} = \tilde{\rho}_{12}e^{i(\omega t+\phi)} \tag{3.19}$$

$$\rho_{21} = \tilde{\rho}_{21}e^{-i(\omega t+\phi)} \tag{3.20}$$

to obtain

$$\dot{\tilde{\rho}}_{11} = \frac{ix}{2}(\tilde{\rho}_{21} - \tilde{\rho}_{12}) \tag{3.21}$$

$$\dot{\tilde{\rho}}_{22} = -\frac{ix}{2}(\tilde{\rho}_{21} - \tilde{\rho}_{12}) \tag{3.22}$$

$$\dot{\tilde{\rho}}_{12} = \frac{ix}{2}(\tilde{\rho}_{22} - \tilde{\rho}_{11}) + i(\omega_0 - \omega)\tilde{\rho}_{12} \tag{3.23}$$

$$\dot{\tilde{\rho}}_{21} = -\frac{ix}{2}(\tilde{\rho}_{22} - \tilde{\rho}_{11}) - i(\omega_0 - \omega)\tilde{\rho}_{12}. \tag{3.24}$$

Then the real quantities s, u, v, and w are defined as

$$s = \tilde{\rho}_{11} + \tilde{\rho}_{22} = 1 \tag{3.25}$$

$$u = \tilde{\rho}_{21} + \tilde{\rho}_{12} \tag{3.26}$$

$$-iv = \tilde{\rho}_{21} - \tilde{\rho}_{12} \tag{3.27}$$

$$w = \tilde{\rho}_{11} - \tilde{\rho}_{22} \tag{3.28}$$

where s is the trace of the density matrix, which is constant, w is related to the population difference between the two rotational levels, ΔN, and u and v are the real and imaginary parts, respectively, of the macroscopic polarisation, P. The derivatives of these quantities can be obtained by neglecting terms in 2ω (using the rotating wave approximation [10])

and choosing the phase of the microwave pulse such that $\phi = 0$,

$$\dot{s} = 0 \tag{3.29}$$

$$\dot{u} = -v\Delta\omega \tag{3.30}$$

$$\dot{v} = u\Delta\omega - wx \tag{3.31}$$

$$\dot{w} = xv \tag{3.32}$$

where $\Delta\omega = \omega_0 - \omega$ is the difference between the transition frequency, ω_0 and the frequency of the applied microwave pulse, ω.

In an FTMW experiment, the population difference between the two rotational levels, ΔN, before the microwave excitation is applied is

$$N_1 - N_2 = N(\rho_{11} - \rho_{22}) \tag{3.33}$$

$$= Nw_0. \tag{3.34}$$

Also $u_0 = v_0 = 0$, since the density matrix is diagonal before the microwave pulse is applied.

At time $t = 0$, a pulse of microwave radiation of angular velocity ω is applied, where ω is near resonant with the rotational transition frequency, ω_0, so that $\Delta\omega$ is small. If x, the amplitude of the microwave energy, is chosen to be

$$x = \frac{2\mu_{12}\varepsilon}{\hbar} \gg \Delta\omega, \tag{3.35}$$

then Eqs. (3.29) - (3.32) can be approximated as

$$\dot{s} = 0 \tag{3.36}$$

$$\dot{u} = 0 \tag{3.37}$$

$$\dot{v} = -xw \tag{3.38}$$

$$\dot{w} = xv. \tag{3.39}$$

The solution to these differential equations is

$$v(t) = -w_0 \sin(xt) \tag{3.40}$$

$$w(t) = w_0 \cos(xt) \tag{3.41}$$

$$u(t) = 0 \tag{3.42}$$

because $v_0 = 0$. So during the microwave excitation pulse $v(t)$ and $w(t)$ oscillate between w_0 and $-w_0$ at angular velocity x.

At time $t = t_p$, the microwave excitation is turned off and

$$u_p = 0 \tag{3.43}$$

$$v_p = -w_0 \sin(xt_p) \tag{3.44}$$

$$w_p = w_0 \cos(xt_p). \tag{3.45}$$

When the amplitude of the microwave excitation goes to zero, x becomes zero. Neglecting relaxation effects, Eqs. (3.29) - (3.32) become

$$\dot{s} = 0 \tag{3.46}$$

$$\dot{u} = -v\Delta\omega \tag{3.47}$$

$$\dot{v} = u\Delta\omega \tag{3.48}$$

$$\dot{w} = 0. \tag{3.49}$$

Solving these differential equations results in

$$u(t) = -v_p \sin(\Delta\omega t) \tag{3.50}$$

$$v(t) = v_p \cos(\Delta\omega t) \tag{3.51}$$

$$w(t) = w_p \tag{3.52}$$

for $t > t_p$.

The macroscopic polarisation induced in the sample by the microwave pulse is expressed as

$$\begin{aligned} P(t) &= N\langle\hat{\mu}\rangle && (3.53)\\ &= NTr(\hat{\mu}\hat{\rho}) && (3.54)\\ &= NTr\begin{bmatrix} 0 & \mu_{12} \\ \mu_{12} & 0 \end{bmatrix}\begin{bmatrix} \rho_{11} & \rho_{12} \\ \rho_{21} & \rho_{22} \end{bmatrix} && (3.55)\\ &= N\mu_{12}\left(\rho_{21}+\rho_{12}\right) && (3.56)\\ &= N\mu_{12}\left(u(t)\cos(\omega t) - v(t)\sin(\omega t)\right). && (3.57) \end{aligned}$$

Then substituting in for $u(t)$ and $v(t)$ results in

$$\begin{aligned} P(t) &= N\mu_{12}\left(-v_p\sin(\Delta\omega t)\cos(\omega t) - v_p\cos(\Delta\omega t)\sin(\omega t)\right) && (3.58)\\ &= -N\mu_{12}v_p\left(\sin\left[(\Delta\omega+\omega)\right]\right) && (3.59)\\ &= -N\mu_{12}v_p(\sin(\omega_0 t)) && (3.60)\\ &= N\mu_{12}(w_0\sin(xt_p))(\sin(\omega_0 t)). && (3.61) \end{aligned}$$

From this expression, it can be seen that the macroscopic polarisation will oscillate at ω_0, the frequency of the rotational transition. $P(t)$ depends on the initial population difference, w_0N, the transition dipole moment, μ_{12}, and the length of microwave excitation pulse, t_p. The macroscopic polarisation can be optimised by maximising $\sin(xt_p)$; this occurs when the microwave pulse length, t_p, satisfies $xt_p = 2\mu_{12}\varepsilon t_p/\hbar = n\pi/2$ where n is an integer. This is called the "$\pi/2$" condition. For a constant ε, the smaller the transition dipole moment the longer the pulse length needed to obtain the "$\pi/2$" condition.

Eq. (3.61) was derived without considering relaxation effects. In a real FTMW experiment, the macroscopic polarisation, $P(t)$, decays to zero and the population difference, $\Delta N = wN$, returns to thermal equilibrium. Exponential terms describing both types of

relaxation can be added phenomenologically to the expressions derived above to account for these effects [10,37].

3.3 Microwave Cavity

A Fabry-Perot microwave cavity forms the heart of a FTMW spectrometer. The cavity consists of two spherical aluminium mirrors with radius of curvature of 38.4 cm and diameter 28 cm placed approximately 30 cm apart. One of the mirrors is movable so the cavity can be manually tuned into resonance at the microwave excitation frequency using a micrometer screw; the other mirror is held fixed. A schematic diagram of the microwave cavity is given in Fig. 3.1.

In the original FTMW spectrometer design [9], the pulsed nozzle was mounted so that the molecular jet and the microwave cavity axis were perpendicular. However, it has since been observed that injecting the molecular sample parallel to the cavity axis increases the sensitivity of the spectrometer [39,40]. To operate in the "parallel" configuration, the pulsed nozzle is mounted slightly off centre (~2-3 cm) in the fixed mirror. Because the line widths obtained with this configuration are between ~7-10 kHz, each line appears as a doublet due to the Doppler effect. The microwave mirrors are mounted on translation rods inside a vacuum chamber, which is pumped by a 6 in. diffusion pump backed by a mechanical pump. The experimental repetition rate is limited to approximately 1 Hz by the efficiency of the pumping system.

The microwave excitation pulse is coupled into the cavity *via* an antenna located at the centre of one of the microwave mirrors. The cavity has a bandwidth of 1 MHz when operating at 10 GHz, which restricts the maximum frequency step-size while searching to 1 MHz. The operating range of the spectrometer is 4-26 GHz.

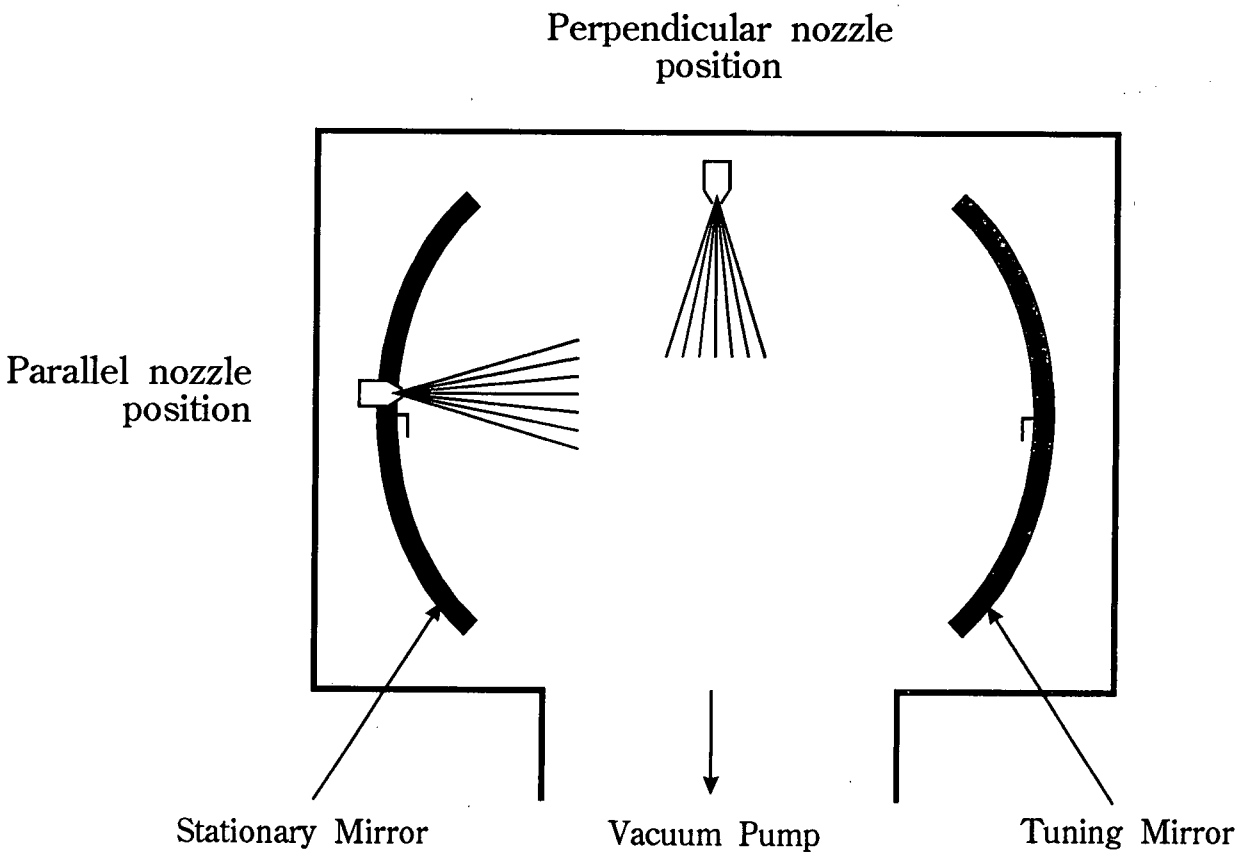

Figure 3.1: Schematic diagram of microwave cavity showing location of mirrors, nozzle and antennae.

3.4 Microwave Source

A Hewlett-Packard 8340A synthesiser was used as the microwave source for the experiments described in this thesis. During the experiments on MgS, MgBr and MgNC the synthesiser was referenced to an internal 10 MHz standard which has an aging rate of $1x10^{-9}$ per day. The HP synthesiser is now referenced to a 10 MHz frequency obtained from a Loran C frequency standard which is accurate to 1 part in 10^{-12}. The remaining experiments, on AlNC, AlBr, YF and YBr, were performed using this setup. The 10 MHz signal is also used to control the timing of the experiment and to do up- and down-frequency conversions.

3.5 Experiment Sequence

To perform an experiment, the cavity must first be tuned into resonance at the excitation frequency, ν_{MW}. To do this the microwave synthesiser is swept over a range of frequencies centred about the microwave excitation frequency, ν_{MW}. An antenna in the movable mirror is used to couple the microwave energy into the cavity. The signal is detected using an antenna located at the centre of the fixed mirror and the cavity modes are monitored using an oscilloscope. The size of the cavity is changed using a micrometer screw to optimise the transmission of radiation at the microwave excitation frequency. The cavity must be re-tuned every time the excitation frequency is changed to ensure the maximum transmission of energy.

The trigger signals for the experiment are generated using a home built pulse generator. Schematic diagrams of the measurement pulse sequence and spectrometer electronics are shown in Figs. 3.2 and 3.3. One FTMW experiment cycle consists of two parts; first, the decay of the cavity without a molecular pulse is measured and then the decay of the cavity and the molecular signal is recorded. The cavity background signal is subtracted

from the cavity plus molecular decay to remove any residual cavity "ringing" effects.

Since the measurement sequences for both parts of the experiment cycle are basically identical, only the second part (with the molecular pulse) will be described in detail. The microwave synthesiser produces a frequency, ν_{MW} + 20 MHz, which is divided and part is mixed with 20 MHz in the single sideband modulator to generate ν_{MW}. The microwave excitation pulse is produced by opening and closing a PIN diode switch (labelled MW-switch in Fig. 3.3). This is coupled into the microwave cavity through the circulator. Here the radiation interacts with a gas sample which has been injected into the cavity. After the microwave pulse is turned off, the molecules emit a coherent signal, $\nu_0 = \nu_{MW} + \Delta\nu$, which is slightly off resonant from the the excitation frequency, ν_{MW}, by $\Delta\nu$. The molecular signal is coupled out of the cavity *via* the circulator. A second PIN diode switch (labelled protective MW-switch in Fig 3.3) is used to protect the detection circuit from being damaged by the microwave excitation pulse. The molecular signal is then amplified, down-converted to 20 MHz + $\Delta\nu$, using the output of the microwave synthesiser, and then down-converted to 5 MHz + $\Delta\nu$, using the 25 MHz signal.

3.6 Data Acquisition

The decay signals from each part of the measurement cycle are collected using a transient recorder (plug-in A/D board with maximum sampling rate 25 MHz). Since the molecular signal is being measured at discrete intervals, care must be taken so that the complete spectrum can be recovered from the sampled values. This is accomplished by sampling the function at at least twice the highest frequency desired because two points are needed per wavelength to recover the entire spectrum. Failure to do this results in aliasing, in which higher frequency lines appear at lower incorrect frequencies in the resulting spectrum. In the FTMW experiments, the transient recorder measures frequencies centred about

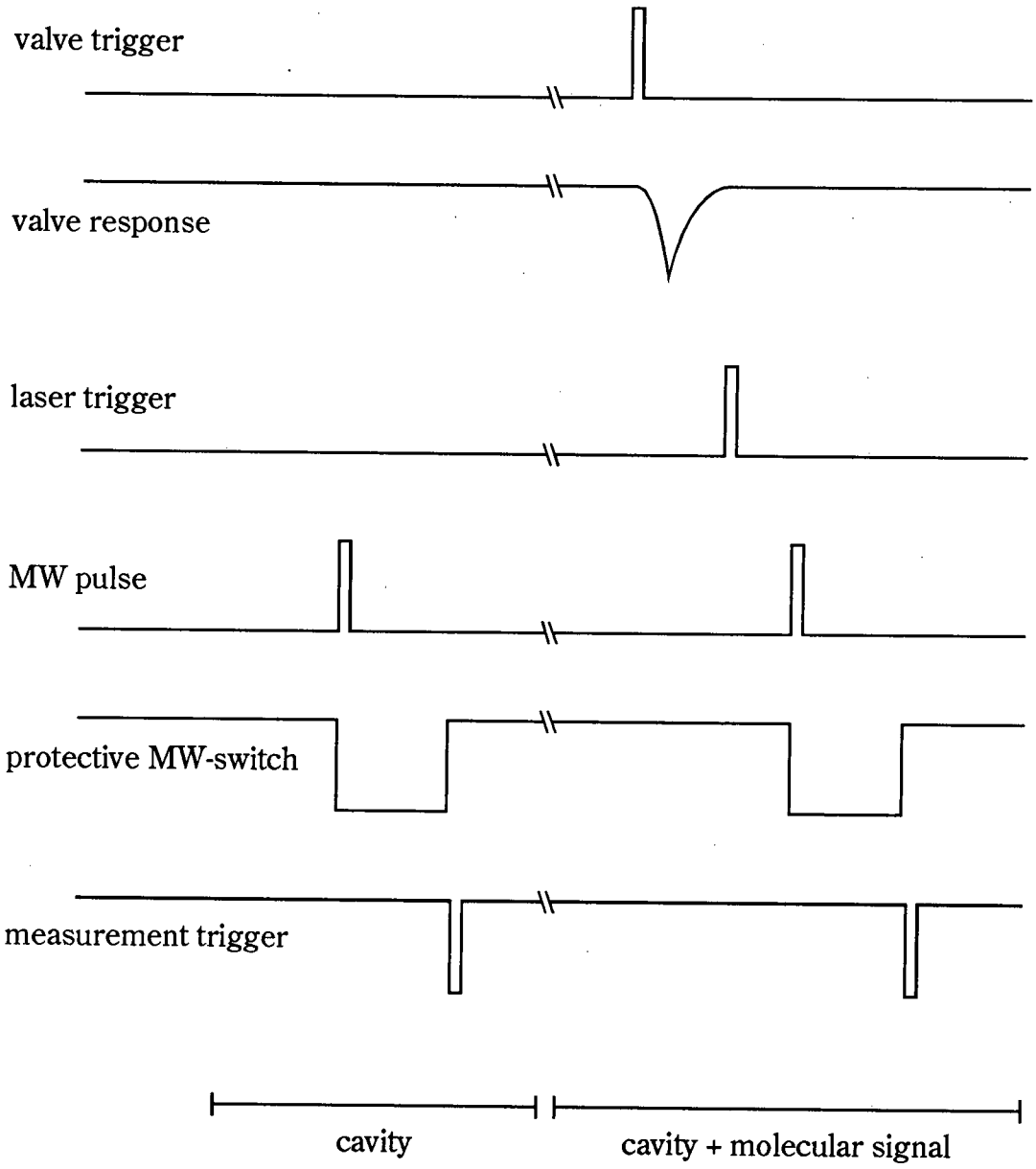

Figure 3.2: Schematic pulse sequence diagram.

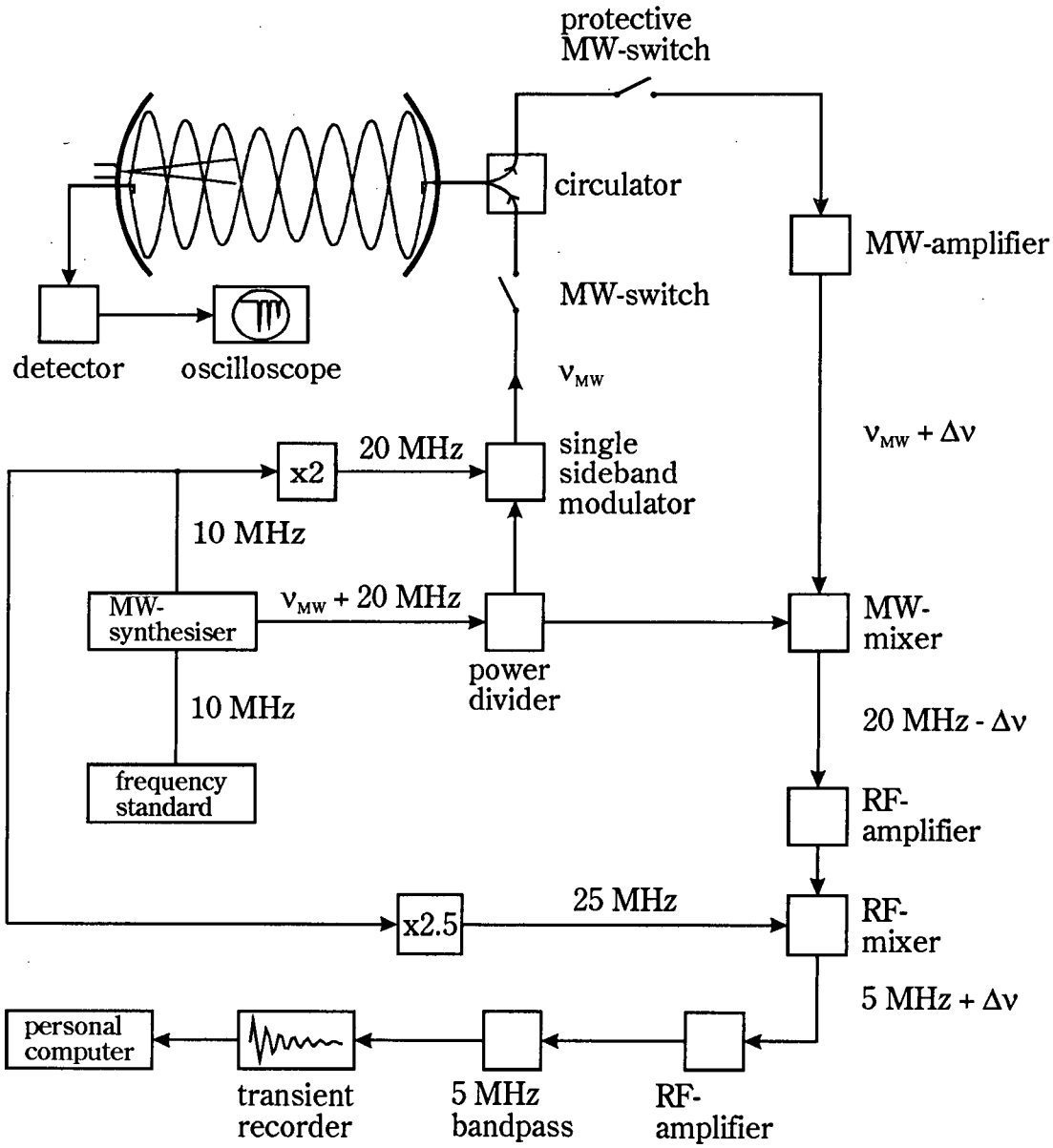

Figure 3.3: Schematic circuit diagram.

5 MHz using a sampling interval of 50 ns and aliasing is prevented by using a 5 MHz bandpass filter prior to digitising the signal. 4 K data points are recorded.

The molecular decay signal, obtained by subtracting the cavity-only signal from the cavity-plus-molecular signal, is stored in the computer and the results of successive experiments are co-added. The time domain signal is transformed into frequency domain by a discrete Fourier transform

$$F(\nu) = \sum_{n=0}^{N-1} f(n\Delta t)e^{-i2\pi\nu n\Delta t} \tag{3.62}$$

where $f(n\Delta t)$ is the time domain signal consisting of n data points collected with Δt sampling interval. The molecular signal is displayed as a power spectrum which is obtained by summing the squares of the real and imaginary parts of the Fourier transform. Peak positions of strong unblended lines are determined by averaging the frequencies of the two Doppler components obtained from the power spectrum. For closely spaced or overlapped lines, distortions occur in the power spectrum [41] and to determine the line positions accurately a fit must be made to the time domain signal [42].

The digital resolution of the obtained spectrum is limited by the uncertainty principle. The frequency interval between data points in the spectrum is inversely proportional to the acquisition time, thus the resolution of the spectrum can be increased by increasing the measurement time. This can be simulated using a technique called "zero-filling" where zeros are added to the end of the spectrum after measurement to artificially enhance the digital resolution [43]. The accuracy of the lines measured in these experiments is estimated to be better than ± 1 kHz.

3.7 Gas Sample

The molecular samples were injected into the microwave cavity through a General Valve Series 9 nozzle, which was operated with a backing pressure of 5-7 bar. The compounds

studied in this work were prepared by reacting the ablated target metal atoms with precursor molecules, which were present as no more than 0.5% in Ar carrier gas. The details of the laser ablation setup are discussed in Chapter 4. The metal-containing species are formed through collisions in the nozzle. In the supersonic expansion, the translational and rotational energies are converted into mass flow along the axis of expansion; this results in very low rotational temperatures (~1 K). Narrow line widths (~7-10 kHz) are obtained because the near collision-less environment of the jet removes pressure broadening, which is the major contribution to line broadening in traditional microwave experiments.

Vibrational cooling of the molecules is less efficient and more dependent on the composition of the gas sample. This can be seen in the difference in vibrational temperatures estimated for MgS and MgBr. The strongest transition for each molecule ($J = 1 - 0$ for MgS and $N = 1 - 0$, $J = 3/2 - 1/2$, $F = 3 - 2$ for MgBr) was measured in both the $v = 0$ and $v = 1$ vibrational states, taking 1000 averaging cycles for each spectrum. The signal to noise ratios and intensities of these spectra were used to estimate the vibrational temperatures, T_{vib}. For MgBr, T_{vib} was estimated to be $\sim$ 320 K, using a gas mixture of 0.1% Br_2 in 6.5 bar Ar. A higher vibrational temperature of $\sim$ 550 K was obtained for the MgS experiments where a mixture of 0.2% OCS in 5.5 bar Ar was used. This range of T_{vib} values is typical for FTMW laser ablation experiments [44–46].

3.8 Helmholtz Coils

Special care had to be taken when measuring the spectra of MgNC and MgBr because these species are paramagnetic and the rotational spectra would show first order Zeeman splitting due to the earth's magnetic field. This effect could generally be removed using a set of three mutually perpendicular Helmholtz coils [47] to collapse the Zeeman

pattern down to the expected Doppler components. Fig. 6.1 shows an example transition of MgBr measured with the Zeeman splitting removed using the Helmholtz coils. The transition frequency could then be determined in the usual way by averaging the frequencies of the Doppler components obtained from the power spectrum. However, residual Zeeman splitting was observed in some transitions; this is shown in Fig. 7.1, a transition of MgNC. To measure the centre frequencies of these transitions accurately, the positions of these closely spaced lines were determined by a fit to the time domain signals [42] and the frequencies of the components were averaged. For some transitions, use of the Helmholtz coils produced a very wide Doppler doublet with the Zeeman splitting incompletely removed (see the upper spectrum of Fig. 6.2). For this line and some others, the most accurate determination of the transition frequency was made by measuring the components of the Zeeman pattern obtained without the Helmholtz coils (see lower spectrum of Fig. 6.2). In these cases, the line positions of the closely spaced Zeeman components were determined by fitting to the time domain signals [42] and then the component frequencies were averaged to obtain the line positions. Centre frequencies calculated for the spectra of several lines taken with the Helmholtz coils both on and off indicated that the uncertainty introduced by the averaging method is less than ± 2 kHz.

Chapter 4

Development of Laser Ablation Source

4.1 Introduction

Laser ablation coupled with supersonic expansion has been shown to be an effective method for producing gas phase metal-containing compounds [48–50]. The main advantage of this method is that the setup can be operated at room temperature; the energy needed to vaporize the metal sample is introduced as a pulse of laser radiation. Earlier methods of producing gas phase metal species used high temperature oven systems. The heating apparatus and insulation required to operate one of these systems would be quite difficult to mount into an FTMW spectrometer. In contrast, laser ablation sources have been successfully incorporated into several FTMW spectrometers. They have provided data on various compounds such as: carbides [51], oxides [44,52,53], halides [45,46,54–56], isocyanides [57], and hydroxides, [58, 59]. More recently, larger molecules such as borohydrides [60], glycine [61] and urea [62] have been investigated in this manner.

The most prevalent method of producing laser ablated samples for FTMW spectroscopy is vaporization of a solid sample of the molecule of interest. A second method, ablation of the target metal followed by reaction with a gas phase precursor, has been used to a lesser extent. The limitation of the vapourisation method is that it is often difficult to produce a rod of the desired compound. The ablate and react method provides

more flexibility in producing transient species. A complete list of the FTMW studies of species produced by each method prior to the present work is given in Table 4.1.

Almost all the laser ablation-FTMW spectrometers used to measure these spectra operate in the "perpendicular" configuration, with the molecular beam travelling perpendicular to the microwave cavity axis [44,45,62]. This configuration has the advantage that the nozzle is completely independent of other equipment, and variations in nozzle design can be easily implemented. Yet with most spectrometers, and especially the one used for these experiments, this arrangement has reduced resolution and sensitivity compared with that obtained with the "parallel" configuration, in which the nozzle is mounted in one of the mirrors and the molecular beam travels parallel to the cavity axis [39,40]. The location of the nozzle in the perpendicular and parallel configurations is shown in Fig. 3.1.

In the earlier laser ablation studies from this laboratory, the parallel configuration was used [46,54,56]. In this source, the metal rod was kept in a fixed position to simplify construction. However, other work has suggested that rotating the rod provides better signal strength and stability over a series of experiments [63]. Although it was somewhat awkward to design, a laser ablation system has been constructed which is mounted in the mirror and incorporates a rotating rod.

4.2 Ablation Source Design

The nozzle cap design was based on the system of Barnes *et al.* [64]. The laser ablation source consists of a stainless steel nozzle cap which holds a metal rod 5 mm from the orifice of a General Valve Series 9 pulsed nozzle. A schematic diagram of the nozzle cap and its location in the mirror is shown in Figure 4.1. In order to operate in the parallel configuration, the laser ablation source had to be mounted in the fixed mirror. This was

done by recessing the back of the fixed mirror to hold the nozzle cap and other equipment. The gas channel, in the nozzle cap, begins at 1.5 mm in diameter at the nozzle orifice and increases to 5 mm at the point of ablation. The total length is 2 cm and the outlet of the nozzle cap is 2.5 mm from the front surface of the fixed mirror. The last 5 mm of the gas channel is an inter-changeable brass nozzle cap extension. This was included in the design so that the expansion conditions could be varied.

Two parameters were varied to obtain the final design for the nozzle cap, the exit conditions and the gas channel diameter. In the preliminary design, a cone shaped nozzle cap extension, with the inlet larger than the outlet, was used in an attempt to enhance cooling of the gas sample. This, however, proved only to reduce signal strength. A straight nozzle cap extension provided the strongest signals; the signal to noise ratio improved by an order of magnitude when using the straight extension instead of the cone shaped extension. The nozzle cap gas channel diameter, initially 1.5 mm, was changed incrementally. It was found that signal strength increased as the diameter of the channel was increased. The gas channel diameter is limited to 5 mm by the size of hole which can be drilled in the mirror without affecting spectrometer sensitivity.

A 5 mm diameter rod of the target metal is supported in the nozzle cap and is translated and rotated by a motorised actuator (Oriel Motor Mike). A diagram of the rotating rod setup is shown in Fig. 4.2. As had been anticipated, it was found that rotating the rod did maintain signal strength over a series of experiments [63]. When the rod was not rotated, the signal strength was found to decrease by up to 50% over 2000 laser pulses. A side view of the fixed mirror with the nozzle cap and rotating rod assembly mounted is shown in Fig. 4.3.

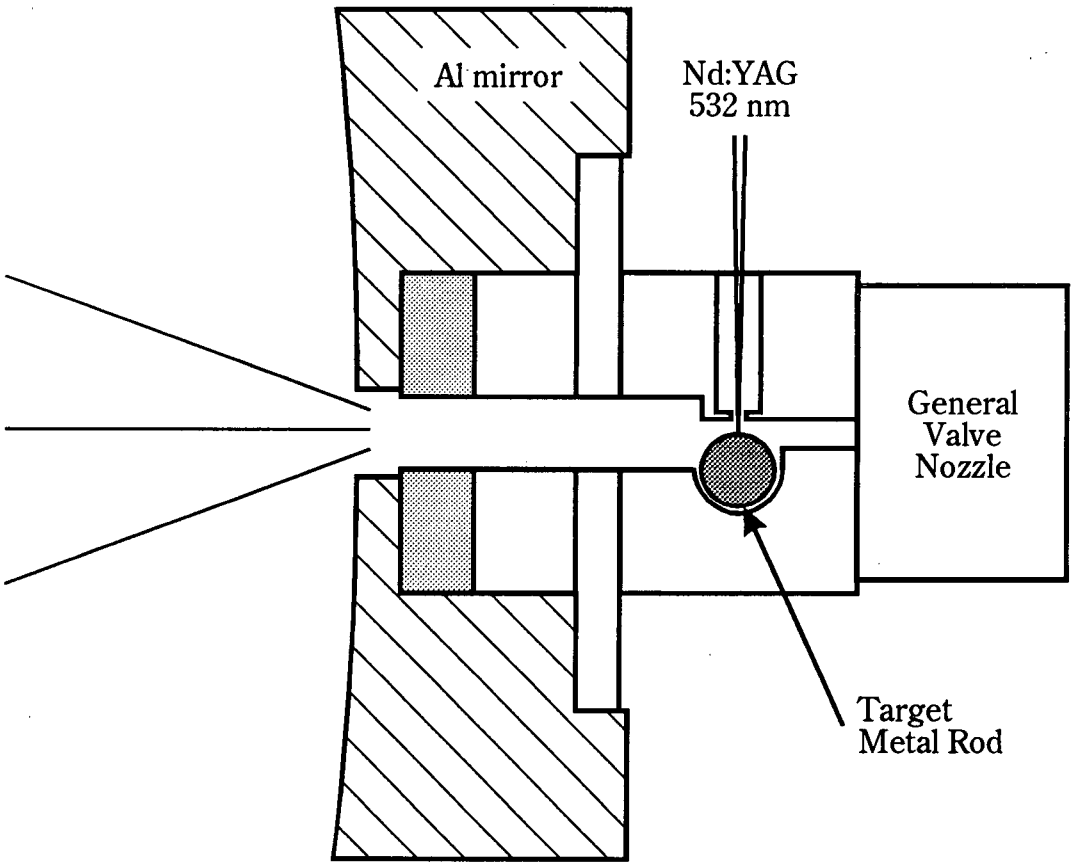

Figure 4.1: Top view of laser ablation nozzle cap and part of fixed aluminium mirror. The nozzle cap is mounted slightly off centre in the mirror. Shaded part at the end of the gas channel is the nozzle cap extension; see Sec. 4.2 for details. The motorized actuator (not shown in diagram) is located below the plane of the paper.

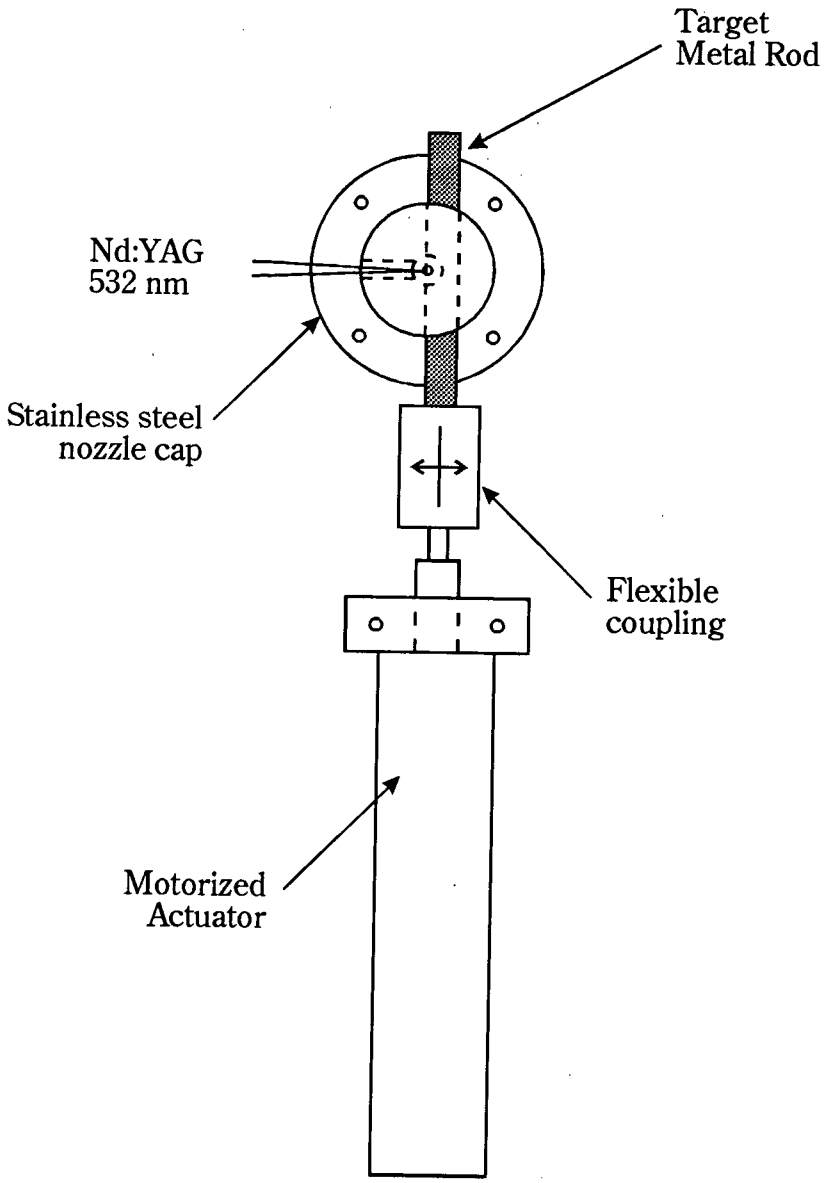

Figure 4.2: View of laser ablation nozzle cap and motorized actuator. The metal rod is coupled to the motorized actuator with a length of flexible rubber tubing.

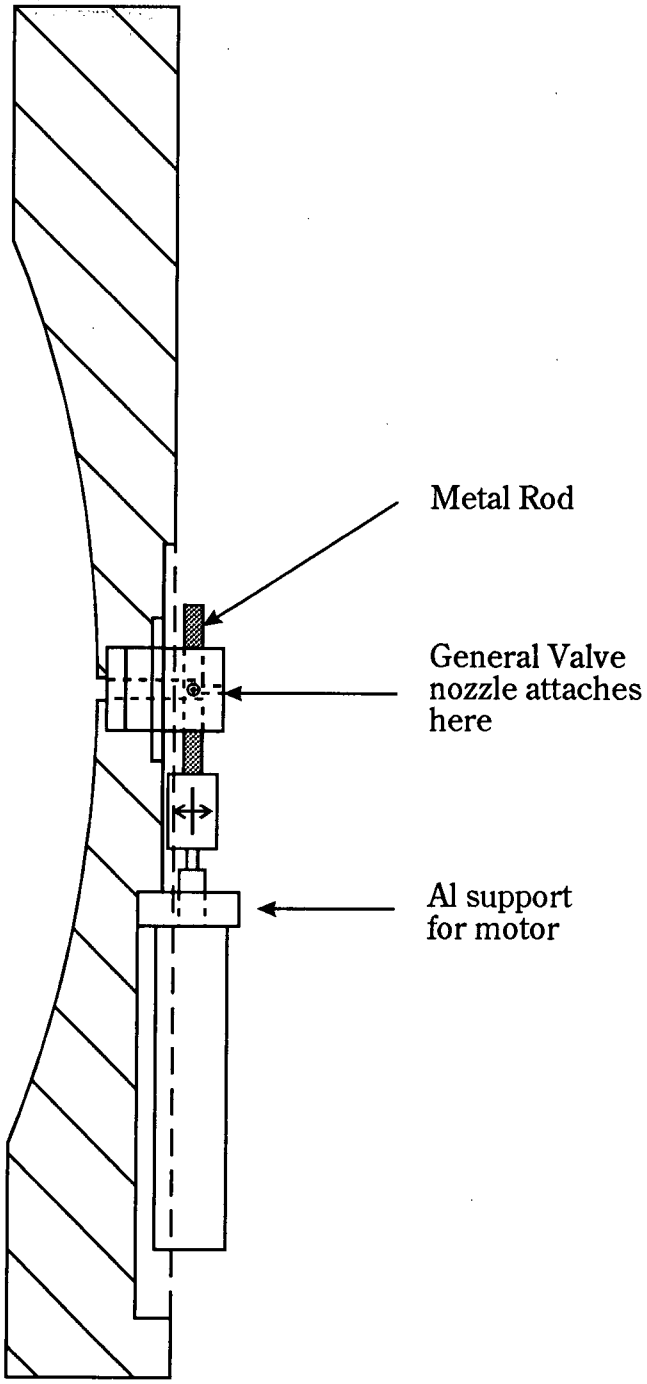

Figure 4.3: Side view of fixed mirror showing location of nozzle cap and motorized actuator. The dashed vertical line shows the recesses needed to mount the laser ablation setup in the back of the mirror.

4.3 Experimental Details

In the experiments described in this thesis, the rod was ablated using the frequency doubled output of a Q-switched Nd:YAG laser (Continuum Surelite I-10). The second harmonic frequency was initially used because it is in the visible region and therefore it was easier to align the system. Strong signals were obtained for all the species studied, so no attempt was made to use other laser frequencies. The laser energy was directed into the vacuum chamber using a set of mirrors. The beam was focused to a spot less than 1 mm in diameter at the point of ablation using a lens located just outside the chamber. Fig. 4.4 shows a schematic diagram of the laser coupling system. The laser energy enters the nozzle cap through a channel which is at right angles to the gas expansion channel (for detail see Fig. 4.1). The laser power was not monitored during the experiment but was estimated to be $\sim$ 5-10 mJ/pulse. The timing of the laser pulse with respect to the nozzle opening was crucial. The pulse sequence for the experiment is shown in Fig. 3.2. The optimum delay between the nozzle being fully open and the laser pulse was $\sim$ 300-350 μs.

4.4 Testing of Laser Ablation Source

The performance of the laser ablation setup was evaluated by measuring the spectra of several molecules investigated with the fixed rod laser ablation setup. Preliminary tests were done using AgCl and CuCl [54]; the spectra obtained with the rotating rod setup had signal to noise ratios which were about five times those obtained with the fixed rod system.

The final molecule measured with the fixed rod system was yttrium monochloride [56]. The transitions observed in this work were reported as being "frustratingly weak". Fig. 4.5 compares the results obtained for the strongest hyperfine components of the $J = 2-1$

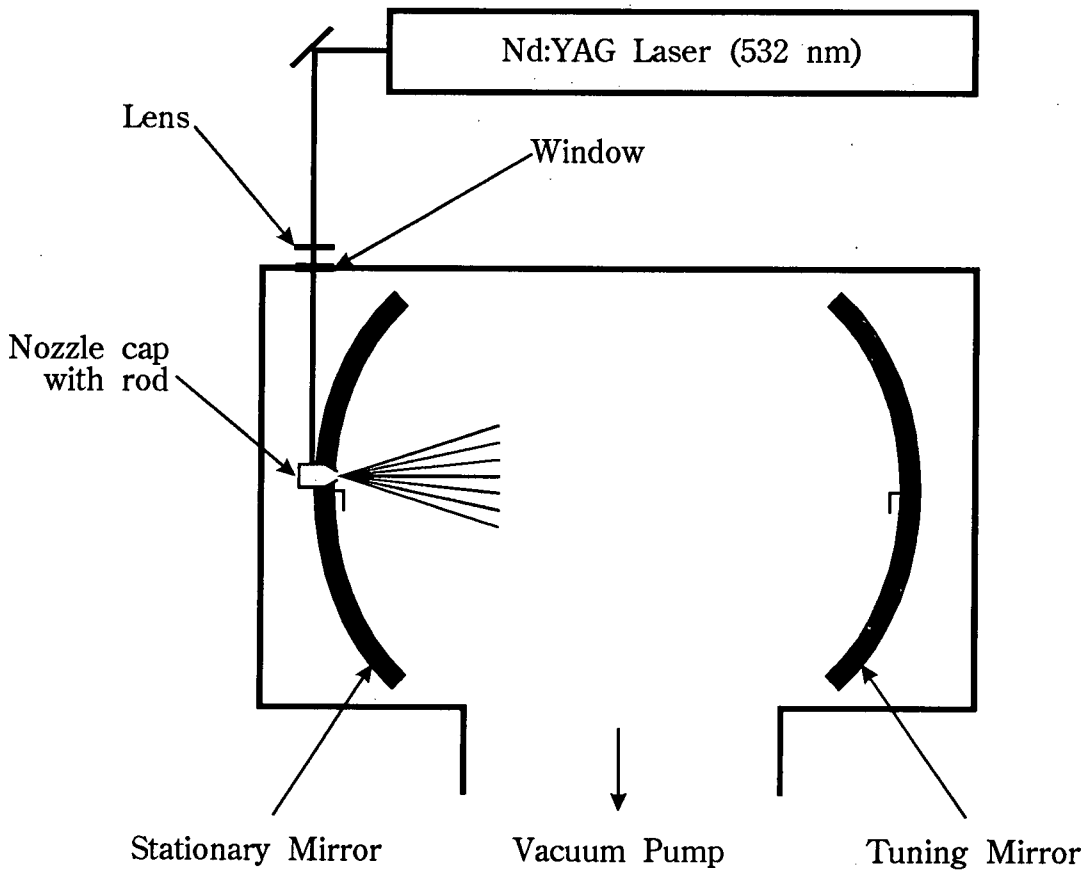

Figure 4.4: Diagram showing method of coupling laser energy into the spectrometer cavity.

transition of $Y^{35}Cl$ using the fixed rod (upper spectrum) and the rotating rod (lower spectrum) systems. The magnitude of the Doppler splitting differs between the two spectra because different backing gases were used in the expansion. It can be seen that this rotating rod laser ablation setup marks an improvement in the FTMW spectroscopy of metal-containing species.

The final test of the rotating rod laser ablation setup was the measurement of magnesium sulfide. These experiments, which are described in Chapter 5, are the first FTMW measurement of a metal sulfide produced by reacting ablated metal with a source of sulfur; there had been no previous FTMW measurements of MgS or other metal sulfides. Several species of low natural abundance were observed. This study demonstrates the utility and sensitivity of the rotating rod laser ablation setup.

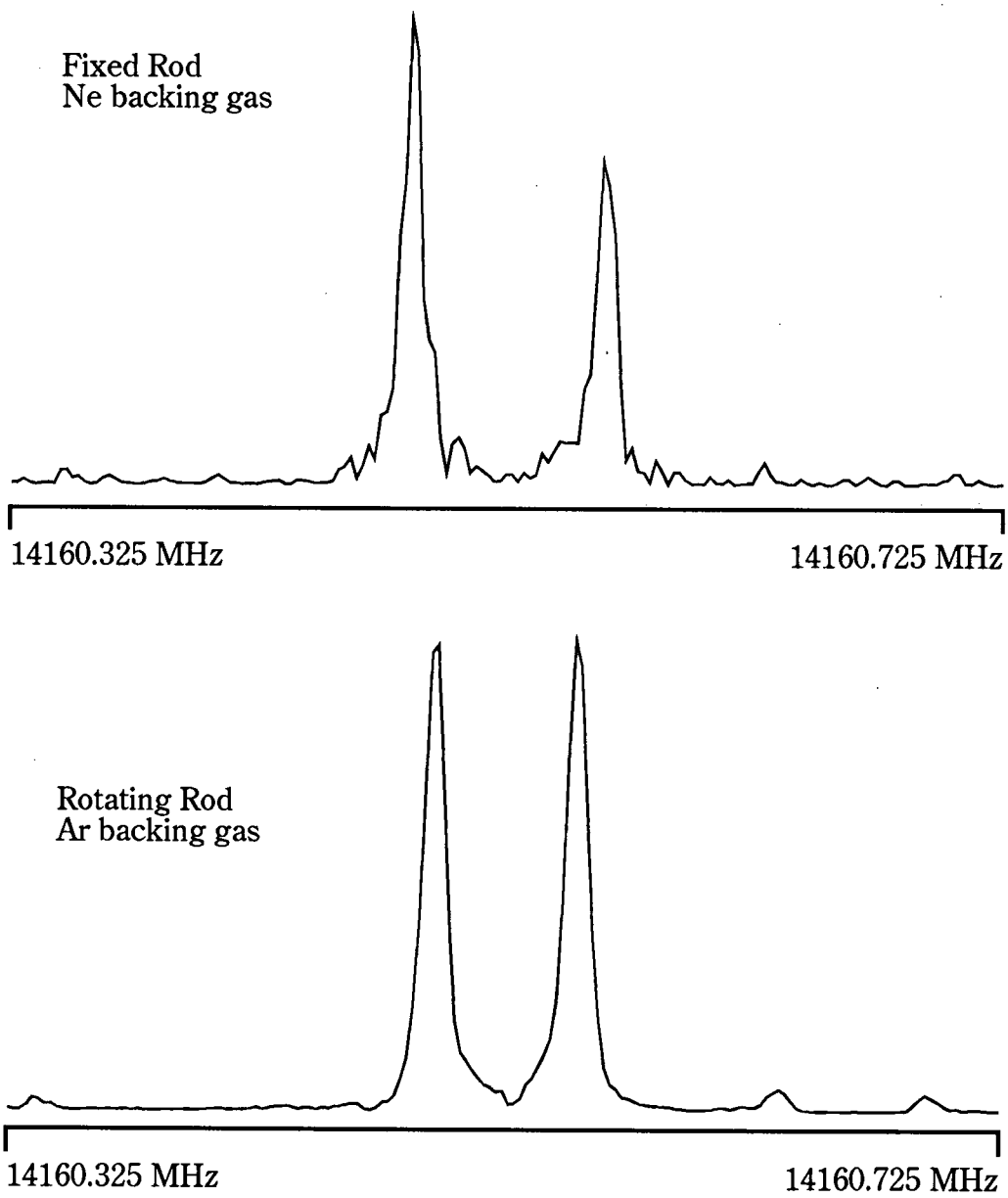

Figure 4.5: Comparison of spectra taken of the overlapped hyperfine components $F = 5/2-3/2, 7/2-5/2$ of the $J = 2-1$ transition of $Y^{35}Cl$. Both spectra were recorded with 320 averaging cycles. 4 K data points were recorded and the spectra are displayed as 8 K transformations. The upper and lower spectra were recorded using the fixed rod system and the rotating rod setups, respectively. The excitation frequencies used to obtain the upper and lower spectra were 14160.300 MHz and 14160.525 MHz, respectively.

Table 4.1: FTMW Spectroscopy of Molecules Produced by Laser Ablation.

Vapourization of Sample:			
Carbides	SiC_2	Suenram et al. 1989	[51]
Oxides	YO, LaO, ZrO, HfO	Suenram et al. 1990	[44]
	VO, NbO	Suenram et al. 1991	[52]
	SrO, BaO	Blom et al. 1992	[53]
Halides	CuCl, CuBr	Low et al. 1993	[55]
Hydroxides	NaOH, KOH, RbOH, CsOH	Kawashima et al. 1996	[58]
	InOH	Lakin et al. 1997	[59]
Larger	KBH_4, $NaBH_4$	Kawashima et al. 1995	[60]
	glycine	Lovas et al. 1995	[61]
	urea	Kretschmer et al. 1996	[62]
Ablation and Reaction to form Sample:			
Halides	AgCl, AlCl, CuCl	Hensel et al. 1993	[54]
	MgCl	Ohshima and Endo 1993	[45]
	YCl	Hensel and Gerry 1994	[56]
	InF, InCl, InBr	Hensel and Gerry 1997	[46]
Isocyanides	CaNC	Scurlock et al. 1994	[57]

Chapter 5

FTMW Spectroscopy of MgS

5.1 Introduction

Significant spectroscopic interest in many compounds containing refractory metals has arisen because of the observed depletion of these metals in interstellar clouds [65, 66]. Most of the depleted elements are contained in dust grains, but gas phase molecules containing metals such as Mg should be detectable [67]. By searching for refractory metal compounds in space, a greater understanding of their chemistry in both the gas phase and on dust grains can be obtained [6,67]. Thus far the only magnesium bearing molecule observed has been MgNC, found via its millimetre wave spectrum in IRC +10216 [68,69]. Hence there is particular interest in other simple Mg containing compounds.

One of these, MgS, has been the target of several astrophysical searches. Features in the far infrared spectra of several carbon-rich stars have been attributed to the vibration of MgS on dust grains [70]. This assignment was based on laboratory far infrared spectroscopy of powdered MgS samples prepared in polyethylene [71]. Further laboratory work in the optical region [72] confirmed this assignment but suggested that FeS and mixed MgFe sulfides might also contribute to this feature. The first radio astronomical search for gaseous MgS was reported by Takano *et al.* as part of a laboratory millimetre wave study [73]. This search proved unsuccessful. This molecule was also part of a larger

search for refractory compounds carried out by Turner [67]; again it was not found.

Even with this interest from the astrophysical community, only three high resolution gas phase spectroscopic studies have been made of MgS. The initial vibrational analysis of the $B\ ^1\Sigma^+ - X\ ^1\Sigma^+$ optical transition of the main isotopomer, $^{24}Mg^{32}S$, was done by Wilhelm [74] in 1932. This work was extended by Marcano and Barrow [75], who measured the rotationally resolved absorption spectrum of the same transition. They determined an equilibrium bond length and also measured the isotopic shifts of the other two $Mg^{32}S$ isotopomers, $^{25}Mg^{32}S$ and $^{26}Mg^{32}S$. The most recent study was that of the millimetre wave spectrum of the main isotopomer by Takano *et al.* , mentioned above [73]. In all of these studies, a furnace system was used to produce MgS by reaction of magnesium and sulfur in the gas phase.

This chapter presents the low frequency pure rotational spectrum of MgS. This work was undertaken as a test of the laser ablation source. Of the four isotopomers studied, $^{24}Mg^{34}S$ has been observed for the first time. Nuclear hyperfine structure due to the ^{25}Mg nucleus has been resolved and its quadrupole coupling constant determined. This is the first measurement of a metal quadrupole coupling constant for an alkaline earth metal sulfide molecule. The equilibrium geometry has been obtained by two methods and the results have been compared with those of previous studies.

5.2 Experimental Details

Magnesium sulfide was produced by reacting ablated magnesium metal (rod from A. D. MacKay, 99.9%) with OCS present as 0.2−0.5% in Ar carrier gas. Magnesium sulfide was produced in sufficient quantity to observe the $^{24}Mg^{32}S$ isotopomer $J = 1 - 0$ transition in 5 cycles. Since this result was satisfactory for testing purposes, no attempt was made to use any other sulfur-containing compound in the gas mixture.

5.3 Observed Spectra and Analyses

The $J = 1 - 0$ pure rotational transition near 16 GHz was the only transition of MgS available in the frequency range of the spectrometer. It was measured for 4 isotopic species in natural abundance: those for all 3 isotopes of Mg with ^{32}S, specifically ^{24}Mg^{32}S, ^{25}Mg^{32}S, and ^{26}Mg^{32}S, and one isotopomer containing ^{34}S, namely ^{24}Mg^{34}S. The natural abundances of these species range from 74.7% for the main isotopomer, ^{24}Mg^{32}S, to 3.3% for ^{24}Mg^{34}S.

The transition frequency for the main isotopomer was predicted using the millimetre wave constants [73]; the transition was found within 20 kHz of the calculated frequency. This microwave transition was fit together with the millimetre wave data, using Pickett's nonlinear least squares fitting program, SPFIT [76], to obtain the rotational constant, B_0, and centrifugal distortion constant, D_0. A relative weighting of 900:1 was given to the microwave line with respect to the millimetre wave data, to take account of the estimated experimental accuracies. The transition frequencies are listed in Table 5.1. The constants derived from the fit are listed in Table 5.2 under the heading Combined Fit. Also listed are the rotational constants obtained from the millimetre wave study of Takano *et al.* [73]. As was expected, there is not a significant change in the B_0 and D_0 values with the addition of the microwave transition.

The vibrational temperature was sufficiently high that the $J = 1 - 0$ transition could be measured for the main isotopomer in the $v = 1$ state. The frequency was predicted using the rotational constants from Marcano and Barrow [75]. The transition was found within 400 kHz of the prediction. The observed frequency is listed in Table 5.1. B_0 and B_1 were calculated from the $v = 0$ and $v = 1$ transition frequencies by assuming that D_0 and D_1 were equal to D_0 from the combined fit described above. Use of D_1 constant scaled according to the values of Marcano and Barrow [75] introduced no significant

variation in B_1. The B_e and α_e constants were then calculated directly from B_0 and B_1 using Eq. (2.16), which is shown here for reference

$$B_v = B_e - \alpha_e\left(v+\frac{1}{2}\right) + \gamma_e\left(v+\frac{1}{2}\right)^2 + ...$$

This expression was truncated following the α_e term. The constants obtained are listed in Table 5.2 under the heading Direct Calculation. Fig. 5.1 shows the two measured $J = 1 - 0$ transitions for $^{24}Mg^{32}S$.

The main isotopomer B_0 value was used to predict the transition frequencies for $^{26}Mg^{32}S$ and $^{24}Mg^{34}S$ by scaling B_0 using the reduced masses. Again the transitions were found very close to the predicted frequencies (within 1 MHz). Since only one transition was available for each of the minor isotopomers, rotational constants were calculated by holding D_0 fixed at a value obtained by scaling the main isotopomer D_0 value inversely as the square of the reduced mass. The transition frequencies and derived constants are listed in Table 5.3.

Searching for $^{25}Mg^{32}S$ was not quite so straightforward as it had been for the other isotopomers. Since the ^{25}Mg nucleus has a spin, I, of $\frac{5}{2}$, the transition was split into three components, with consequently lower signal intensity. In addition, an initial estimate for the quadrupole coupling constant turned out to be much larger than the value eventually found, so the search region was larger than necessary. The B_0 value was predicted by the same procedure used for the other minor isotopomers. All the nuclear hyperfine structure was observed within one cavity width. The transition was quite weak, and a very large number of averaging cycles was needed to see it. The spectrum shown in Fig. 5.2 was the result of $2\frac{1}{2}$ hours of signal accumulation. The frequencies of the three hyperfine components are listed in Table 5.4. These were fit using the SPFIT program [76] to determine the B_0 rotational constant and $eQq(^{25}Mg)$, which are listed in Table 5.5. Again, the D_0 constant was held fixed at the value scaled from that of

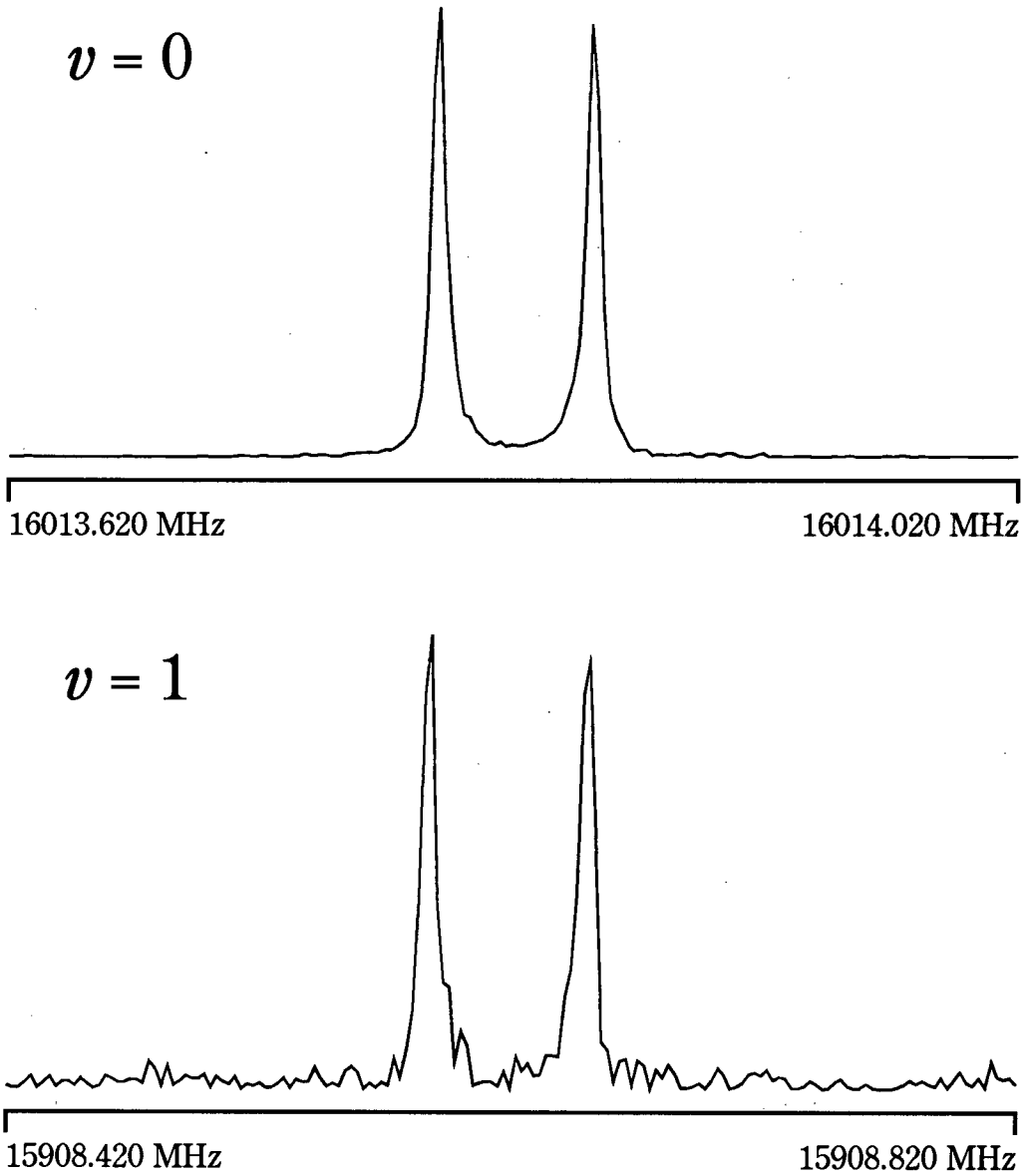

Figure 5.1: The $J = 1 - 0$ rotational transition of $^{24}Mg^{32}S$ was measured in both the $v = 0$ and $v = 1$ vibrational states. Each spectrum was measured with 1000 averaging cycles. The microwave excitation frequencies were 16013.820 MHz and 15908.620 MHz for the $v = 0$ and $v = 1$ transitions respectively. 4 K data points were measured for each spectrum with a 50 ns sampling interval and each power spectrum is displayed as an 4 K transformation.

$^{24}Mg^{32}S$ by the inverse square of the reduced mass.

5.4 Discussion

5.4.1 Equilibrium Bond Distance

Sufficient data were available that both isotopic substitution and the vibrational data could be used to determine the equilibrium bond length, r_e. Since isotopic data were available for both atoms, a complete substitution structure (r_s) could be calculated for the main isotopomer, $^{24}Mg^{32}S$. This method is described in detail in Sec. 2.4. The distance of an atom from the centre of mass, z_i, is given by Eq (2.62)

$$z_i{}^2 = \left(\frac{1}{\mu}\right)\Delta I_B^0$$

The calculated values z_i, for z_{Mg} and z_S, and the resulting r_s value with estimated uncertainties, are given in Table 5.6. For a diatomic molecule, the r_e value can be evaluated from Eq. (2.61):

$$r_e = 2r_s - r_0$$

using the r_0 value determined from B_0 for $^{24}Mg^{32}S$. This r_e value is listed in Table 5.7 as r_e (Subst.).

A second value for r_e, calculated directly from B_e, is also listed in Table 5.7 as r_e (Vibr.). The uncertainty given reflects those of the rotational constants, the fundamental constants and the atomic masses. It takes no account of electronic effects: the value of r_e in the Born-Oppenheimer approximation can be expected to differ by $\sim 10^{-5}$ Å, and possibly more [33]. The uncertainty in calculating r_e is discussed further in Secs. 2.4 and 6.5.1.

For comparison, Table 5.7 also contains the r_e value determined by Marcano and

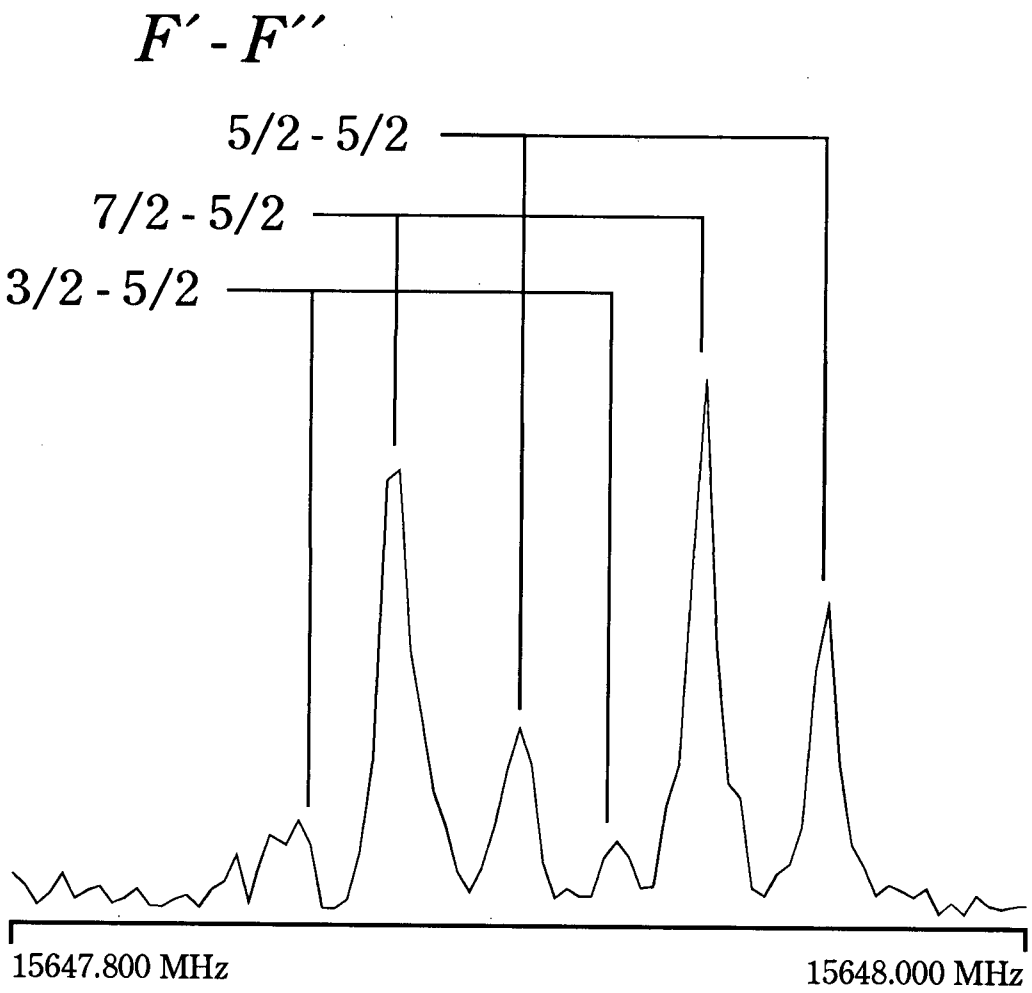

Figure 5.2: The $J = 1 - 0$ transition of $^{25}Mg^{32}S$ showing hyperfine structure due to ^{25}Mg nuclear quadrupole coupling. The excitation frequency was 15 647.80 MHz. The corresponding time domain signal consists of 4 K points and was recorded with 10 000 averaging cycles. The power spectrum was obtained after an 8 K transformation. Line positions of the labelled transitions and the constants obtained are listed in Tables 5.4 and 5.5, respectively.

Barrow in their optical study [75]; they gave no estimate of the uncertainty. The two new values agree with that of the optical study.

5.4.2 Nuclear Quadrupole Hyperfine Structure

The nuclear quadrupole coupling constant, $eQq(^{25}\mathrm{Mg})$, is the first metal nuclear quadrupole coupling constant measured for an alkaline earth sulfide molecule. Therefore comparisons cannot be made to similar molecules. However, it can be used to gain insight into the electron charge distribution at the magnesium nucleus. In terms of simple bonding theories, the MgS bond is ionic, with the molecule containing Mg^{2+} and S^{2-} ions. At infinite separation, both ions are spherically symmetric, making any nuclear quadrupole coupling constants zero. Since Mg^{2+} has the same electron configuration as Ne ($1s^2 2s^2 2p^6$), the non-zero ^{25}Mg coupling constant could be considered as due to a small "hole" in the $2p$ configuration, resulting from a $3s \leftarrow 2p$ excitation induced by the proximity of the S^{2-} ion.

The coupling constant can thus be interpreted in terms of unbalanced p-electrons using the Townes-Dailey model [17]. This was discussed in Sec. 2.3.1 and Eq. (2.43) is reprinted here substituting in the appropriate nuclear quadrupole coupling constants for ^{25}MgS:

$$eQq(^{25}\mathrm{Mg}) = \left(n_z - \frac{n_x + n_y}{2}\right) eQq_{210}(^{25}\mathrm{Mg})$$

Although a value for $eQq_{210}(^{25}\mathrm{Mg})$ is unavailable, that of $eQq_{310}(^{25}\mathrm{Mg})$ is known: -16 MHz [2]. It is expected that $eQq_{210}(^{25}\mathrm{Mg})$ will be a larger negative value since these constants are proportional to $\langle r^{-3} \rangle$, where r is the distance from the nucleus to an electron in the orbital in question. From the expression above it can be seen that the term relating the quadrupole coupling constants is very small and negative. This suggests that the electron density in the $2p_x$ and $2p_y$ orbitals is slightly greater than that in the $2p_z$ orbital, making

the electron cloud around the Mg nucleus slightly oblate in shape.

5.5 Conclusion

Measurement of the spectra of four isotopomers of MgS, including species of low abundance, has demonstrated the utility and sensitivity of the new laser ablation system. These experiments represent the first time MgS has been detected by FTMW spectroscopy. An equilibrium bond length has been obtained for MgS, along with the ^{25}Mg quadrupole coupling constant.

Table 5.1: Observed frequencies for $^{24}Mg^{32}S$ in MHz.

Transition				Observed Frequency[a]	Obs.-Calc.[b]
v'	J'	v''	J''	(MHz)	(kHz)
0	1	0	0	16 013.8215	−0.2
1	1	1	0	15 908.6190	
0	14	0	13	224103.178	26
0	16	0	15	256086.116	−1
0	17	0	16	272072.920	−12
0	18	0	17	288056.376	3
0	19	0	18	304036.237	−1
0	22	0	21	351952.415	12
0	23	0	22	367915.973	−12

[a] $J = 1 - 0$ data from present work. Other data taken from millimeter wave study [73].
[b] Observed minus calculated frequencies from combined fit of all $v = 0$ transitions. See Sec. 5.3 for details.

Table 5.2: Molecular constants calculated for $^{24}Mg^{32}S$ in MHz.

Parameter	Combined Fit[a,b]	Direct Calculation[c,d]	Lit.[g]
B_0	8006.92739(45)	8006.9273(5)	8006.9278(15)
B_1		7954.3260(5)	
D_0	0.00827291(66)	[0.008273[e]]	0.0082744(19)
D_1		[0.008273[e]]	
B_e		8033.2280(6)[f]	
α_e		52.6013(7)[f]	

[a] Fit combining present results and millimeter wave data [73].
[b] One standard deviation in parentheses, in units of least significant digit.
[c] B_0 and B_1 calculated from measured $J = 1 - 0$ frequencies.
[d] Estimated errors reflecting measurement uncertainty given in parentheses, in units of least significant digit.
[e] Centrifugal distortion constants, D_0 and D_1, were held fixed at D_0 value determined in combined fit; for detail see Sec. 5.3.
[f] B_e and α_e calculated from B_0 and B_1.
[g] From millimeter wave study of Takano *et al.* [73]. Three standard deviations in parentheses, in units of least significant digit.

Table 5.3: Frequencies for the $J = 1 - 0$ transition of isotopomers of MgS and derived B_0 values in MHz.

Isotopomer	Observed Frequency	B_0[a]	D_0
$^{26}Mg^{32}S$	15311.4750	7655.7526	[0.007563]
$^{24}Mg^{34}S$	15611.1768	7805.6041	[0.007863]

[a] Calculated by holding centrifugal distortion constant fixed at value scaled from that calculated for $^{24}Mg^{32}S$ in combined fit.

Table 5.4: Frequencies of measured hyperfine components of $^{25}Mg^{32}S$ in MHz.

Transition				Observed Frequency[a]
J'	F'	J''	F''	
1	3/2	0	5/2	15647.8878(21)
1	7/2	0	5/2	15647.9053(31)
1	5/2	0	5/2	15647.9300(09)

[a] Observed minus calculated frequencies in parentheses, in units of the least significant digit.

Table 5.5: Molecular constants for $^{25}Mg^{32}S$ in MHz.

Parameter	Value[a]
B_0	7823.9703(6)
D_0	[0.007900[b]]
eQq	0.1366(92)
ν_o	15647.9090[c]

[a] One standard deviation in parentheses, in units of the least significant digit.
[b] Centrifugal distortion constant held fixed in fit at value scaled from that calculated for $^{24}Mg^{32}S$ in combined fit.
[c] Hypothetical unsplit frequency calculated from B_0 and D_0 values.

Table 5.6: Substitution structure results for $^{24}Mg^{32}S$ in Å[a].

	z_{Mg}	z_S	r_s
$^{24}Mg^{32}S$	1.225213(19)	0.919118(23)	2.144331(30)

[a] Estimated uncertainties in parentheses, in units of least significant digit, reflect the uncertainties in the rotational constants, the fundamental constants and the atomic masses only.

Table 5.7: Equilibrium bond length calculated for $^{24}Mg^{32}S$ in Å[a].

	Subst.[b]	Vibr.[c]	Lit.[d]
$^{24}Mg^{32}S$	2.142573(60)	2.1425728(10)	2.1425

[a] Estimated uncertainties in parentheses, in units of least significant digit, reflect the uncertainties in the rotational constants, the fundamental constants and the atomic masses only.
[b] Calculated from substitution data using $r_0 = 2.1460889(10)$Å.
[c] Calculated from vibrational data.
[d] From optical study by Marcano and Barrow [75].

Chapter 6

Pure Rotational Spectra of MgBr and AlBr

6.1 Introduction

Aluminium and magnesium are among the most abundant metals in the Earth's crust and both are quite reactive. The monobromide compounds of these metals differ in that MgBr is paramagnetic ($^2\Sigma^+$ ground electronic state) and AlBr is diamagnetic. Their electronic structures can be investigated through their hyperfine constants. The ionic character of the metal-halogen bond can be calculated from the halogen nuclear quadrupole coupling constant. The unpaired electron spin density in the alkaline earth monohalides (such as MgBr) can be calculated from the electron spin-nuclear spin coupling constants. These hyperfine interactions in the pure rotational spectra of two metal monohalides, magnesium monobromide and aluminium monobromide, will be used to examine bonding in the species.

Hyperfine structures in the spectra of only two magnesium monohalides, MgF and MgCl, have been investigated in any detail. Electron spin resonance and millimetre wave spectroscopy have been used to observe the spectra of MgF [77–79], and Fourier transform microwave (FTMW) and millimetre wave spectroscopy have been applied to the investigation of MgCl [45, 80]. These methods have provided precise hyperfine parameters which have been used to compare bonding trends within the molecules. Though MgF

and MgCl are quite ionic, they appear to have greater covalent character than the other alkaline earth monofluorides and monochlorides [79]. The present study was undertaken to determine whether magnesium monobromide follows this trend.

The spectroscopy of magnesium monobromide has been of interest since 1906, when Olmsted photographed the band spectra of several alkaline earth halides, including MgBr, in emission [81]. This work was extended, in 1928, by Walters and Barratt, who made an absorption study of the same region [82]. The first vibrational analysis was done of the $A^2\Pi - X^2\Sigma^+$ transition by Morgan in 1936 [83]. In this study, the band heads due to the two isotopes of bromine could not be completely resolved. Several other studies have examined the $A-X$ transition [84,85] and transitions from higher excited electronic states to the ground state [86,87]. MgBr has been included in larger theoretical studies of spin-orbit splittings [88] and Franck-Condon factors [89]. Recently, both theoretical and experimental studies have been made of predissociation in the $A^2\Pi$ state [90,91]. There has however been only one study of a rotationally resolved spectrum. In 1969, Patel and Patel did a partial rotational analysis of the $A^2\Pi - X^2\Sigma^+$ (0-0) band [92]. They, too, did not resolve any isotope effects. There has been no previous microwave spectroscopic study of MgBr.

Aluminium monobromide provides an interesting comparison for magnesium monobromide, as both metals are in the same row of the periodic table. Microwave and millimetre wave spectroscopy have been used to investigate the hyperfine structure of AlF [93–96] and AlCl [54,93,97,98]. For AlBr, millimetre wave spectra have been recorded for both isotopomers in several vibrational states ($v = 0 - v = 5$) [97]. Nuclear quadrupole hyperfine structure has been measured only for the $J = 1 - 0$ transition of $Al^{79}Br$ by Hoeft *et al.* [98]. The measurements described in this chapter were made to provide further information on the hyperfine structure.

The electronic spectroscopy of aluminium monobromide has been examined in some detail. The initial investigations were made in the 1930's by Crawford and Ffolliott [99] and by Miescher [100, 101]. From these studies two electronic transitions, $A\ ^1\Pi - X\ ^1\Sigma^+$ and $a\ ^3\Pi - X\ ^1\Sigma^+$, were identified. The vibrational analyses of the $A\ ^1\Pi - X\ ^1\Sigma^+$ transition were made by both Howell [102] and Mahanti [103] in 1935. Jennergren made the first rotational analysis of this transition in 1948 [104, 105]. In further studies, predissociation in the $A\ ^1\Pi$ state was identified [106]. This was investigated in detail by grating spectroscopy [107–109], pulsed dye laser spectroscopy [110] and Fourier transform spectroscopy [111]. Langhoff *et al.* [112] calculated spectroscopic constants for the $A\ ^1\Pi$ and $X\ ^1\Sigma^+$ states of AlBr as part of their theoretical study of the aluminium monohalides. Vibrational analysis of the $a\ ^3\Pi - X\ ^1\Sigma^+$ electronic transition was made by Sharma [113] in 1951. Lakshminarayana and Haranath [114] carried out the first rotational analysis of this transition. Their work was extended by Griffith and Mathews [108] and by Bredohl *et al.* [115]. Bredohl *et al.* also identified a third electronic transition, the $b\ ^3\Pi - X\ ^1\Sigma^+$ system, and did a vibrational analysis. More recently, Uehara *et al.* used a Fourier transform infrared spectrometer to measure the ro-vibrational spectrum of aluminium bromide in emission [116]. They combined their results with those of the millimetre wave study [97] to determine Dunham potential coefficients.

This chapter describes the pure rotational spectra of MgBr and AlBr in their ground and first excited vibrational states. This is the first complete rotational analysis of magnesium monobromide. The rotational, fine and hyperfine parameters of both isotopomers of MgBr, in its $^2\Sigma^+$ ground electronic state, have been determined. These have been used to evaluate the equilibrium bond distance and to draw conclusions about unpaired electron density in the molecule. The first measurement of the hyperfine spectrum of $Al^{81}Br$ has been made. Nuclear quadrupole, spin-rotation and spin-spin coupling constants have

been determined for both isotopomers of aluminium monobromide. The hyperfine parameters of MgBr and AlBr have also been used to investigate the ionic character of these species and to make comparisons with other metal monohalides.

6.2 Experimental Details

MgBr and AlBr were produced by reaction of Br_2, which was present as $0.05 - 0.2\%$ in Ar carrier gas, with ablated Mg(rod from Goodfellow 99.9%) or ablated Al(rod from Alfa AESAR 99.999%), respectively. The strongest transitions could be seen easily with fewer than 5 averaging cycles. As was found in the FTMW investigation of AlCl [54], a very low concentration of the halogen precursor, Br_2, had to be used to promote formation of the metal monohalide rather than di- and trihalides. When measuring the spectrum of the free radical MgBr, a set of three mutually perpendicular Helmholtz coils was used to collapse the Zeeman splitting due to the earth's magnetic field. Use of these coils is discussed in Section 3.8.

6.3 Assignment of Spectra

6.3.1 MgBr

The search for the pure rotational transitions of MgBr presented a challenge since there were no precise rotational constants to provide search parameters. The one rotational constant available was from the partial analysis of the $A - X$ band [92]; it was not well determined and was for an unspecified isotopomer. Also the spectrum of MgBr is complicated by the fact that the two main isotopomers have almost equal natural abundance (40.04% and 38.95% for $^{24}Mg^{79}Br$ and $^{24}Mg^{81}Br$, respectively) and is further complicated by hyperfine structure, since each isotope of bromine has a nuclear spin of $I = \frac{3}{2}$. Since there have been no theoretical studies of the spectroscopic properties of

MgBr, estimates also had to be made for the fine structure and hyperfine parameters.

This problem was approached by making a series of predictions by examining trends within the measured spectroscopic parameters of several magnesium and calcium monohalides. Then the predicted $N = 1 - 0$ spectra were compared and a wide initial search range ($\sim$ 200 MHz) was established. Within this range, 10 transitions were found. The search was continued and 28 lines in total were measured for the $N = 1 - 0$ transition. These lines belong to four overlapped groups, one for each of the two isotopomers, $^{24}Mg^{79}Br$ and $^{24}Mg^{81}Br$, in each of the $v = 0$ and $v = 1$ vibrational states. The initial assignment was made using pattern recognition and then confirmed using the observed Zeeman patterns and the prediction of the $N = 2 - 1$ transition. In the end, a rich hyperfine spectrum comprised of 50 components was measured between 9.4 and 20.1 GHz. Only the two lowest N rotational transitions were available for study in the frequency range of the spectrometer. Example spectra are shown in Figs. 6.1 and 6.2. Figure 6.3 shows all observed $v = 0$ and $v = 1$ components of the $N = 1 - 0$ transition for $Mg^{79}Br$ and $Mg^{81}Br$. The observed transitions for the $^{24}Mg^{79}Br$ and $^{24}Mg^{81}Br$ species are listed in Tables 6.1 and 6.2, respectively. Spectra for species containing the minor isotopes of magnesium, ^{25}Mg and ^{26}Mg, were not sought.

6.3.2 AlBr

In contrast to MgBr, the initial search range for AlBr was quite narrow because the rotational and centrifugal distortion constants of both isotopomers were known from the millimetre wave study [97]. However as was found for MgBr, only the two lowest J rotational transitions of AlBr were available in the frequency range of the spectrometer. Nuclear quadrupole interactions due to both Br($I = \frac{3}{2}$ for both isotopes, ^{79}Br and ^{81}Br) and $^{27}Al(I = \frac{5}{2})$ were included in the prediction using the ^{27}Al and ^{79}Br nuclear

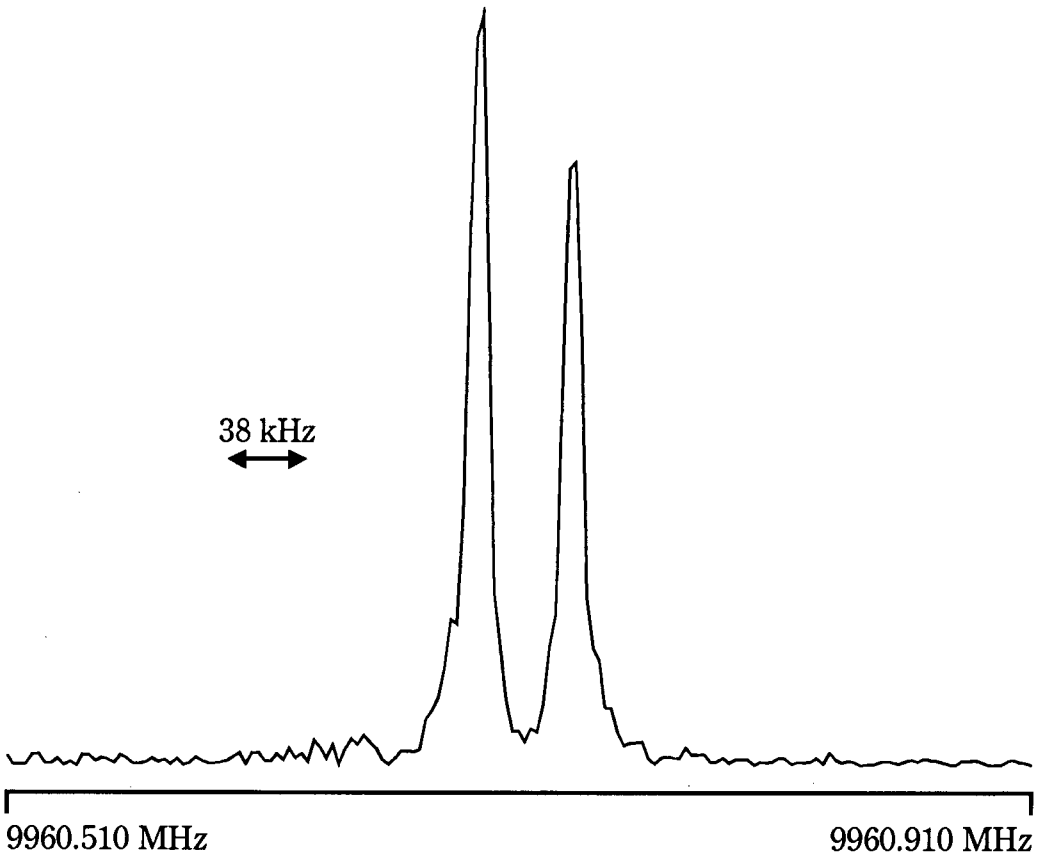

Figure 6.1: The $N = 1-0$, $J = 3/2-1/2$, $F = 2-2$ transition of $^{24}Mg^{81}Br$ was measured using a set of mutually perpendicular Helmholtz coils to remove the effects of the earth's magnetic field. This spectrum was obtained with 50 averaging cycles. The microwave excitation frequency was 9960.710 MHz. 4 K data points were measured with a 50 ns sampling interval and the power spectrum is displayed as an 8 K transformation.

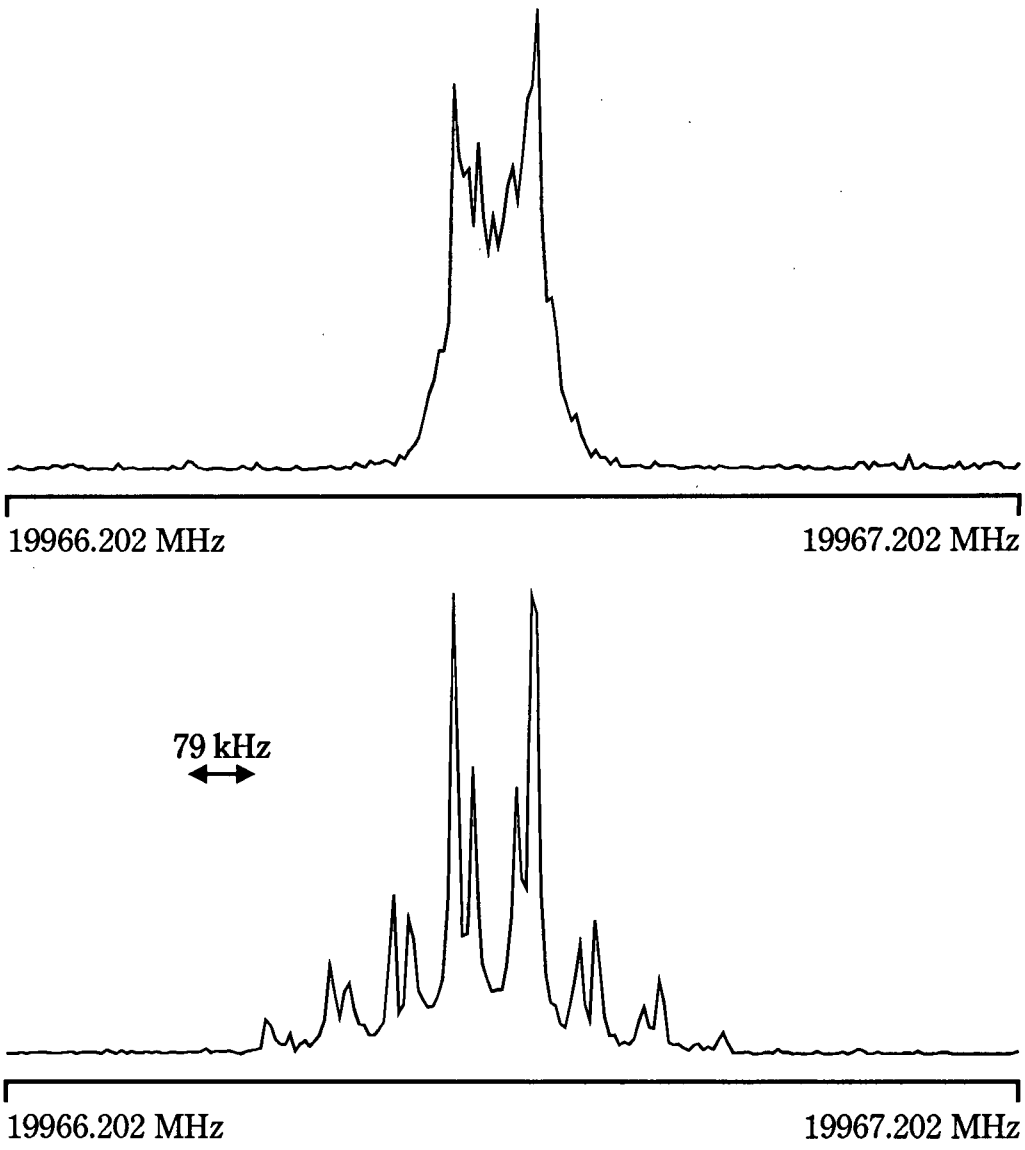

Figure 6.2: Two spectra of the $N = 2 - 1$, $J = 5/2 - 3/2$, $F = 4 - 3$ transition of $^{24}Mg^{79}Br$. The upper spectrum was measured with 400 averaging cycles and using the Helmholtz coils to cancel the earth's magnetic field. The lower spectrum was obtained with 1000 averaging cycles. The Helmholtz coils were not used for this measurement and thus the first order Zeeman splitting due to the earth's magnetic field was observed. For both spectra, the excitation frequency was 19966.702 MHz, 4 K data points were recorded and the power spectra shown here were obtained with an 8 K transformation.

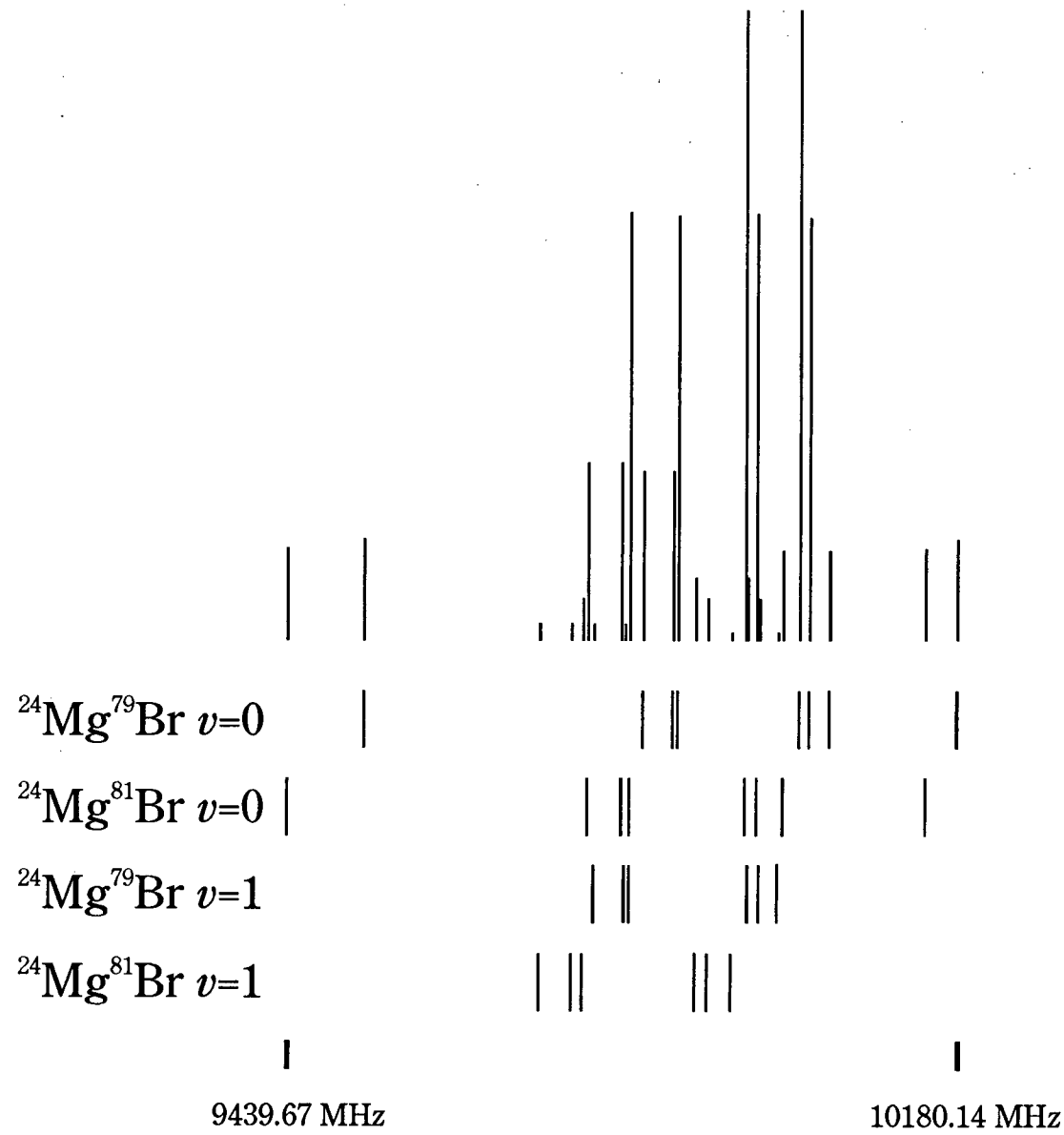

Figure 6.3: Stick spectrum showing all observed $v = 0$ and $v = 1$ hyperfine components of the $N = 1 - 0$ rotational transition for $Mg^{79}Br$ and $Mg^{81}Br$. This composite was produced by using the measured transition frequencies along with the predicted transition intensities.

quadrupole coupling constants reported for $Al^{79}Br$ by Hoeft *et al.* [98].

The $J = 1 - 0$ transition of $Al^{79}Br$ was measured first. Seventeen hyperfine components were observed and were assigned using the coupling scheme $\mathbf{J} + \mathbf{I}_{Br} = \mathbf{F_1}$; $\mathbf{F_1} + \mathbf{I}_{Al} = \mathbf{F}$. An overview spectrum of the $J = 1 - 0$ transition, shown in Fig. 6.4, shows the relative magnitude of the Br and Al splittings: the Br quadrupole coupling splits the transition into three lines which are further split by the Al quadrupole coupling. A preliminary fit was made holding D_0 fixed at the millimetre wave value to obtain improved ^{27}Al and ^{79}Br nuclear quadrupole coupling constants and to determine the Al and ^{79}Br nuclear spin-rotation constants. The improved value of $eQq(^{79}Br)$ was scaled, by the ratio of nuclear quadrupole moments, to obtain a value for $eQq(^{81}Br)$ which was used to predict the $J = 1 - 0$ transition of $Al^{81}Br$. Sixteen hyperfine components were measured for this isotopomer. A further 13 lines were measured for each isotopomer for the $J = 2 - 1$ transition. The measured ground vibrational state transitions of $Al^{79}Br$ and $Al^{81}Br$ are listed in Tables 6.3 and 6.4, respectively. A method similar to that used for the $v = 0$ transitions was used to predict and measure the hyperfine components of the $J = 1 - 0$ and $J = 2 - 1$ transitions in the $v = 1$ excited vibrational state for $Al^{79}Br$ and $Al^{81}Br$. The lines of $Al^{79}Br$ and $Al^{81}Br$ measured in the $v = 1$ vibrational state are also listed in Tables 6.3 and 6.4, respectively.

6.4 Analyses

The transitions for each vibrational state of each isotopomer of MgBr were fit separately using Pickett's exact fitting program, SPFIT [76]. This program employs a Hund's case ($b_{\beta J}$) coupling scheme; $\mathbf{N} + \mathbf{S} = \mathbf{J}$; $\mathbf{J} + \mathbf{I}_{Br} = \mathbf{F}$. The fit determined the rotational, centrifugal distortion and fine structure constants (B, D, and γ, respectively) as well as several hyperfine parameters for the bromine nucleus (the Fermi-contact constant, b_F, the

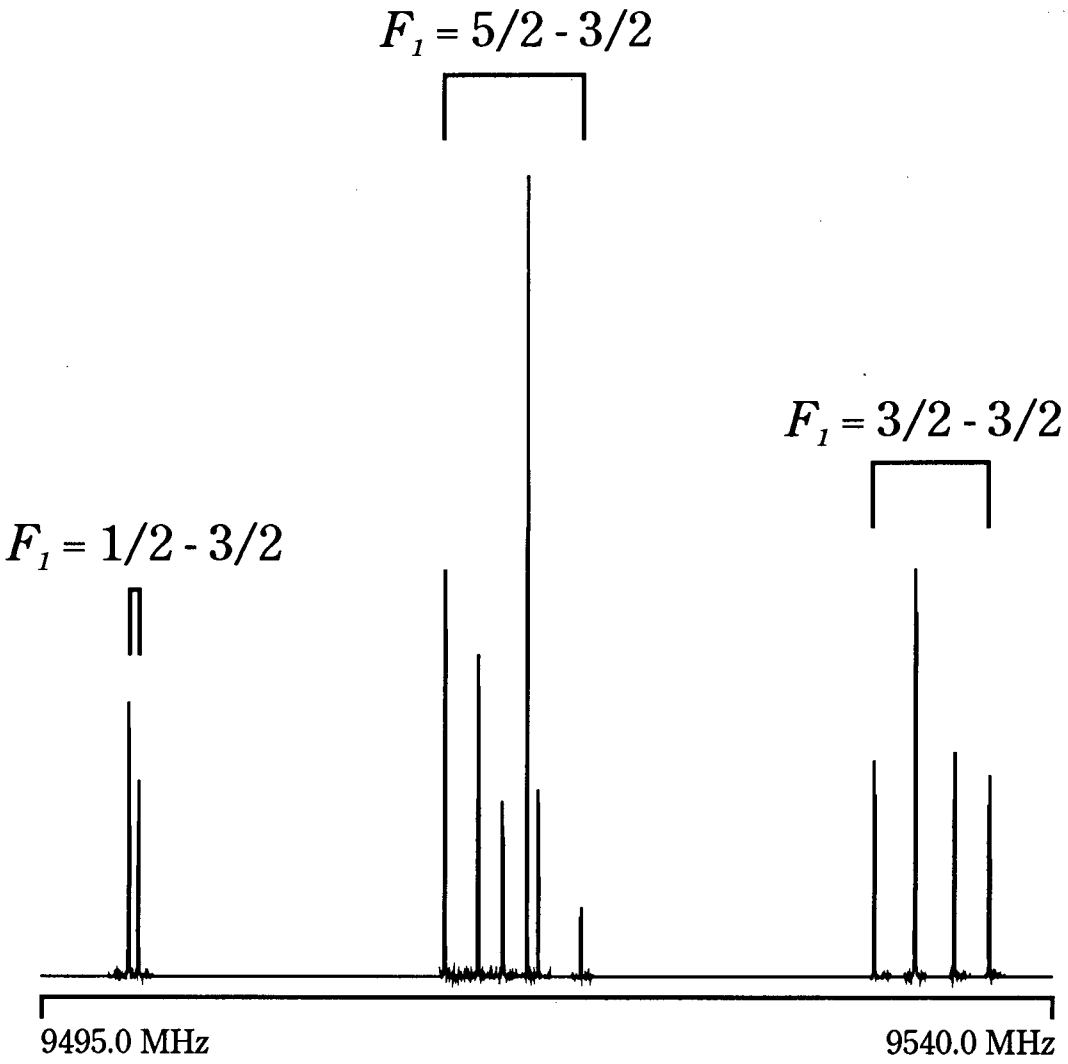

Figure 6.4: Composite spectrum of the $J = 1 - 0$ rotational transition of $Al^{79}Br$. The transition is split into three groups by the ^{79}Br nucleus and the further splitting within each group is due to the ^{27}Al nucleus. The results of twelve different microwave experiments were used to produce this composite. The individual power spectra were scaled to reproduce predicted intensities.

dipole-dipole interaction constant, c, the nuclear quadrupole coupling constant, eQq(Br) and the nuclear spin-rotation constant, C_I(Br)). All parameters determined are listed in Table 6.5. It is difficult to compare the rotational constants obtained in this study with that obtained by Patel and Patel [4932(15) MHz] since their study could not separate transitions due to the different isotopomers.

For AlBr, the transitions for each isotopomer in each vibrational state were fit separately using Pickett's exact fitting program SPFIT to determine the rotational and centrifugal distortion constants, B and D, along with the nuclear quadrupole coupling constants, eQq, and nuclear spin-rotation constants, C_I for both the aluminium and bromine nuclei and the nuclear spin-spin constant, α_{Al-Br}. The lines observed for the overlapped hyperfine components of the $J = 1 - 0$ transition were fit as blended lines using predicted intensities as weighting factors. The determined constants are listed in Table 6.6. The calculated rotational and centrifugal distortion constants agree quite well, within about one standard deviation, with those determined by Wyse and Gordy [97]. Also the nuclear quadrupole coupling constants, $eQq(^{27}\text{Al})$ and $eQq(^{79}\text{Br})$ determined for the $Al^{79}Br$ isotopomer are within one standard deviation of those determined by Hoeft *et al.* [98]. However, the nuclear quadrupole coupling constants determined in this study are two orders of magnitude more precise than those of Hoeft *et al.*.

The ratios of the fine and hyperfine parameters found for $^{24}Mg^{79}Br$ and $^{24}Mg^{81}Br$ and of the hyperfine parameters determined for $Al^{79}Br$ and $Al^{81}Br$ should be equal to the ratios of certain nuclear and molecular properties. The γ parameter ratio is equal to the inverse ratio of the reduced masses. The ratios of the hyperfine parameters are equal to the ratios of certain nuclear moments, specifically, the nuclear magnetic moments for b_F, c and C_I, and the nuclear electric quadrupole moments for eQq. The ratio of the nuclear spin-rotation constants also depends on the inverse ratio of the reduced masses.

These ratios have been calculated for the parameters derived for the two vibrational states of both MgBr and AlBr and are listed in Table 6.7 along with ratios of reduced masses and/or nuclear moments obtained from the literature. The ratios for eQq(Br) and c agree quite well with the ratios from the literature, within the calculated uncertainties. The C_I(Br) ratios also agree with ratios of the literature values, though the uncertainties are quite large. However for γ and b_F, this is not the case. This deviation observed for the γ and b_F ratios is due to vibrational effects, because, strictly speaking, the equilibrium values of the fine and hyperfine parameters should be used to calculate the ratios [117, 118]. To account for this, an expansion in terms of vibrational contributions, of the form

$$X_v = X_e + X_1(v + \frac{1}{2}), \tag{6.1}$$

was used to calculate the equilibrium values of each of the parameters. The vibrational dependencies of the four well determined parameters of MgBr, in MHz, can be summarised by the following expressions:

$$\begin{aligned}
\gamma_v(^{79}\mathrm{Br}) &= 179.6020(18) - 2.5944(24)\left(v + \frac{1}{2}\right) \\
\gamma_v(^{81}\mathrm{Br}) &= 178.5673(17) - 2.5708(21)\left(v + \frac{1}{2}\right)
\end{aligned}$$

$$\begin{aligned}
eQq_v(^{79}\mathrm{Br}) &= 109.3761(50) + 1.8744(69)\left(v + \frac{1}{2}\right) \\
eQq_v(^{81}\mathrm{Br}) &= 91.3736(49) + 1.5593(69)\left(v + \frac{1}{2}\right)
\end{aligned}$$

$$\begin{aligned}
b_{F_v}(^{79}\mathrm{Br}) &= 172.9049(25) - 1.1681(43)\left(v + \frac{1}{2}\right) \\
b_{F_v}(^{81}\mathrm{Br}) &= 186.3870(25) - 1.2580(43)\left(v + \frac{1}{2}\right)
\end{aligned}$$

$$c_v(^{79}\mathrm{Br}) = 206.5561(37) + 1.0464(53)\left(v + \frac{1}{2}\right)$$

$$c_v(^{81}\mathrm{Br}) = 222.6568(35) + 1.1215(50)\left(v+\frac{1}{2}\right).$$

The expressions for the vibrational dependence of the nuclear quadrupole coupling constants of AlBr, in MHz, are:

$$eQq_v(^{79}\mathrm{Br}) = 79.4193(19) - 1.4258(27)\left(v+\frac{1}{2}\right)$$
$$eQq_v(^{81}\mathrm{Br}) = 66.3427(20) - 1.1903(28)\left(v+\frac{1}{2}\right).$$

The ratios calculated using the equilibrium values of the parameters are also listed in Table 6.7. These equilibrium parameter ratios agree more consistently with the ratios from the literature, to within 1.5 times the calculated uncertainties. The γ and b_F constants are sufficiently well determined that vibrational effects on the ratios are evident; this reflects the high precision available from the FTMW technique.

6.5 Discussion

6.5.1 Equilibrium Bond Distance of MgBr

In the millimetre wave study of the similar molecule MgCl [119], the observed transitions were fit to Dunham coefficients from which a bond length could be determined. There are insufficient rotational and vibrational data for MgBr to employ this method. Instead, Eq. (2.16) was used:

$$B_v = B_e - \alpha_e\left(v+\frac{1}{2}\right) + \gamma_e\left(v+\frac{1}{2}\right)^2 \ldots$$

where B_e is the equilibrium rotational constant, B_v is the rotational constant of the vth vibrational state and α_e and γ_e are higher order vibrational correction terms. This expression was used in three different calculations to estimate the equilibrium rotational constant and equilibrium bond distance. The details of this calculation of r_e have been

discussed in Sec. 2.4. For the first method, Eq. (2.16) was truncated after the α_e term. Using the B_0 and B_1 data, B_e and α_e were determined for both isotopomers and from these r_e was determined using atomic masses and fundamental constants from Ref. 120. These results are listed in Table 6.8 under the heading Method I. In the second method, the higher order correction constant γ_e was substituted by $10^{-3} \cdot \alpha_e$ in Eq. (2.16). This value is similar to those found for CaBr [121] and BaCl [18]. Two more values of B_e and r_e were determined from the B_0 and B_1 data by employing this approximation. These are listed in Table 6.8 under Method II. The r_e obtained using Method II agrees fairly well with that calculated by Method I. The uncertainties given for each of these results, which are on the order of 10^{-6} Å, reflect the uncertainties in the rotational and fundamental constants only.

So far no account has been taken of electronic effects; these have been described in Sec. 2.4. An estimate of the order of magnitude of the effect of non-spherical charge distribution can be made by considering MgBr as the completely ionic molecule, Mg^+Br^-. The same estimate of γ_e was made as in Method II and B_e was calculated for the two isotopomers of MgBr; however to calculate r_e, ion masses were used instead of atomic masses. This provided a third estimate of r_e which is listed under Method III in Table 6.8. The difference in r_e obtained for Methods II and III is on the order of 10^{-5} Å; the uncertainty due to electronic effects is estimated to be of this order of magnitude. This is also expected to be a good measure of the deviation of r_e from that obtained in the Born-Oppenheimer approximation.

This estimate can be verified using AlBr, since the equilibrium bond distance in the Born-Oppenheimer approximation is known from the study of Wyse and Gordy [97]. In their study, B_e was calculated from the Dunham coefficient Y_{01} using a method after Bunker [31] which also accounted for the breakdown of the Born-Oppenheimer

approximation [30]. For this comparison, r_e was calculated for AlBr using the three methods described above. These values are listed in Table 6.9 along with the r_e value in the Born-Oppenheimer approximation from the millimetre wave study. The differences between the r_e values estimated by Methods I, II, and III and the Born-Oppenheimer r_e are all of the order of magnitude of 10^{-5}Å, which is equal to the estimate of uncertainty in r_e made above for MgBr.

Table 6.10 presents a summary of the r_e values calculated for MgBr by each method and also a best estimate of r_e, which is an average of the results of Methods II and III. These results can be compared to the two literature values, the r_0 value from the partial rotational analysis [92] and an r_e value from a recent *ab initio* study [90]. The results of this FTMW study have clearly provided the first accurate value for the equilibrium bond distance for magnesium monobromide.

6.5.2 Electron Spin-Nuclear Spin Hyperfine Parameters

The magnetic hyperfine constants b_F and c were used to characterise the bonding in MgBr *via* the unpaired electron spin densities in the bromine atomic orbitals. This method is discussed in detail in Sec. 2.3.3. The definitions of the Fermi contact and dipole-dipole interaction constants, Eq. (2.52) and Eq. (2.53), are shown here for reference

$$\begin{aligned} b_F &= \frac{8\pi}{3} g_e g_N \mu_B \mu_N |\Psi(0)|^2 \\ c &= \frac{3}{2} g_e g_N \mu_B \mu_N \left\langle (3\cos^2\Theta - 1)/r^3 \right\rangle . \end{aligned}$$

Values of $|\Psi(0)|^2$ and $\langle(3\cos^2\Theta - 1)/r^3\rangle$ were calculated for $Mg^{79}Br$ and $Ca^{79}Br$ from b_F and c using Eqs. (2.52) and (2.53) and constants from Ref. 120. These values are listed in Table 6.11. Also listed are corresponding values for the bromine atom, which were calculated by considering the unpaired electron to be in the bromine atom $4s$ orbital, for $|\Psi(0)|^2$, or the $4p_z$ orbital, for $\langle(3\cos^2\Theta - 1)/r^3\rangle$, and using atomic parameters calculated

by Morton and Preston [22]. A value of $\langle 3\cos^2\Theta - 1\rangle = \frac{4}{5}$ was used for the p_z orbital and a relativistic correction, on the order of 16.7%, was included for $|\Psi(0)|^2$ [22]. The unpaired spin densities, $\rho(s)$ and $\rho(p)$ listed in Table 6.11, were calculated for the $4s$ and $4p_z$ orbitals in MgBr and CaBr by taking ratios of the experimental molecular to calculated atomic values for $|\Psi(0)|^2$ and $\langle(3\cos^2\Theta - 1)/r^3\rangle$, respectively. From these, it can be seen that there is very little unpaired electron spin density on the bromine in these species. The unpaired electron can be considered to reside almost entirely on the metal, indicating that the radicals are almost completely ionic, M^+Br^-. The spin densities for MgBr, however, are approximately twice those of CaBr. This higher unpaired spin density on the halogen nucleus, as compared to the other alkaline earth monohalides, has been observed for both MgF [79] and MgCl [45]. It appears that the amount of covalent character in the metal-halide bond increases as the mass of the alkaline earth atom decreases [79] and these results for MgBr are consistent with this observation.

6.5.3 Nuclear Quadrupole Coupling Constant

The ionic character of the metal bromide bond can be calculated from the nuclear quadrupole coupling constant, $eQq(\mathrm{Br})$. This method has been described in Sec. 2.5. Eq. (2.71) is given here for reference

$$i_c = 1 + \frac{eQq(\mathrm{Br})}{eQq_{410}(\mathrm{Br})},$$

where $eQq_{410}(^{79}\mathrm{Br})$ is -769.76 MHz [2]. Table 6.12 presents the ionic character calculated for MgBr, AlBr and several other metal monobromide species using this expression. For the alkaline earth and alkali metal monobromides, these results follow the expected periodic trends in electronegativity; MgBr and NaBr are less ionic than CaBr and KBr, respectively, and the greatest difference in ionic character observed is between MgBr and KBr. These results also support the observation from analysis of the electron spin-nuclear

spin hyperfine constants that the magnesium monohalides exhibit more covalent bond character than the corresponding calcium species. However, for the Al and Ga species, the calculated ionic character results do not appear follow the trend expected from the literature electronegativity values.

This discrepancy can be investigated by calculating the electronegativity difference between the two atoms in the molecule from its ionic character. These relations are described in detail in Sec. 2.3.1. Eq. (2.78), given here for reference,

$$i_c = 1.15 \exp\left[-\frac{1}{2}(2-\Delta x)^2\right] - 0.15$$

was used to calculate the difference in electronegativities, Δx, for AlBr and GaBr [122] using the ionic characters obtained from the bromine nuclear quadrupole coupling constants. From these Δx values, the electronegativities of aluminium and gallium were determined using halogen electronegativity values taken from Ref. 2. This method was repeated using the corresponding monochloride species, AlCl [54] and GaCl [123]. The average electronegativity values are listed in Table 6.12 as x_M(calc.).

This difference between the literature aluminium electronegativity value, 1.5 [2], and that calculated from the nuclear quadrupole coupling constants, 1.3, was also noted by Wyse and Gordy [97]. This difference was ascribed to the method used to obtain the electronegativity values. The literature value was obtained from solid phase data where aluminium would most likely be present in its trivalent state rather than its monovalent state and the electronegativity values are expected to be 0.2 to 0.3 higher for trivalent aluminium than for monovalent aluminium [97]. Wyse and Gordy estimated the electronegativity of monovalent aluminium to be 1.3. This value agrees with that determined from the more accurate nuclear quadrupole coupling constants for AlBr and AlCl [54] obtained by FTMW spectroscopy.

The Al nuclear quadrupole coupling constants can be related to the degree of *sp*

hybridisation on the Al atom. This will be discussed in conjunction with the Al nuclear quadrupole coupling constants of aluminium isocyanide and other related aluminium halides in Sec. 7.5.1.

6.5.4 AlBr Nuclear Spin-Spin Constant

The nuclear spin-spin constant, α_{Al-Br}, should be consistent with the calculated bond length. Using Eq. (2.58) from Sec. 2.3.3, α_{Al-Br} can be expressed as

$$\alpha_{Al-Br} = \frac{-3\mu_N^2 g_{Al} g_{Br}}{r_{Al-Br}^3}$$

where μ_N is the nuclear magneton and g_{Al} and g_{Br} are the nuclear g-factors for the Al and Br nuclei. Internuclear bond distances of 2.31(13) Å and 2.47(17) Å were calculated from the nuclear spin-spin constants of $Al^{79}Br$ and $Al^{81}Br$, respectively. The large uncertainties in the estimated bond distances are due to uncertainties in the respective constants. Despite the large uncertainties, the estimated internuclear distances agree with the r_e value of ~ 2.29Å.

6.6 Conclusion

The first complete rotational analysis of the spectrum of magnesium monobromide has been made. Accurate rotational and centrifugal distortion constants have been determined as well as new fine and hyperfine parameters. The first accurate equilibrium bond length has been determined for MgBr. The ^{81}Br nuclear quadrupole structure of $Al^{81}Br$ has been observed for the first time. Improved nuclear quadrupole coupling constants have also been obtained for $Al^{79}Br$ and nuclear spin-rotation and nuclear spin-spin constants have been determined for both isotopomers. The analyses of the hyperfine structure has shown that the bonding in MgBr and AlBr follow the trends predicted from

electronegativities. Also MgBr has been found to follow the same trends in bonding as MgF and MgCl: all three species exhibit greater covalent character than the corresponding Ca and other alkaline earth monohalides.

Table 6.1: Measured frequencies of $N = 1 - 0$ and $N = 2 - 1$ transitions of $^{24}Mg^{79}Br$ in $v = 0$ and $v = 1$ vibrational states.

Transition						$v = 0$	Obs. - calc.	$v = 1$	Obs. - calc.
N'	J'	F'	N''	J''	F''	(MHz)	(kHz)	(MHz)	(kHz)
1	1/2	1	0	1/2	2	9524.7196	−0.2		
1	3/2	1	0	1/2	2	9835.8658	−0.5	9780.8303	1.6
1	1/2	1	0	1/2	1	9868.9931	0.3	9814.4948	0.0
1	1/2	2	0	1/2	1	9873.9752	−1.1	9820.2456	−1.4
1	3/2	3	0	1/2	2	10007.5349	0.5	9950.8962	0.7
1	3/2	2	0	1/2	2	10018.5122	0.4	9963.9149	0.0
1	3/2	0	0	1/2	1	10040.5588	1.2	9983.8199	0.2
1	3/2	1	0	1/2	1	10180.1367	−2.6		
2	3/2	3	1	1/2	2	19806.7336	1.3	19697.8937	1.1
2	5/2	2	1	3/2	2	19860.1058	−0.1	19748.6261	−0.5
2	3/2	2	1	1/2	1	(19854.946)[a]			
2	5/2	3	1	3/2	2	19954.1031	0.2	19842.2139	−0.6
2	5/2	3	1	3/2	3	19965.0798	−0.5		
2	5/2	4	1	3/2	3	19966.6855	−1.1	(19854.946)[a]	
2	5/2	2	1	3/2	1	20042.7515	0.1		

[a] Blended lines not included in fit.

Table 6.2: Measured frequencies of $N = 1 - 0$ and $N = 2 - 1$ transitions of $^{24}Mg^{81}Br$ in $v = 0$ and $v = 1$ vibrational states.

Transition						$v = 0$	Obs. - calc.	$v = 1$	Obs. - calc.
N'	J'	F'	N''	J''	F''	(MHz)	(kHz)	(MHz)	(kHz)
1	1/2	1	0	1/2	2	9439.6747	0.6		
1	3/2	1	0	1/2	2	9774.2372	−1.8	9719.8268	−0.9
1	1/2	1	0	1/2	1	9810.8129	−0.1	9756.6116	−0.1
1	1/2	2	0	1/2	1	9821.2344	−1.4	9767.9234	0.2
1	3/2	3	0	1/2	2	9949.1867	1.5	9893.0409	0.0
1	3/2	2	0	1/2	2	9960.7121	−0.1	9906.6172	0.0
1	3/2	0	0	1/2	1	9990.1631	1.4	9934.0030	−0.0
1	3/2	1	0	1/2	1	10145.3776	−0.3		
2	3/2	3	1	1/2	2	19695.5304	0.5	19587.6184	−0.1
2	5/2	2	1	3/2	2	19741.3556	0.5	19630.9493	0.2
2	3/2	2	1	1/2	1	19744.5411	1.5		
2	5/2	3	1	3/2	2	19836.5686	−0.2	19725.6566	0.2
2	5/2	3	1	3/2	3	19848.0947	−1.0		
2	5/2	4	1	3/2	3	19851.5795	−2.0	19740.8692	−0.3
2	5/2	2	1	3/2	1	19927.8289	0.6		

Table 6.3: Measured frequencies of $J = 1 - 0$ and $J = 2 - 1$ transitions of $Al^{79}Br$ in $v = 0$ and $v = 1$ vibrational states.

Transition						$v = 0$	Obs. - calc.	$v = 1$	Obs. - calc.
J'	F_1'	F'	J''	F_1''	F''	/MHz	/kHz	/MHz	/kHz
1	1/2	3	0	3/2	4	9498.8843	-0.4	9447.2081	0.6
					2				
1	1/2	3	0	3/2	3	9498.8913	0.5	9447.2129	-0.8
1	1/2	2	0	3/2	1	9499.3000	0.8		
					2				
					3				
1	5/2	4	0	3/2	4	9513.1626	-0.7	9461.7707	0.3
1	5/2	4	0	3/2	3	9513.1697	0.2	9461.7765	-0.2
1	5/2	3	0	3/2	4	9514.6912	-1.2	9463.2601	0.6
					2				
					3				
1	5/2	2	0	3/2	1	9515.8005	-0.6		
1	5/2	2	0	3/2	2	9515.8088	0.9		
					3				
1	5/2	5	0	3/2	4	9516.9414	-0.4	9465.5128	-0.3
1	5/2	1	0	3/2	1	9517.4427	-0.5		
					2				
1	5/2	0	0	3/2	1	9519.4344	1.1		
1	3/2	1	0	3/2	1	9532.6899	1.0		
					2				
1	3/2	4	0	3/2	4	9534.4667	-0.1	9483.4006	-0.0
1	3/2	4	0	3/2	3	9534.4734	0.4	9483.4068	-0.1
1	3/2	2	0	3/2	1	9536.1761	-0.8		
1	3/2	2	0	3/2	2	9536.1870	0.8		
					3				
1	3/2	3	0	3/2	2	9537.7080	-0.9	9486.6262	-0.0
					3				
					4				
2	3/2	4	1	3/2	4	19023.5363	0.0		
2	5/2	4	1	3/2	3	19033.9816	-0.1	18931.2710	0.2
2	7/2	4	1	5/2	3	19035.4116	0.5	18932.7194	0.0
2	7/2	3	1	5/2	2	19035.9549	-0.4		
2	7/2	5	1	5/2	4	19037.1585	-0.1	18934.4273	-0.9
2	7/2	6	1	5/2	5	19037.7460	0.4	18935.0157	-0.2
2	5/2	5	1	3/2	4	19038.7946	0.6	18936.0618	0.8
2	1/2	3	1	1/2	2	19038.9670	-1.2		
2	1/2	2	1	1/2	3	19039.1645	0.1		
2	1/2	3	1	1/2	3	19039.3799	-0.3		
2	3/2	2	1	1/2	2	19058.8521	-0.1		
2	3/2	4	1	1/2	3	19059.1193	0.9		
2	3/2	3	1	1/2	2	19059.2005	-0.4		

Table 6.4: Measured frequencies of $J = 1 - 0$ and $J = 2 - 1$ transitions of $Al^{81}Br$ in $v = 0$ and $v = 1$ vibrational states.

Transition						$v = 0$	Obs. - calc.	$v = 1$	Obs. - calc.
J'	F_1'	F'	J''	F_1''	F''	/MHz	/kHz	/MHz	/kHz
1	1/2	3	0	3/2	4	9442.1516	-0.2	9391.0201	-0.3
					2				
1	1/2	3	0	3/2	3	9442.1572	0.3	9391.0257	0.1
1	1/2	2	0	3/2	1	9442.6367	-0.3		
					2				
					3				
1	5/2	4	0	3/2	4	9453.9378	0.0	9403.0418	0.3
					3				
1	5/2	3	0	3/2	4	9455.6860	-0.4	9404.7448	0.1
					2				
					3				
1	5/2	2	0	3/2	1	9456.6388	-0.7		
1	5/2	2	0	3/2	2	9456.6464	1.2		
					3				
1	5/2	5	0	3/2	4	9457.7853	-0.3	9406.8512	-0.1
1	5/2	1	0	3/2	1	9458.1142	-0.7		
					2				
1	5/2	0	0	3/2	1	9460.2789	0.7		
1	3/2	1	0	3/2	1	9470.4626	0.8		
					2				
1	3/2	4	0	3/2	4	9472.1403	-0.1	9421.5076	0.3
1	3/2	4	0	3/2	3	9472.1459	0.3	9421.5121	-0.5
1	3/2	2	0	3/2	1	9473.8751	-1.1		
1	3/2	2	0	3/2	2	9473.8851	1.1		
					3				
1	3/2	3	0	3/2	4	9475.3213	-0.4	9424.6748	0.1
					2				
					3				
2	3/2	4	1	3/2	4	18906.3863	-0.2		
2	5/2	4	1	3/2	3	18914.7191	0.3	18812.9761	0.0
2	7/2	4	1	5/2	3	18915.9108	0.0	18814.1951	0.2
2	7/2	3	1	5/2	2	18916.5822	-0.1		
2	7/2	5	1	5/2	4	18917.8648	0.0	18816.1040	-0.6
2	7/2	6	1	5/2	5	18918.4175	-0.1	18816.6581	-0.6
2	5/2	5	1	3/2	4	18919.4318	0.5	18817.6710	1.0
2	1/2	2	1	1/2	3	18919.6381	0.4		
2	1/2	3	1	1/2	3	18919.8830	-0.0		
2	3/2	2	1	1/2	2	18936.0620	-0.7		
2	3/2	4	1	1/2	3	18936.3751	-0.0		

Table 6.5: Molecular constants calculated for MgBr in MHz[a].

Parameter	$^{24}Mg^{79}Br$		$^{24}Mg^{81}Br$	
	$v = 0$	$v = 1$	$v = 0$	$v = 1$
B	4972.20127(57)	4944.62754(69)	4943.62546(57)	4916.28928(68)
D	0.003945(82)	0.00392(11)	0.003849(80)	0.00390(10)
γ	178.3048(14)	175.7104(19)	177.2819(13)	174.7111(17)
C_I(Br)	0.00553(39)	0.00545(50)	0.00595(39)	0.00555(48)
b_F	172.3208(12)	171.1527(41)	185.7580(12)	184.5000(41)
c	207.0793(26)	208.1257(46)	223.2175(24)	224.3390(44)
eQq(Br)	110.3133(36)	112.1877(59)	92.1532(35)	93.7125(60)

[a] One standard deviation in parentheses, in units of least significant digit.

Table 6.6: Molecular constants calculated for AlBr in MHz[a].

Parameter	$Al^{79}Br$		$Al^{81}Br$	
	$v = 0$	$v = 1$	$v = 0$	$v = 1$
B	4759.72699(17)	4734.05280(24)	4729.82499(18)	4704.39229(26)
D	0.003414(25)	0.003382(37)	0.003360(26)	0.003319(41)
eQq(Al)	−28.0059(34)	−27.8019(51)	−28.0061(35)	−27.8068(53)
eQq(Br)	78.7064(14)	80.1322(23)	65.7476(15)	66.9379(24)
C_I(Al)	0.00412(12)	0.00450(27)	0.00406(12)	0.00408(27)
C_I(Br)	0.01356(13)	0.01348(22)	0.01451(13)	0.01463(24)
α_{Al-Br}	−0.00191(33)	−0.00191[b]	−0.00170(35)	−0.00170[b]

[a] One standard deviation in parentheses, in units of least significant digit.
[b] Nuclear spin-spin constant held fixed at value obtained from $v = 0$ fit.

Table 6.7: Calculated ratios of hyperfine parameters compared to nuclear and molecular properties of MgBr and AlBr.

MgBr	v=0	v=1	Eq.[a]	Lit.
$\gamma(^{79}Br)/\gamma(^{81}Br)$	1.00577(1)	1.00572(1)	1.00579(1)	1.0057885(1)[b]
$b_F(^{79}\mathrm{Br})/b_F(^{81}\mathrm{Br})$	0.92766(1)	0.92766(3)	0.92767(2)	0.927700(2)[c]
$c(^{79}\mathrm{Br})/c(^{81}\mathrm{Br})$	0.92770(2)	0.92773(3)	0.92769(2)	0.927700(2)[c]
$eQq(^{79}\mathrm{Br})/eQq(^{81}\mathrm{Br})$	1.19706(6)	1.19715(10)	1.19702(7)	1.19707(3)[d]
$C_I(^{79}\mathrm{Br})/C_I(^{81}\mathrm{Br})$	0.929(89)	0.982(124)	-	0.933573(2)[e]

AlBr	v=0	v=1	Eq.[a]	Lit.
$eQq(^{79}\mathrm{Br})/eQq(^{81}\mathrm{Br})$	1.19710(6)	1.19711(6)	1.19711(5)	1.19707(3)[d]
$C_I(^{79}\mathrm{Br})/C_I(^{81}\mathrm{Br})$	0.934(12)	0.921(21)	-	0.933573(2)[f]

[a] For method of calculation, see text Sec. 6.4.
[b] Inverse ratio of reduced masses of $^{24}Mg^{79}Br$ and $^{24}Mg^{81}Br$, calculated using atomic masses in Ref. 120.
[c] Ratio of nuclear moments of ^{79}Br and ^{81}Br, calculated using values in Ref. 120.
[d] Ratio of electric quadrupole moments of ^{79}Br and ^{81}Br, taken from Ref. 2.
[e] Ratio of nuclear magnetic moments of ^{79}Br and ^{81}Br multiplied by inverse ratio of reduced masses of $Mg^{79}Br$ and $Mg^{81}Br$, calculated using values in Ref. 120.
[f] Ratio of nuclear magnetic moments of ^{79}Br and ^{81}Br multiplied by inverse ratio of reduced masses of $Al^{79}Br$ and $Al^{81}Br$, calculated using values in Ref. 120.

Table 6.8: Equilibrium parameters calculated for MgBr[a,b].

Method I	$^{24}Mg^{79}Br$	$^{24}Mg^{81}Br$
B_e/MHz	4985.9881(7)	4957.2936(7)
α_e/MHz	27.57373(89)	27.33618(89)
r_e/Å	2.347408(1)	2.347408(1)
Method II	$^{24}Mg^{79}Br$	$^{24}Mg^{81}Br$
B_e/MHz	4985.9675(7)	4957.2731(7)
α_e/MHz	27.51869(89)	27.28162(89)
r_e/Å	2.347413(1)	2.347413(1)
Method III	$^{24}Mg^{79}Br$	$^{24}Mg^{81}Br$
B_e/MHz	4985.9675(7)	4957.2731(7)
α_e/MHz	27.51869(89)	27.28162(89)
r_e/Å	2.347432(1)	2.347432(1)

[a] For methods of calculation, see Sec. 6.5.1.
[b] Estimated uncertainties in parentheses, in units of least significant digit, derived from rotational constants, fundamental constants and reduced masses.

Table 6.9: Comparison of equilibrium bond length estimates for AlBr[a].

	Method I[b]	Method II[b]	Method III[b]	Lit. Exp.
r_e/Å	2.294870(1)	2.294878(1)	2.294893(1)	2.29480(3)[c]

[a] For description of methods see Sec. 6.5.1.
[b] Estimated uncertainties in parentheses, in units of least significant digit, derived from rotational constants, fundamental constants and reduced masses.
[c] r_e from Wyse and Gordy [97].

Table 6.10: Summary of equilibrium bond length estimates for MgBr[a].

	Method I[b]	Method II[b]	Method III[b]	Ave.	Lit. Exp.	Lit. Theo.
r_e/Å	2.347408(4)	2.347413(4)	2.347432(4)	2.34742(2)[c]	2.36[d]	2.40[e]

[a] For description of methods see Sec. 6.5.1.
[b] Estimated uncertainties in parentheses, in units of least significant digit, derived from rotational constants, fundamental constants and reduced masses.
[c] Average of Method II and III. Uncertainty estimated from range of values.
[d] r_0 from partial rotational analysis [92].
[e] r_e from Ref. 90.

Table 6.11: Spin densities calculated from magnetic hyperfine constants for MgBr and CaBr.

Parameter	$^{24}Mg^{79}Br$	$^{40}Ca^{79}Br^{a}$	^{79}Br atom^{b}
b_F/MHz	172.321	121.202	-
c/MHz	207.079	77.620	-
$\|\Psi(0)\|^2/\text{au}^{-3}$	0.153345	0.107855	28.56
$\langle(3\cos^2\Theta - 1)/r^3\rangle/\text{au}^{-3}$	1.02919	0.385774	12.20
$\rho(s)/\%$	0.5369	0.3776	-
$\rho(p)/\%$	8.436	3.162	-

[a] Taken from Ref. 118.
[b] Calculated from data in Ref. 22.

Table 6.12: Comparison of AlBr, MgBr and related metal monobromide nuclear quadrupole coupling constants.

	$^{23}Na^{79}Br^{a}$	$^{39}K^{79}Br^{b}$	$^{24}Mg^{79}Br$	$^{40}Ca^{79}Br^{c}$	$^{27}Al^{79}Br$	$^{69}Ga^{79}Br^{d}$
$eQq(^{79}Br)$/MHz	58.60801	10.2383	110.313	20.015	78.706	106.2
i_c/%	92.5	98.7	85.7	97.4	89.8	86.2
$x_M{}^{e}$	0.9	0.8	1.2	1.0	1.5	1.5
x_M(calc.)^{f}					1.3	1.4

[a] Results taken from Ref. 124.
[b] Results taken from Ref. 125.
[c] Results taken from Ref. 118.
[d] Results taken from Ref. 122.
[e] Electronegativities taken from Ref. 2.
[f] Average of electronegativites calculated from ionic character of the respective MCl and MBr species. Uncertainty is estimated to be in the least significant digit. See Sec. 6.5.3 for method.

Chapter 7

Microwave Spectroscopy of MgNC and AlNC

7.1 Introduction

The spectra of refractory-element molecules in circumstellar clouds provide information which will further our understanding of the chemistry of these elements in space [6]. Laboratory spectra provide search parameters for new species and can be used to identify (and verify) lines in the spectra of interstellar sources. Theoretical studies have predicted that magnesium-bearing compounds should be present in circumstellar shells; however, searches for MgS, MgH and MgO have so far proved unsuccessful [73, 126, 127] and consequently other Mg-species have been suggested. A study of interstellar refractory-element chemistry by Turner suggested nitrogen containing species, such as MgN, could have a greater abundance than either sulfide or oxide species [67]. This prediction was supported by the discovery of MgNC, the first magnesium-bearing molecule found in space [68,69]. The detection of this and NaCN [128] in the circumstellar envelope of IRC + 10216 has raised the possibility that other metal cyanides and isocyanides might be present in interstellar sources. Specifically, AlNC/AlCN has been suggested [129]. This seems promising because Al and Mg have comparable cosmic abundances, and AlCl [130] and AlF [130,131] have also been detected in IRC + 10216.

The first astronomical observation of MgNC was made by Guélin *et al.* in 1986 [68].

They reported the measurement of three millimetre wave transitions of a then unknown paramagnetic molecule in IRC + 10216. In 1993, these lines were identified by Kawaguchi *et al.* [69] from the results of a laboratory based millimetre wave study. These results were extended by Anderson and Ziurys to include the other magnesium isotopomers, ^{25}MgNC and ^{26}MgNC [132], which were subsequently also identified in space [133]. The rotational spectrum in the ν_2 excited bending state has been measured and these results have been used to discuss the flexibility of the molecule [134]. The electronic spectroscopy has also been investigated [135, 136]. The first theoretical study was done in 1985 by Bauschlicher *et al.* as part of a larger study of the alkaline earth isocyanides [137]. There have been four *ab initio* studies done to predict the spectroscopic constants and structural parameters of MgNC and several related isocyanides [138–141]. Theoretical studies have also been made of the thermochemistry of MgNC and of its protonated and hydrogenated derivatives [142, 143]. Recently two low frequency transitions, $N = 3 - 2$ and $N = 4 - 3$, have been measured as part of a larger survey of IRC + 10216 [144]; however, the $N = 3 - 2$ transition was overlapped by lines due to other molecules and the hyperfine splitting was not examined. There have been no measurements of low N transitions of MgNC where the hyperfine structure due to ^{14}N has been resolved. The current work was undertaken to measure this hyperfine structure.

AlNC and AlCN were first detected by mass spectroscopy by Gingerich in 1967 [145]. Subsequently, three *ab initio* studies have been made of the structures of these molecules [129, 140, 146]. These studies predict that AlNC and AlCN should be linear, and that AlNC should be more stable than AlCN by about ~ 23 kJ/mol. Two experimental studies have been reported quite recently. Robinson *et al.* have measured the millimetre wave spectrum of AlNC in both the ground vibrational state and excited states of the bending mode, ν_2 [147]. Fukushima has reported investigation of the $^1A' - \tilde{X}\ ^1\Sigma^+$ electronic

transition of AlNC and AlCN by laser induced fluorescence [148].

This chapter reports the first measurements made of the hyperfine structure in magnesium and aluminium isocyanide. The two lowest rotational transitions of both molecules in their ground vibrational states have been measured. Hyperfine structure due to the ^{14}N nucleus has been observed in the spectra of both molecules along with nuclear hyperfine splitting due to the ^{27}Al nucleus in AlNC. The derived constants have been used to investigate orbital hybridisation in these species.

7.2 Experimental Details

MgNC and AlNC were prepared by reacting ablated Mg metal (rod from A. D. MacKay 99.9%) or ablated Al metal (rod from Goodfellow 99.999%) with cyanogen present as 0.2-0.5% in Ar backing gas. To measure the transition frequencies of the paramagnetic species MgNC, a set of three mutually perpendicular Helmholtz coils was used to collapse the Zeeman splitting due to the earth's magnetic field. This procedure was described in detail in Sec. 3.8. The signals for AlNC were so strong that the $J = 1 - 0$ transitions were easily observable in a few measurement cycles; 10 averaging cycles produced a power spectrum with 50:1 S/N.

7.3 Observed Spectra

7.3.1 MgNC

The millimetre wave spectrum of the free radical MgNC had been measured previously [69] and hence the rotational, centrifugal distortion and fine structure constants were all well determined. These results narrowed the search range for the microwave study because only the hyperfine parameters had to be estimated for the initial prediction. The magnetic hyperfine coupling constants, b_F and c, were estimated by scaling the

results from MgF [78] by the ratio of the nuclear g-factors, $g_I(^{14}\mathrm{N})/g_I(^{19}\mathrm{F})$. The nuclear quadrupole coupling constant $eQq_0(^{14}\mathrm{N})$ was assumed to be equal to that of CaNC [57].

Only the two lowest N rotational transitions, $N = 1 - 0$ and $N = 2 - 1$, were available in the frequency range of the spectrometer. An initial prediction was made for the $N = 1 - 0$ transition from the millimetre wave parameters and the estimated hyperfine parameters. The most intense component was found 400 kHz from the predicted frequency. After further searching, five components of the $N = 1 - 0$ transition were found. These lines were fit to B_0, γ and the three hyperfine parameters, with D_0 held fixed at the value obtained from the millimetre wave study [69]. These improved parameters were used to predict the $N = 2 - 1$ transitions. In total, 12 hyperfine components of the two transitions were measured; their frequencies are listed in Table 7.1. Transitions for the minor isotopomers of MgNC were not sought. An example spectrum is shown in Fig. 7.1.

7.3.2 AlNC

When this study was undertaken no experimental results had been presented, so the transition frequencies were predicted using results from the theoretical study by Ma *et al.* [129]. Experience with the similar species MgNC provided some added insight into how the theoretical results could be employed. For MgNC, it was found that calculations made at the SDCI/TZ2P level of theory produced a rotational constant B that was about 27 MHz lower in frequency than that obtained from experiment [138]. In their theoretical study of AlNC, Ma *et al.* found that B_0 and B_e differed by only about 5 MHz. Consequently the B_e constant predicted for AlNC using the same level of theory as for MgNC was chosen to calculate the initial search range. To estimate the magnitude of the hyperfine splitting, $eQq(^{27}\mathrm{Al})$ from AlF [96] and $eQq(^{14}\mathrm{N})$ from MgNC were included in

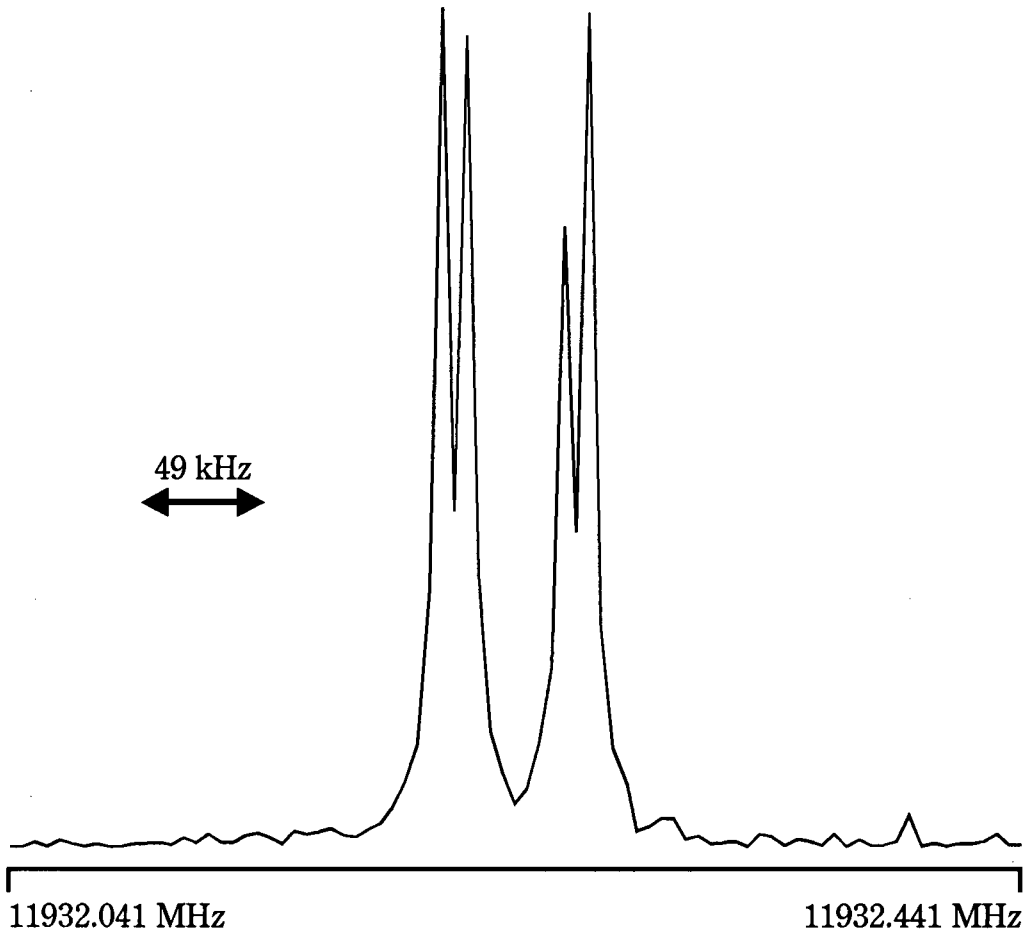

Figure 7.1: The $N = 1 - 0$, $J = 3/2 - 1/2$, $F = 3/2 - 1/2$ transition of $^{24}Mg^{14}N^{12}C$ was measured using a set of mutually perpendicular Helmholtz coils to remove the effects of the earth's magnetic field. In addition to the 49 kHz Doppler splitting, a residual Zeeman splitting, on the order of 10 kHz, is present in this spectrum. This spectrum was obtained with 400 averaging cycles. The microwave excitation frequency was 11932.241 MHz. 4 K data points were measured with a 50 ns sampling interval and the power spectrum is displayed as an 4 K transformation.

the prediction. The $J = 1-0$ transitions were found less than 40 MHz from the predicted values.

Two rotational transitions, $J = 1 - 0$ and $J = 2 - 1$, were available in the frequency range of the spectrometer. Twenty seven lines were measured for the main isotopomer $^{27}Al^{14}N^{12}C$ (98.53% natural abundance). Spectra of species containing other isotopes of N and C were not sought. Nuclear hyperfine structure due to both ^{27}Al ($I = \frac{5}{2}$) and ^{14}N ($I = 1$) was observed. Since the splittings due to ^{27}Al were larger than those due to ^{14}N, the lines were easily assigned in terms of the coupling scheme $\mathbf{J} + \mathbf{I}_{Al} = \mathbf{F_1}; \mathbf{F_1} + \mathbf{I}_N = \mathbf{F}$. An overview spectrum of the $J = 1 - 0$ transition, shown in Fig. 7.2, shows the relative magnitudes of these splittings: the ^{27}Al quadrupole coupling produces three lines which are then split further by the ^{14}N quadrupole coupling. An expanded view of the $F_1 = 7/2 - 5/2$ section of the $J = 1 - 0$ transition is given in Fig. 7.3. All the measured lines and their assignments are listed in Table 7.2.

7.4 Analyses

7.4.1 MgNC

The measured transition frequencies of MgNC were fit using Pickett's exact fitting program SPFIT [76], which employs a Hund's case ($b_{\beta J}$) coupling scheme, $\mathbf{N} + \mathbf{S} = \mathbf{J}$; $\mathbf{J} + \mathbf{I}_N = \mathbf{F}$. This fit determined the rotational and centrifugal distortion constants, B_0 and D_0, the spin-rotation parameter, γ, the nuclear quadrupole coupling constant, $eQq_0(^{14}N)$, and the magnetic hyperfine parameters, the Fermi contact constant, b_F, and the dipole-dipole coupling constant, c. The parameters are listed in Table 7.3 under the heading Microwave Fit, along with the millimetre wave parameters obtained by Kawaguchi *et al.* [69]. The rotational and centrifugal distortion constants obtained agree well with those of the millimetre wave study, within three standard deviations. However,

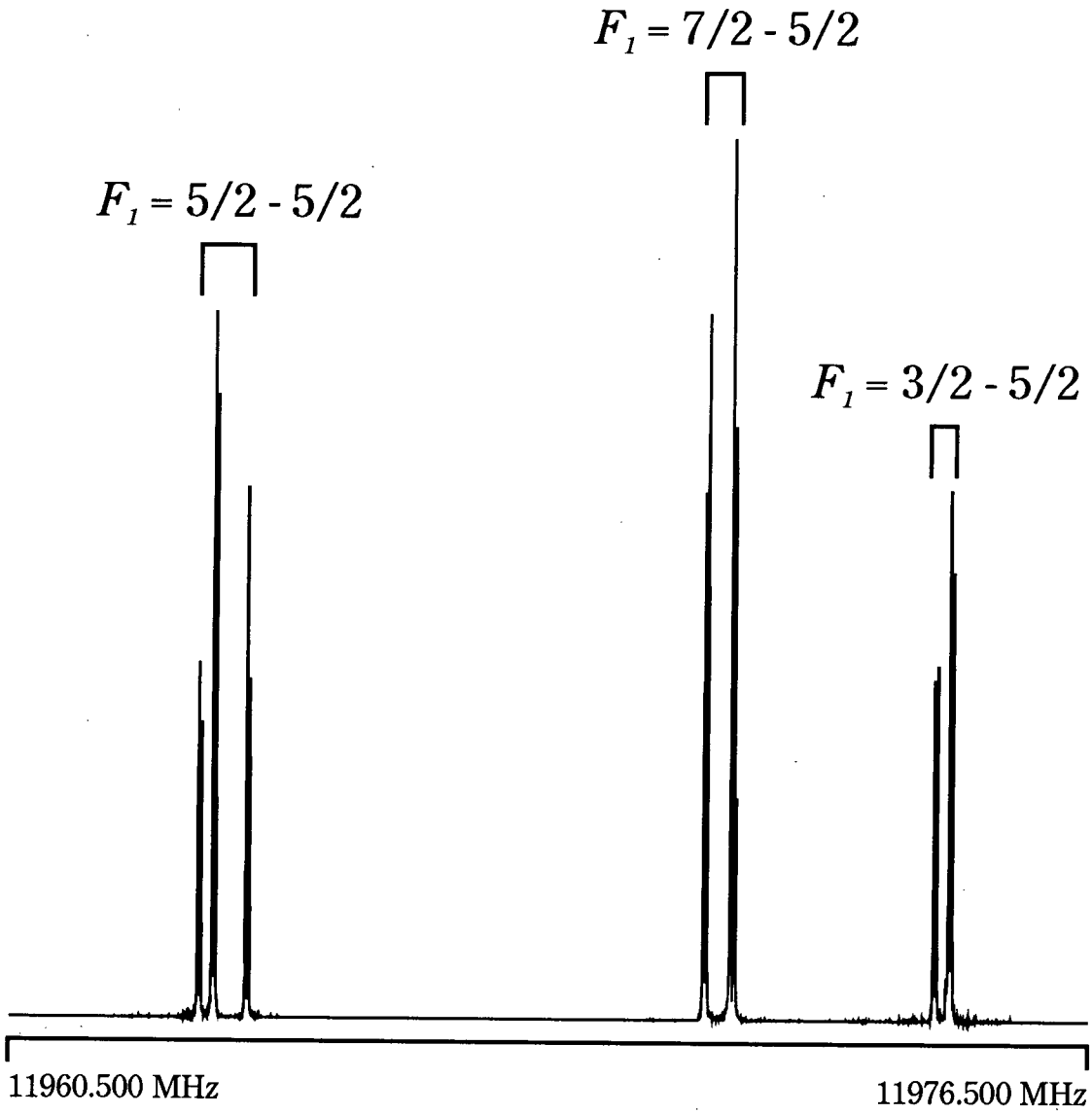

Figure 7.2: Composite spectrum of the $J = 1 - 0$ rotational transition of AlNC. The results of three different microwave experiments were used to produce this composite. Each experiment consisted of 200 averaging cycles. 4 K data points were collected at 50 ns sampling interval and transformed.

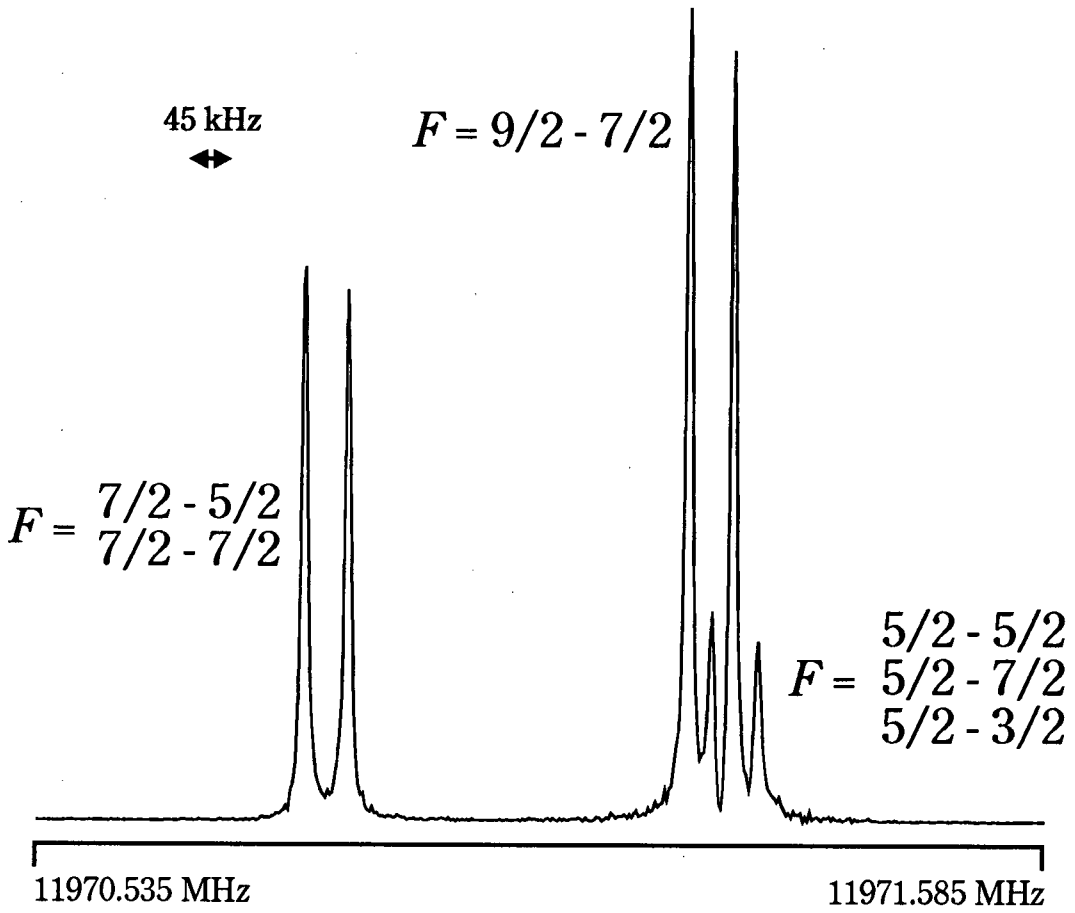

Figure 7.3: Detail of the $J = 1 - 0$ transition of AlNC, showing the $F_1 = 7/2 - 5/2$ hyperfine transition. This spectrum was obtained with 75 averaging cycles. 4 K data points were measured and the power spectrum is displayed with an 8 K transformation. The microwave excitation frequency was 11970.835 MHz.

the spin-rotation parameter γ does not compare as well. This is most likely the result of spin-rotation distortion effects, which were potentially significant in the higher N transitions measured at the millimetre wave lengths, but not in the lowest N transitions measured in our study.

To confirm this deduction, a global fit was made using both the microwave and millimetre wave data. The transitions used are listed in Table 7.1. The data were fit simultaneously, using all lines to determine the rotational and quartic and sextic centrifugal distortion constants, B_0, D_0, and H_0, the spin-rotation constants, γ and γ_D, and the hyperfine parameters. In this fit, the microwave data were given a relative weighting of 100:1 with respect to the millimetre wave results to account for the measurement uncertainties. The parameters determined are listed in Table 7.3 under the heading Global Fit. The rotational and centrifugal distortion parameters agree well with those obtained from the millimetre wave study [69], to within three standard deviations. Distortion effects do appear to be the source of the discrepancy between the spin-rotation constants determined in the microwave and millimetre wave studies. In the Global Fit, the spin-rotation distortion parameter, γ_D, was determined to better than 1 part in 10, which was not possible from the millimetre wave data alone. By fitting these results together with the microwave data, this constant could be determined.

7.4.2 AlNC

The measured frequencies of AlNC were fit using Pickett's program SPFIT [76], to the rotational constant B_0, the centrifugal distortion constant D_0, the nuclear quadrupole and nuclear spin rotation coupling constants, eQq and C_I, for both the Al and N nuclei, and the nuclear spin-spin constant, α_{Al-N}. The lines observed for the overlapped hyperfine components of the $J = 1-0$ transition were fit as blended lines using predicted intensities

as weighting factors. The resulting constants are listed in Table 7.4.

Table 7.4 also compares the present results with those of Robinson *et al.* [147]. The rotational and centrifugal distortion constants agree quite well, within one standard deviation. Our high resolution FTMW study produced a more precise B_0. However the value of D_0 derived from the millimetre wave study was more precise because rotational transitions up to $J = 31$ were measured, where distortion effects are larger. It is interesting that in the present work a value of D_0 precise to three figures could be obtained. This too reflects the high precision of FTMW spectroscopy. To parallel the approach taken for MgNC, a fit of the FTMW and millimetre wave results for AlNC was made. The resulting constants are listed in Table 7.4 under the heading Global Fit. The measurement uncertainties were used to obtain a relative weighting of 400:1 for the microwave lines with respect to the millimetre wave data. The rotational and centrifugal distortion constants obtained from the global fit compare well with those obtained from the millimetre wave study [147].

The B_0 rotational constant also compares fairly well with the theoretical values of Ma *et al.* [129] as shown in Table 7.5. It appears that the TZ2P + f CISD level of calculations provided the best estimate of the rotational constant, to within 17 MHz of the experimental result. The predicted B_e labelled by Ma *et al.* as the most reliable, however, proved to be about 100 MHz lower in frequency. The assumed quadrupole coupling constants, derived from AlF and MgNC, were found to provide excellent estimates of those of AlNC, thereby showing the similarities between these three molecules.

7.5 Discussion

The three possible equilibrium structures for metal cyanide compounds are the linear cyanide, the linear isocyanide, and the non-linear T-shaped configurations. The structures observed have been described as resulting from a subtle balance between long-range (classical electrostatic and induction) and short-range (exchange and penetration) forces [149]. This picture was proposed by Essers *et al.* to explain the structures of the alkali metal cyanides(K, Na and Li). The almost completely ionic compounds KCN and NaCN are both T-shaped because the short-range interaction predominates, while the slightly less ionic LiNC has the linear isocyanide structure. This structure was described as a compromise between the T-shaped configuration, favoured by the short-range interaction, and the linear cyanide structure, favoured by the long-range interaction [149]. This linear isocyanide structure was also predicted to be favoured for aluminium monocyanide [129,147] and the alkaline earth monocyanides [57,137,150,151].

When considering the experimental results for AlNC and MgNC, comparisons can be made with two types of compounds; namely the linear metal isocyanides and the metal monohalides. The linear isocyanide structure is preferred for lithium [152] and the alkaline earth [137] as well as aluminium [129] cyanides. It has been observed that the ionic character of the M-NC bond decreases as the calculated energy difference between the linear isocyanide and cyanide structures of these molecules increases [129]. Since AlNC has the greatest calculated energy difference of the linear metal isocyanides, the Al-NC bond should be less ionic than that of MgNC and the other alkaline earth and alkali metal isocyanides. Also the properties of the magnesium and aluminium isocyanides should be comparable to those of the magnesium and aluminium monohalides, since the electronegativity of the CN group is similar to those of F and Cl. Information obtained from the hyperfine constants can be used to determine whether AlNC and MgNC follow

these predicted bonding trends.

7.5.1 Nuclear Quadrupole Coupling Constants

The bonding in the metal cyanides and isocyanides can be investigated through their nuclear quadrupole coupling constants. Table 7.6 lists the ^{14}N quadrupole coupling constants for several of these species. For NaCN and KCN, the eQq_z constant is listed. This allows comparisons to be made to constants obtained for the linear isocyanides because the z-axis in the T-shaped KCN and NaCN compounds was found to be almost parallel to the CN bond [153, 154]. Also listed in Table 7.6 is the nuclear quadrupole coupling constant determined for the nearly completely covalent molecule HNC [155]. The constants for NaCN and KCN are in close agreement with that calculated for the free CN^- ion [154], showing that these are indeed almost completely ionic compounds. It can be seen, by comparison with KCN, NaCN and HNC, that the linear metal isocyanides are fairly ionic species. However, they do appear to have some covalent character. To investigate further the bonding in these species, the degree of sp-hybridisation of the ^{14}N atom was calculated from the nuclear quadrupole coupling constants.

The ^{14}N nuclear quadrupole coupling constants can be interpreted in terms of valence p-shell electrons using the Townes-Dailey model [17], which was described in detail in Sec. 2.3.1. Eq. (2.43) relates the measured molecular quadrupole coupling constant to the nuclear quadrupole coupling constant of an np-electron. This expression is repeated here for reference:

$$eQq(\text{mol}) = \left(n_z - \frac{n_x + n_y}{2}\right) eQq_{n10}(\text{atom})$$

where n_x, n_y and n_z are the number of electrons in the np_x, np_y and np_z orbitals, respectively. By estimating values for n_x, n_y and n_z, this model can be used to probe orbital hybridisation [2, 35, 93]. The molecular orbital basis for this discussion can be

found in Sec. 2.5.

We will consider an sp_z-hybrid orbital on N in a linear metal isocyanide molecule; d orbital contributions will be neglected. In this discussion of linear molecules, the z-axis will be taken to be the molecular axis. The number of p_z-electrons in the two hybrid orbitals can be calculated from Eq. (2.75)

$$n_z = 2a^2(1 - a_s^2) + Na_s^2$$

where the first term is from the sp-hybrid bonding orbital and the second from the counterhybridised orbital, which may or may not be involved in another bond. In this expression, a^2 is the fractional weight of the sp hybrid in the M-N bond molecular orbital, a_s^2 is the s-character of the hybrid orbital and N is the number of electrons in the counterhybridised orbital. The a^2 value can be estimated from the ionic character of the molecule, i_c, using Eq. (2.67). Methods of calculating ionic character are discussed in Sec. 2.5. For all species discussed here, i_c has been calculated using the approximate expression Eq. (2.77):

$$i_c = \frac{|x_M - x_{NC}|}{2}$$

The electronegativity values, x, are taken from Ref. [2], except for x_{Al}; for it the value derived from the nuclear quadrupole coupling constants of AlBr and AlCl in Chapter 6 was used. (The calculated a_s^2 values changed by only 5% when using the more exact expression, Eq. (2.78), for i_c.)

In a linear metal isocyanide compound, M-NC, the N is on the negative pole of the bond and therefore $2a^2$ is equal to $(1 + i_c)$. Care must be taken in determining the p-electron distribution because N is part of the NC ligand. The sp-hybrid orbital forms the M-N bond and the counterhybridised orbital forms the N-C σ bond. The bonding in the N≡C group is assumed to be completely covalent, so each of the pure $2p_x$ and $2p_y$ orbitals

and the *sp* counterhybridised orbital have one half of a bond pair ($n_x = n_y = N = 1$). Using Eq. (2.43) and (2.75) and substituting the above values, the following equation results

$$\begin{aligned} eQq(^{14}\mathrm{N}) &= \left[(1+i_c)(1-a_s^2)+a_s^2-\frac{1+1}{2}\right] eQq_{210}(^{14}\mathrm{N}) \\ &= i_c(1-a_s^2)eQq_{210}(^{14}\mathrm{N}). \end{aligned} \tag{7.1}$$

A further correction must be added to account for the screening effect of the negative charge on the NC group,

$$eQq(^{14}\mathrm{N}) = i_c(1-a_s^2)\frac{eQq_{210}(^{14}\mathrm{N})}{(1+i_c\varepsilon)}, \tag{7.2}$$

where $\varepsilon = 0.3$ [1]. The value of a_s^2 was calculated for the bonding orbital of N for MgNC, AlNC and several other linear isocyanides using Eq. (7.2); the results are listed in Table 7.6. Since *s*-character values for the various linear isocyanides are approximately equal (within $\sim 10\%$), the bonding orbital in each of the isocyanide groups must be similar. The differences in the observed nuclear quadrupole coupling constants appear to arise solely from differences in the ionic character of the M-NC bond, which decreases from LiNC to AlNC. As the M-NC bond becomes more ionic, more electron density is transferred from the metal atom to the N, thereby increasing the magnitude of the quadrupole coupling constant, as predicted by Eq. (7.1). The nuclear quadrupole coupling constants are listed in the table in order of decreasing ionic character of the M-NC bond, so the effects of charge transfer, from the metal atom to the cyanide ligand, on the field gradient at the nitrogen nucleus can be seen in the decreasing quadrupole coupling constants.

In the case of AlNC, there is a significant contribution to the coupling constants from orbital hybridisation on both Al and N nuclei. The *sp*-hybridisation of the Al bonding orbital can be investigated using a method similar to that described above for N. In this discussion several Al-X compounds will be considered.

The valence shell configuration of Al is $3s^2 3p^1$. The value of $2a^2$ is $(1 - i_c)$, since Al is the positive pole of the Al-X bond [2]. N will be taken to be 2, because the counterhybridised orbital will have an unshared pair, and the $3p_x$ and $3p_y$ orbitals are unfilled, so $n_x = n_y = 0$. By combining Eqs. (2.43) and (2.75) and substituting, the following expression results:

$$eQq(^{27}\mathrm{Al}) = [(1 - i_c)(1 - a_s^2) + 2a_s^2]eQq_{310}(^{27}\mathrm{Al}). \tag{7.3}$$

A further correction must be added to account for decreased nuclear screening of the positive Al nucleus,

$$eQq(^{27}\mathrm{Al}) = [(1 - i_c)(1 - a_s^2) + 2a_s^2](1 + i_c\varepsilon)eQq_{310}(^{27}\mathrm{Al}), \tag{7.4}$$

where $\varepsilon = 0.35$ for Al [1]. Eq. (7.4) was used to estimate the s-character of the sp-hybridised bonding orbital of Al for AlNC, AlF, AlCl and AlBr and the results are listed in Table 7.7. These four species are quite ionic compounds (completely so in the case of AlF) and without contributions from sp-hybridisation the Al quadrupole coupling constants would be be negligible. The s-character calculated for AlNC is intermediate between that of AlF and AlCl and the values of both $eQq(^{27}\mathrm{Al})$ and a_s^2 decrease from F to NC to Cl to Br.

7.5.2 Electron Spin-Nuclear Spin Hyperfine Parameters for MgNC

The nature of the bonding in MgNC can be examined by calculating the unpaired electron spin density in the nitrogen atomic orbitals from the electron spin-nuclear spin hyperfine coupling constants. In a completely ionic alkaline earth isocyanide compound, the unpaired electron should be centred solely on the metal ion, M^+, i.e. with no unpaired electron density at nitrogen. The unpaired electron spin densities in the nitrogen

atomic orbitals are related to the Fermi contact constant, b_F, and to the dipole-dipole interaction constant, c. Definitions of these constants were given in Eqs. (2.52) and (2.53) and discussed in detail in Sec. 2.3.3. These equations are repeated here for reference

$$\begin{aligned} b_F &= \frac{8\pi}{3} g_N g_e \mu_N \mu_B |\Psi(0)|^2 \\ c &= \frac{3}{2} g_N g_e \mu_N \mu_B \langle (3\cos^2\Theta - 1)/r^3 \rangle, \end{aligned}$$

From b_F and c, values of $|\Psi(0)|^2$ and $\langle (3\cos^2\Theta - 1)/r^{-3} \rangle$ were calculated for MgNC and CaNC. These are listed in Table 7.8. Also listed are corresponding values for the nitrogen atom which were calculated by taking the unpaired electron to be entirely on the nitrogen, in either the $2s$ orbital or the $2p_z$ orbital. Atomic parameters for the calculations were taken from Morton and Preston [22]. Unpaired electron spin densities, $\rho(s)$ and $\rho(p)$, were determined for MgNC and CaNC by taking the ratios of the respective experimental molecular to calculated atomic values. The values obtained are listed in Table 7.8. These are quite small for both species, indicating that there is very little unpaired electron spin density on the nitrogen nucleus and that these are highly ionic compounds. However, the N spin densities calculated for MgNC are more than twice those for CaNC. A similar trend has been observed for MgBr and the other alkaline earth monohalide compounds: as the mass of the alkaline earth atom decreases, the covalent character of the M-X bond increases [79]. It appears that this trend is also followed in the alkaline earth isocyanides.

The electron spin-nuclear spin hyperfine parameters for the alkaline earth isocyanides can also be compared to those of the corresponding alkaline earth fluorides. The magnetic hyperfine parameters used in the initial prediction for MgNC were calculated by scaling those of MgF by the ratio of the nuclear g-factors, $g_I(^{14}\mathrm{N})/g_I(^{19}\mathrm{F})$. This estimation method had been used for CaNC [57] and provided values which were of the right order of magnitude. However when this method was used for MgNC, the values predicted from MgF [$b_F = 16.5$ MHz and $c = 13.7$ MHz] did not agree well with the experimentally

determined values [b_F = 29.167 MHz and c = 5.386 MHz]. This suggests that the electronic structures of CaF and CaNC are more similar than those of MgF and MgNC.

7.5.3 Nuclear Spin-Spin Constant for AlNC

From the nuclear spin-spin coupling constant, an estimate of the Al-N bond distance can be made. The nuclear spin-spin constants are described in detail in Sec. 2.3.3. α_{Al-N} was defined in Eq. (2.58) as

$$\alpha_{Al-N} = \frac{-3\mu_N^2 g_{Al} g_N}{r_{Al-N}^3}.$$

A value of r_{Al-N} = 1.75(20) Å was obtained from this expression. The large uncertainty comes from the relatively large uncertainty in α_{Al-N}. This result compares well, within the uncertainty, with the experimental value determined by Robinson *et al.*(1.849 Å) [147] and the theoretical values calculated by Ma *et al.* [129]. Also this Al-N bond distance is intermediate between the corresponding distances in AlF [r_e = 1.65436 Å [94, 95]] and AlCl [r_e = 2.13011 Å [97]], parallelling the bond properties obtained from the Al quadrupole coupling constants and again showing the similarities between these three Al-X species.

7.6 Conclusion

Laser ablation has been shown to be an effective route to produce metal isocyanides for investigation by FTMW spectroscopy. This first measurement of the hyperfine structure of aluminium isocyanide and magnesium isocyanide has produced several new parameters. The nuclear quadrupole and nuclear spin-rotation constants for the N nuclei, in each molecule, have been determined along with those for the Al nuclei in AlNC. The *sp*-hybridisation in the bonding orbitals of AlNC and MgNC have been investigated through

the nuclear quadrupole coupling constants. The orbital hybridisation calculated for N in the linear metal isocyanides is quite similar. The Mg-NC bond has been found to have greater covalent character than that found in CaNC; this trend mirrors that found in the alkaline earth monohalides. The AlNC bond properties have been found to be intermediate between those of AlF and AlCl.

Table 7.1: Observed frequencies of $^{24}Mg^{14}N^{12}C$ in its ground vibrational state[a].

Transition						Obs. Freq.	$\Delta\nu$ Microwave Fit[b,c]	$\Delta\nu$ Global Fit[b,c]
N'	J'	F'	N''	J''	F''	(MHz)	(kHz)	(kHz)
1	1/2	1/2	0	1/2	3/2	11922.9251	−0.9	−0.9
1	1/2	3/2	0	1/2	1/2	11928.6450	0.5	0.7
1	3/2	3/2	0	1/2	3/2	11932.2411	0.3	0.2
1	3/2	1/2	0	1/2	1/2	11935.7735	−1.0	−0.8
1	3/2	5/2	0	1/2	3/2	11941.2144	1.1	1.1
2	3/2	5/2	1	1/2	3/2	23861.2286	2.0	2.2
2	5/2	3/2	1	3/2	3/2	23863.0750	−0.1	0.1
2	3/2	3/2	1	3/2	1/2	23863.7795	−1.4	−1.1
2	5/2	5/2	1	3/2	5/2	23864.6542	0.3	0.6
2	5/2	3/2	1	1/2	1/2	23872.3887	−1.3	−1.2
2	5/2	5/2	1	3/2	3/2	23873.6278	1.4	1.8
2	5/2	7/2	1	3/2	5/2	23875.0396	−0.9	−0.4
21	41/2		20	39/2		250445.992		4
21	43/2		20	41/2		250461.245		−7
22	43/2		21	41/2		262356.464		−18
22	45/2		21	43/2		262371.679		−60
23	47/2		22	45/2		274279.991		−40
24	47/2		23	45/2		286170.795		6
24	49/2		23	47/2		286186.023		−9
26	51/2		25	49/2		309975.563		8
26	53/2		25	51/2		309990.788		6
27	53/2		26	51/2		321874.135		10
27	55/2		26	53/2		321889.423		79
28	57/2		27	55/2		333785.266		28
29	57/2		28	55/2		345663.196		23
29	59/2		28	57/2		345678.383		9
30	59/2		29	57/2		357553.444		−23
30	61/2		29	59/2		357568.654		−6
31	61/2		30	59/2		369440.810		−11
31	63/2		30	61/2		369455.973		−31

[a] Results between 11.9-23.9 GHz are from present study. Other data taken from Ref. [69].
[b] Observed minus calculated frequencies listed as $\Delta\nu$.
[c] Results for microwave and global fits are listed in Table 7.3.

Table 7.2: Observed ground vibrational state frequencies of AlNC[a].

Transition						Obs. Freq.	$\Delta\nu$ Microwave[b,c]	$\Delta\nu$ Global[b,c]
J'	F_1'	F'	J''	F_1''	F''	(MHz)	(kHz)	(kHz)
1	5/2	1/2	0	5/2	5/2 3/2	11963.2831	−0.1	−0.0
1	5/2	7/2	0	5/2	5/2 7/2	11963.4981	−0.0	0.1
1	5/2	5/2	0	5/2	5/2 7/2 3/2	11963.9959	0.0	0.2
1	7/2	7/2	0	5/2	5/2 7/2	11970.8348	−0.1	0.0
1	7/2	9/2	0	5/2	7/2	11971.2387	−0.5	−0.3
1	7/2	5/2	0	5/2	5/2 7/2 3/2	11971.2646	0.1	0.2
1	3/2	3/2	0	5/2	5/2 3/2	11974.2358	0.1	0.1
1	3/2	1/2	0	5/2	3/2	11974.4227	0.7	0.7
1	3/2	5/2	0	5/2	5/2 7/2 3/2	11974.4597	−0.1	0.0
2	5/2	7/2	1	3/2	5/2	23930.8749	0.4	0.4
2	7/2	5/2	1	7/2	5/2	23932.3001	0.8	0.9
2	7/2	9/2	1	7/2	9/2	23932.3737	−0.5	−0.5
2	7/2	7/2	1	7/2	7/2	23932.6368	−0.0	0.0
2	3/2	5/2	1	3/2	5/2	23935.9314	−0.3	−0.3
2	3/2	3/2	1	3/2	3/2	23936.5199	−0.7	−0.7
2	9/2	9/2	1	7/2	7/2	23939.2513	0.1	0.1
2	9/2	11/2	1	7/2	9/2	23939.4034	−0.3	0.2
2	7/2	7/2	1	5/2	5/2	23939.4758	−0.1	0.1
2	9/2	7/2	1	7/2	5/2	23939.5286	0.7	0.8
2	7/2	9/2	1	5/2	7/2	23940.1152	−0.0	0.0
2	7/2	5/2	1	5/2	3/2	23940.2807	0.1	0.2
2	1/2	3/2	1	3/2	5/2	23940.5822	0.1	0.0
2	5/2	5/2	1	5/2	5/2	23941.6089	0.1	0.2
2	5/2	7/2	1	5/2	7/2	23941.8364	0.2	0.3
2	5/2	3/2	1	5/2	3/2	23941.9025	−0.4	−0.4
2	3/2	3/2 1/2	1	5/2	5/2 3/2	23946.7609	−0.1	−0.1
2	3/2	5/2	1	5/2	7/2	23946.8933	−0.1	−0.1
11			10			131642.189		−16
12			11			143605.379		−17
13			12			155567.428		−43
14			13			167528.343		3
15			14			179487.893		−18

Observed ground vibrational state frequencies of AlNC[a] (cont.).

Transition						Obs. Freq.	$\Delta\nu$ Microwave[b,c]	$\Delta\nu$ Global[b,c]
J'	F_1'	F'	J''	F_1''	F''	/MHz	(kHz)	/kHz
18			17			215357.910		−8
19			18			227311.359		−25
20			19			239263.086		−10
21			20			251212.965		−2
22			21			263160.905		−0
23			22			275106.835		12
24			23			287050.637		7
25			24			298992.248		8
26			25			310931.575		11
27			26			322868.534		19
28			27			334803.018		12
29			28			346734.944		−6
30			29			358664.263		1
31			30			370590.854		−2
32			31			382514.633		−15

[a] Results between 11.9-23.9 GHz are from present study. Other data taken from Ref. [147].
[b] Observed minus calculated frequencies listed as $\Delta\nu$.
[c] Results for microwave and global fits are listed in Table 7.4.

Table 7.3: Molecular constants calculated for $^{24}Mg^{14}N^{12}C$ in MHz[a].

Parameter	Microwave Fit[b]	Global Fit[c]	Lit.[d]
B_0	5966.90349(63)	5966.90349(19)	5966.8969(24)
D_0	0.004233(88)	0.00424336(43)	0.0042338(35)
H_0x10^7	-	0.3521(30)	0.308(16)
γ	15.3320(20)	15.3322(19)	15.219(13)
γ_Dx10^4	-	−0.518(45)	-
b_F	29.1645(79)	29.1637(77)	-
c	5.3838(82)	5.3840(77)	-
$eQq_0(^{14}N)$	−2.3232(55)	−2.3231(53)	-

[a] One standard deviation in parentheses, in units of least significant digit.
[b] Fit of microwave data only; for details see Sec 7.4.1.
[c] Fit of microwave and millimeter wave data; for details see Sec. 7.4.1.
[d] From millimeter wave study [69].

Table 7.4: Molecular constants calculated for AlNC in MHz[a].

Parameter	Microwave Fit[b]	Global Fit[c]	Lit.[d]
B_0	5984.67681(23)	5984.676685(59)	5984.6752(14)
D_0	0.003898(30)	0.00388947(34)	0.0038870(24)
H_0x10^7	-	0.2551(26)	0.243(13)
$eQq(^{27}\mathrm{Al})$	−35.6268(16)	−35.6268(16)	-
$eQq(^{14}\mathrm{N})$	−2.1508(19)	−2.1508(19)	-
$C_I(^{27}\mathrm{Al})$	0.003850(84)	0.003841(84)	-
$C_I(^{14}\mathrm{N})$	0.00156(25)	0.00155(25)	-
α_{Al-N}	−0.00127(43)	−0.00126(42)	-

[a] One standard deviation in parentheses, in units of least significant digit.
[b] Fit of microwave data only; for details see Sec 7.4.2.
[c] Fit of microwave and millimeter wave data; for details see Sec. 7.4.2.
[d] Results from millimeter wave study [147].

Table 7.5: Comparison of experimental and theoretical rotational constants for AlNC.

	B/MHz
B_0 exp.	5984.6768
B_e TZ2P + f CISD	5968[a]
B_e TZ2P + f CCSD(T)	5882[a]

[a] From Ref. [129]. B_e was calculated since it was determined that B_e and B_0 differ by less than 5 MHz.

Table 7.6: Comparison of nuclear quadrupole coupling constants of MgNC, AlNC and related cyanides and isocyanides.

Species	Structure	$eQq_0(^{14}\mathrm{N})^a$/MHz	$a_s^{2\,h}$	$i_c{}^i$
KCN	T-shaped	$-4.11^{b,c}$		
NaCN	T-shaped	$-4.219^{b,d}$		
LiNC	linear NC	-2.941^e	0.59	0.93
CaNC	linear NC	-2.697^f	0.62	0.90
MgNC	linear NC	-2.323	0.64	0.80
AlNC	linear NC	-2.151	0.65	0.75
HNC	linear NC	$+0.28^g$		

[a] Molecular properties listed in order of decreasing ionic character of M-NC bond.
[b] Using eQq_z which is along C-N axis (± 1 deg).
[c] From Ref. 153.
[d] From Ref. 154.
[e] From Ref. 152.
[f] From Ref. 57.
[g] From Ref. 155.
[h] s-character of ^{14}N bonding orbital calculated from the ^{14}N nuclear quadrupole coupling constant. For details, see Sec. 7.5.1.
[i] Ionic character of M-NC bond calculated from electronegativities using Eq. (2.77).

Table 7.7: s-character of Al bonding orbital calculated from Al nuclear quadrupole coupling constants.

Species	$eQq(^{27}\mathrm{Al})$/MHz	a_s^2
AlF	-37.49^a	0.37
AlNC	-35.627	0.29
AlCl	-30.408^b	0.26^c
AlBr	-28.006^d	0.20^c

[a] From Ref. [96].
[b] From Ref. [54].
[c] Differs from value in Ref. [2], because of the method used to calculate i_c.
[d] Result from Chapter 6.

Table 7.8: Unpaired electron spin densities calculated at the ^{14}N nucleus from magnetic hyperfine constants for MgNC and CaNC.

Parameter	MgNC	CaNC[a]	^{14}N atom[b]
b_F/MHz	29.167	12.4815	-
c/MHz	5.389	2.074	-
$\|\Psi(0)\|^2/\text{au}^{-3}$	0.0902704	0.0386299	5.606
$\langle(3\cos^2\Theta - 1)/r^3\rangle/\text{au}^{-3}$	0.093143	0.035842	2.8792
$\rho(s)/\%$	1.61	0.689	-
$\rho(p)/\%$	3.23	1.24	-

[a] Taken from Ref. 57.
[b] Calculated from data in Ref. 22; for details see Sec. 7.5.2.

Chapter 8

FTMW Spectroscopy of Yttrium Monohalides: YF and YBr

8.1 Introduction

Interest in the spectroscopy of transition metal containing diatomic molecules has been motivated by the desire to understand the role that d orbitals play in bonding [156]. The yttrium and scandium monohalides have been used as prototype systems by theoreticians because Y and Sc have the simplest open d shell configuration [(core)$nd^1(n+1)s^2$] [157]. Transition metal halides are also of interest in high temperature chemistry [158]. The chemiluminescent reactions of Sc, Y, and La atoms with halogen molecules have been investigated as part of the search for new chemical laser systems [159–161]. Over the past several years, spectroscopic studies of the electronic transitions of the yttrium and scandium monohalides have furthered our understanding of the electronic structures of these molecules. This chapter describes the FTMW spectroscopy of two of these species, YF and YBr.

The most thoroughly studied yttrium monohalide is yttrium monofluoride, whose electronic spectroscopy has been investigated in some detail. Initial studies by Barrow and co-workers [162, 163], and by Shenyavskaya and co-workers [164–167], provided rotational analyses of six singlet transitions ($B^1\Pi - X^1\Sigma^+$, $C^1\Sigma^+ - X^1\Sigma^+$, $D^1\Pi - X^1\Sigma^+$, $E^1\Pi - X^1\Sigma^+$, $F^1\Sigma - X^1\Sigma^+$, and $G^1\Pi - X^1\Sigma^+$) and one triplet transition ($d^3\Phi - a^3\Delta$).

Further studies by Kaledin and Shenyavskaya [168, 169] have improved the rotational constants available for the $X^1\Sigma^+$ and $C^1\Sigma^+$ states and have provided rotational analyses of five new transitions ($b^3\Pi - X^1\Sigma^+$, $e^3\Pi(\Omega = 1) - X^1\Sigma^+$, $^3\Pi - a^3\Delta$, $^3\Pi - b^3\Pi$, and $^3\Pi - X^1\Sigma^+$). In the most recent study by Kaledin *et al.* [170], improved molecular constants have been determined for several electronic states and ligand field theory calculations were used to propose electronic configurations for the excited electronic states of YF. Theoretical spectroscopic constants have been calculated by Langhoff *et al.* [157]. The permanent electric dipole moments of the $X^1\Sigma^+$ ground electronic state and the $B^1\Pi$ excited electronic state were determined by molecular beam optical Stark spectroscopy [171]. Pure rotational transitions of YF, in the ground electronic state, have been measured by molecular beam double resonance techniques. In the first study an effusive oven source was used to produce YF and its spectrum was measured *via* a millimetre wave optical pump/probe technique [172]. A laser ablation source coupled to a pump/probe microwave optical double resonance spectrometer was used in the second study [173]. Both studies produced rotational constants for the ground vibrational state. Even though low J rotational transitions were measured, hyperfine structure due to the ^{19}F nucleus was not reported in either study.

The spectroscopies of yttrium monochloride and monoiodide have been investigated to a lesser extent. The first study of YCl was made in 1966 by Janney [174]. More recently, rotationally resolved studies have been made of six singlet transitions ($B^1\Pi - X^1\Sigma^+$, $C^1\Sigma^+ - X^1\Sigma^+$, $D^1\Pi - X^1\Sigma^+$, $D^1\Pi - A^1\Delta$, $J^1\Pi - X^1\Sigma^+$, $K^1\Pi - X^1\Sigma^+$) [175–179]. In addition a triplet transition ($d^3\Phi - a^3\Delta$) and an intercombination band ($D^1\Pi - a^3\Delta$) have been investigated [180]. The permanent electric dipole moments in the $C^1\Sigma^+$ excited electronic state and $X^1\Sigma^+$ ground electronic state have been determined by molecular beam Stark spectroscopy [181]. The pure rotational spectrum has been measured by

Fourier transform microwave spectroscopy and the hyperfine parameters of both isotopomers of YCl have been determined [56]. Two ro-vibrational studies have been made of the spectrum of yttrium monoiodide in the infrared region by Bernard *et al.* [182,183].

Yttrium monobromide is the least studied of the yttrium monohalides. Low resolution spectra of two electronic transitions of YBr have been measured by laser induced fluorescence [175]. In this study, rotational features could not be resolved and the molecular constants were determined using an iterative computer simulation technique. Accurate rotational constants could not be determined by this method since a ground state equilibrium bond length had to be assumed for YBr to perform the calculations.

This chapter reports the first high resolution spectroscopic study of yttrium monobromide and the first measurement of the ^{19}F nuclear spin-rotation splitting in the spectrum of yttrium monofluoride. Transitions for both molecules have been measured in the ground and first excited vibrational states. Rotational constants, B_0 and B_1, have been determined for both isotopomers of YBr and from these the equilibrium bond length has been calculated. Equilibrium vibrational parameters have also been estimated. Nuclear quadrupole and nuclear spin-rotation hyperfine structure have been observed and coupling constants have been determined for YBr. By combining the FTMW results with data from other microwave studies, the nuclear spin-rotation constant of YF has been determined.

8.2 Experimental Details

The gas phase yttrium monobromide and yttrium monofluoride samples were prepared by reacting ablated Y metal (rod from Goodfellow 99.9%) with either bromine or sulfur hexafluoride, present as 0.05-0.1% in Ar carrier gas. The strongest transitions were seen easily with a few averaging cycles.

8.3 Spectral Search and Assignment

8.3.1 YF

Yttrium monofluoride has only one isotopomer, $^{89}Y^{19}F$, and both ^{89}Y and ^{19}F have a nuclear spin of $\frac{1}{2}$. Only the lowest rotational transition, $J = 1 - 0$ near 17.3 GHz, was available in the frequency range of the spectrometer. This transition was measured in both the ground and first excited vibrational states. The $v = 0$ transition frequency was predicted using the millimetre wave results of Shirley *et al.* [172]; this value was within 100 kHz of the observed frequency. Following this, the results of Kaledin *et al.* [169,170] were used to predict the $v = 1$ transition; it was found within 60 kHz. Nuclear spin-rotation splitting due to the ^{19}F nucleus was observed in the measured transitions; this is shown in Fig. 8.1. Splitting due to the ^{89}Y nucleus, however, was not seen. This is not surprising because the magnitude of the magnetic moment of ^{89}Y is almost 20 times smaller than that of ^{19}F and also nuclear spin-rotation splitting due to ^{89}Y had not been observed in the FTMW study of the similar species YCl [56]. The frequencies of the measured hyperfine components and their assignments are listed in Table 8.1.

8.3.2 YBr

No previous high resolution spectroscopic measurements had been made of yttrium monobromide, so accurate rotational constants were not available to facilitate the search. The laser-induced fluorescence results of Fischell *et al.* [175] could not be used to predict the initial search parameters since the ground state rotational constants were not sufficiently accurate. So, the initial search parameters were calculated using the theoretical results of Langhoff *et al.* [157]. The uncertainty in the bond length was estimated by comparing their calculated r_e for YCl with that obtained experimentally by Simard *et al.* [181]. Nuclear quadrupole coupling constants for each of the bromine nuclei, ^{79}Br and ^{81}Br (both

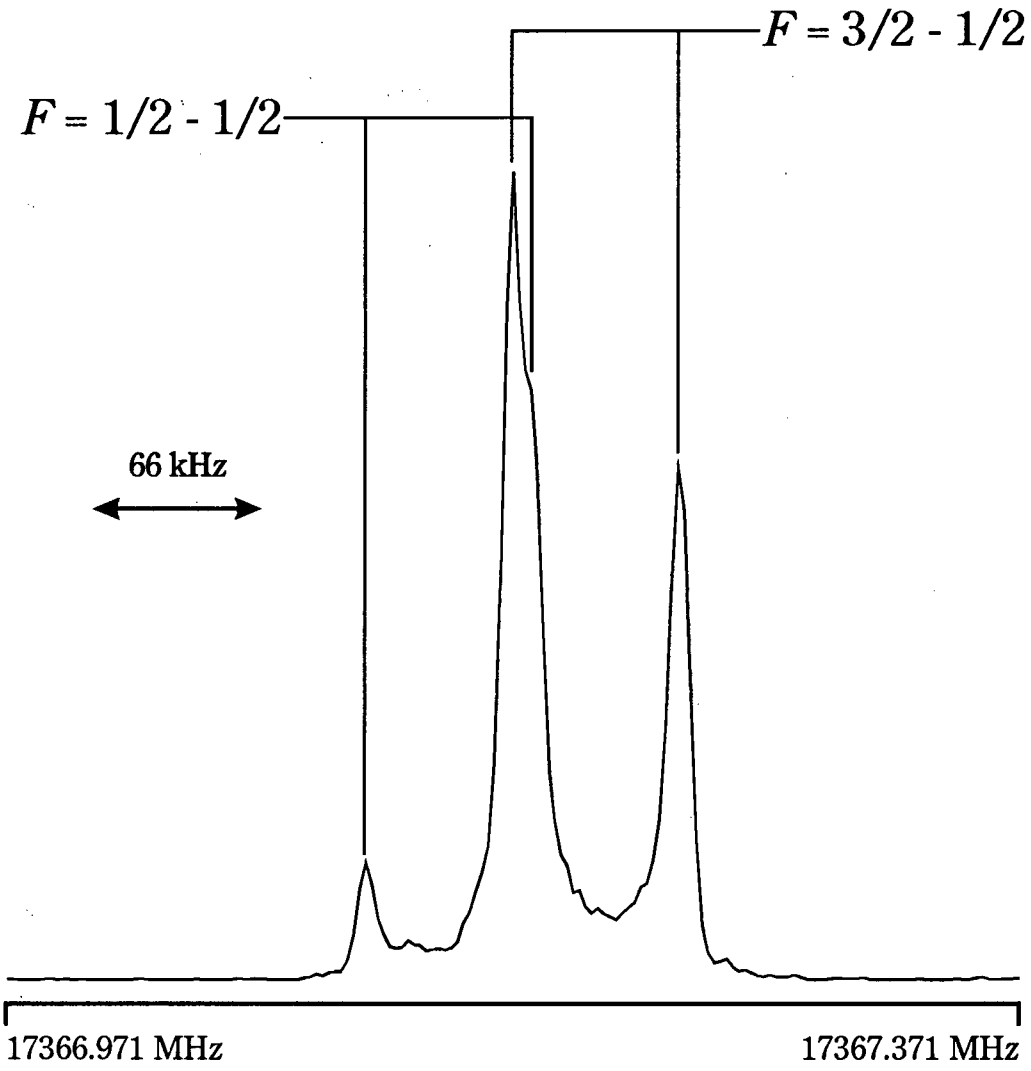

Figure 8.1: The $J = 1 - 0$ rotational transition of YF. The nuclear spin-rotation splitting observed is due to the ^{19}F nucleus. This spectrum was obtained with 100 averaging cycles. The microwave excitation frequency was 17367.171 MHz. 4 K data points were measured with a 50 ns sampling interval and the power spectrum is displayed as an 8 K transformation.

isotopes have $I = \frac{3}{2}$) were estimated using results obtained for KBr [125].

Five rotational transitions, $J = 2 - 1$ to $J = 6 - 5$, were available in the frequency range of the spectrometer. The initial search range was calculated for the $J = 2 - 1$ transition; a line was found within 10 MHz of the prediction. The assignment was made by observing transitions due to both isotopomers, $Y^{79}Br$ and $Y^{81}Br$, which have almost equal natural abundance (50.69% and 49.31%, respectively) and was verified by prediction and measurement of higher J transitions. The measured transition frequencies for $Y^{79}Br$ and $Y^{81}Br$ in the ground vibrational state are listed in Tables 8.2 and 8.3, respectively. The hyperfine structure observed was due only to the bromine nucleus. As was found for YF and YCl, splitting due to yttrium ($I = \frac{1}{2}$) spin-rotation interaction could not be resolved. The rotational transitions of YBr in the $v = 1$ vibrationally excited state were predicted by estimating the vibration-rotation constant α_e. This was done by comparing the values of α_e for AlF, AlCl and AlBr [184] with those of YF [170] and YCl [181]. This method proved to be quite accurate as the $J = 2 - 1$ rotational transitions in the first excited vibrational state were found within 5 MHz of the predicted values. The observed transition frequencies for $Y^{79}Br$ and $Y^{81}Br$ in the $v = 1$ state are also listed in Tables 8.2 and 8.3, respectively.

8.4 Analyses

8.4.1 YF

The results obtained in this study were used alone and in combination with the results of other pure rotational studies to determine molecular constants of YF. First, the nuclear spin-rotation constants for each vibrational level were calculated directly from the measured transitions; these calculations are referred to below as the direct calculation.

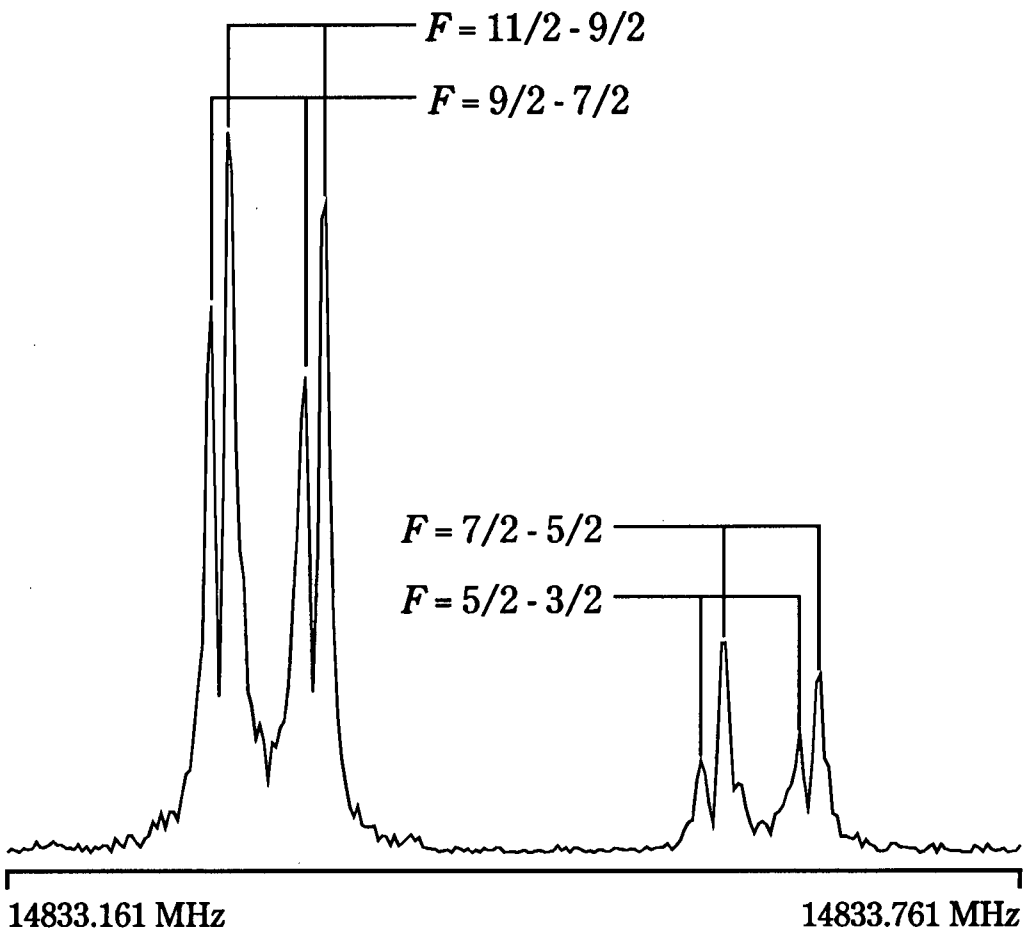

Figure 8.2: The $\Delta F = +1$ hyperfine components of the $J = 4 - 3$ transition of $Y^{81}Br$. 50 averaging cycles were co-added to obtain this spectrum. The excitation frequency was 14833.461 MHz. 4 K data points were recorded and this power spectrum was obtained with an 8 K transformation.

The nuclear spin-rotation contribution to the molecular energy is given by Eq. (2.49):

$$E_{\text{spin-rot.}} = \frac{C_I}{2}[F(F+1) - J(J+1) - I(I+1)].$$

This expression was used to relate the energy difference between the measured hyperfine components in each vibrational level to the nuclear spin-rotation constant, C_I and the hypothetical unsplit frequency, ν. The results are listed in Table 8.4. The C_I values are equal within the calculated uncertainties and indicate that the vibrational dependence of the nuclear spin-rotation constants is less than the estimated error.

A full fit could only be made by combining data from another study with the present results because only one rotational transition was measured in the FTMW study. The $J = 2 - 1$ and $J = 3 - 2$ transitions obtained in the pump/probe microwave-optical double resonance (PPMODR) study [173] were employed with the $v = 0$ FTMW results to calculate ground vibrational state parameters. The PPMODR transitions were treated as overlapped hyperfine components and were fit as blended lines using the predicted intensities as weighting factors. The rotational constant, B_0, the centrifugal distortion constant, D_0, and the ^{19}F nuclear spin-rotation coupling constant, C_I, were determined using Pickett's exact fitting program SPFIT. A relative weighting of 9:1 was given to the FTMW lines with respect to the other pure rotational data; this ratio was obtained from the estimated measurement uncertainties. The constants determined are listed in Table 8.5 under the heading Combined Fit. Values of $C_I(v = 0)$ and B_0 obtained from the direct calculation are listed under the heading Direct Calculation; the B_0 quoted for the direct calculation was obtained from the hypothetical unsplit frequency by fixing D_0 at the value from the PPMODR study. Also listed are the B_0 and D_0 values from the PPMODR study [173]. The rotational constant and the ^{19}F nuclear spin-rotation coupling constant from the combined fit compare quite well with those determined by direct calculation. However, the B_0 and D_0 results from the combined fit do not compare

as well with those obtained from the PPMODR study; neither constant is within three standard deviations.

One source of this difference could be shifts in the spectrum due to partially resolved hyperfine splitting; the $J = 1 - 0$ transition listed in the PPMODR study is within 3 kHz of the $J = 1 - 0$ $F = 3/2 - 1/2$ component measured in this study. To test this possibility, the PPMODR results were fit alone. These were not treated as blended lines; the frequencies were assigned to the most intense hyperfine component of each transition. B_0 and D_0 were determined while C_I was held fixed at the value of $C_I(v = 0)$ determined by direct calculation. The results are listed in Table 8.5 under the heading PPMODR Refit. The calculated constants agree much better with those of the combined fit; B_0 and D_0 are within two standard deviations. It appears that the discrepancy between the B_0 obtained using the FTMW results (either in the combined fit or direct calculation) and the published PPMODR results are most likely due to partially resolved hyperfine effects. [1]

Finally, a fit using the FTMW data and the millimetre wave optical pump/probe data [172] was attempted. Unfortunately, this did not prove fruitful because there was some difficulty in producing observed minus calculated values that were in the range of the estimated measurement uncertainties. A similar difficulty had been found in the PPMODR study; a slight discrepancy was found between the constants obtained in the millimetre wave study [172] and those of the PPMODR study [173]. Poor calibration of the millimetre wave source was suggested as a possible source of this difference [173].

[1] It was also noted that the molecular constants reported in the PPMODR study do not reproduce the reported transition frequencies well. A refit of the reported lines produces B_0 and D_0 constants which are within three standard deviations of those listed in the PPMODR paper. However, this difference in constants is about one third of the difference between the combined fit and the reported PPMODR constants so hyperfine effects in the PPMODR results appear to be still significant.

8.4.2 YBr

The frequencies obtained for each isotopomer of YBr in each vibrational state were fit separately using Pickett's non-linear least squares fitting program SPFIT [76]. In each fit, the rotational constant, B, and centrifugal distortion constant, D, were determined along with the hyperfine parameters for the bromine nuclei, the nuclear quadrupole coupling constant, eQq(Br), and the nuclear spin-rotation constant, C_I(Br). The obtained parameters are listed in Table 8.6. There are no previous rotationally resolved studies with which to compare these results; however, the isotopic ratios of the hyperfine parameters should provide a reasonable comparison.

The ratios of the hyperfine parameters of the two isotopomers of yttrium monobromide, $Y^{79}Br$ and $Y^{81}Br$, should be equal to the ratios of certain molecular and nuclear properties. This method is identical to that employed in Sec. 6.4 for MgBr and AlBr. The ratio of the eQq(Br) and C_I(Br) constants are equal to the ratio of the electric quadrupole moments and the nuclear magnetic moments of the bromine nuclei, respectively. The ratio of the nuclear spin-rotation constants also depends on the inverse ratio of the reduced masses. The ratios of the hyperfine parameters have been calculated for both the $v = 0$ and $v = 1$ vibrational states and are listed in Table 8.7. Also listed are the ratios of the appropriate nuclear and molecular parameters calculated from data taken from Ref. 120. The nuclear spin-rotation constants were not very well determined; however, the ratios agree well with the literature value, within the large estimated uncertainty. The ratios of the nuclear quadrupole coupling constants do not agree quite as well. There appears to be a small deviation in the ratio obtained for the $v = 0$ constants. Strictly, the ratios of the nuclear and molecular properties are equal to the ratio of the equilibrium hyperfine parameters [117,118]. As was done for MgBr and AlBr, the vibrational dependence of the nuclear quadrupole coupling constants was calculated using an

expansion in terms of the vibrational contribution:

$$eQq_v = eQq_e + eQq_1\left(v+\frac{1}{2}\right) \tag{8.1}$$

where eQq_e is the equilibrium nuclear quadrupole coupling constant and eQq_1 is the vibration-rotation correction term. The vibrational dependence of the nuclear quadrupole coupling constants can be summarised by the following expressions,

$$\begin{aligned} eQq_v(^{79}\mathrm{Br}) &= 12.2354(29) + 1.3997(48)\left(v+\frac{1}{2}\right) \\ eQq_v(^{81}\mathrm{Br}) &= 10.2184(29) + 1.1666(48)\left(v+\frac{1}{2}\right). \end{aligned}$$

The ratio of the equilibrium nuclear quadrupole coupling constants is listed in Table 8.7. This value agrees more closely with the literature value than the result obtained of the $v = 0$ parameters. Evidently there is a small vibrational dependence of the nuclear quadrupole coupling constants.

8.5 Discussion

8.5.1 Equilibrium Bond Distance of YBr

The same procedure was used to estimate the equilibrium bond distance of yttrium monobromide as was used for magnesium monobromide in Sec. 6.5.1. The vibrational dependence of the rotational constant, B, can be expressed in terms of the equilibrium rotational constant, B_e, and the vibration-rotation constants, α_e and γ_e using Eq. (2.16) which is repeated here for convenience,

$$B_v = B_e - \alpha_e\left(v+\frac{1}{2}\right) + \gamma_e\left(v+\frac{1}{2}\right) + \ldots$$

This expression was employed in three calculations to estimate the equilibrium rotational constant and the equilibrium bond distance of YBr. For the first calculation, Eq. (2.16)

was truncated following the α_e term. B_e and α_e were calculated directly from B_0 and B_1 and r_e was calculated from B_e using atomic masses and fundamental constants from Ref. 120. The values of B_e, α_e and r_e obtained are listed in Table 8.8 under the heading Method I. The difference in r_e values obtained for the two isotopomers is within the calculated uncertainty and is most likely due to the uncertainties of the masses, which are greater than those of the rotational constants. For the second calculation, an estimate was made for the higher order vibration-rotation contribution. The value of γ_e was estimated as $10^{-3} \cdot \alpha_e$ by comparisons with KBr [185] and RbBr [186]. B_e was determined by including the estimated γ_e value in the calculation and thus a second value of r_e was obtained. These results are listed in Table 8.8 under the heading Method II. The calculated uncertainty in r_e is derived only from the uncertainties in the rotational constants, fundamental constants and masses used in the calculation. The difference between the r_e value determined by this method and that calculated by Method I is of the order of 10^{-6}Å.

In these two calculations no attempt was made to take account of electronic effects. A description of these effects can be found in Sec. 2.4. To estimate the magnitude of the effects due to non-spherical charge distribution, yttrium monobromide was considered to be the completely ionic species Y^+Br^-. This provides a third estimate of the equilibrium bond distance of YBr. B_e and α_e were calculated just as they were in Method II and then r_e was determined using a reduced mass calculated using ion masses instead of atomic masses. The resulting values are listed in Table 8.8 under the heading Method III. The equilibrium bond distances calculated by Method II and Method III differ by only 10^{-6}Å, which is on the order of the estimated uncertainty of r_e. This small change was not unexpected, since the masses of Y and Br are much greater than the mass of

an electron. A reasonable upper limit for the deviation of r_e from that in the Born-Oppenheimer approximation is $\sim 10^{-5}$ Å, as was found for MgBr and AlBr in Sec. 6.5.1. Table 8.9 presents the equilibrium bond distances calculated by each method and an average of all three values. Also listed are the value calculated in the theoretical study by Langhoff *et al.* [157] and the assumed value from the laser-induced fluorescence study by Fischell *et al.* [175] for comparison. The result from the present study is the first accurate determination of the equilibrium bond distance of yttrium monobromide.

8.5.2 Estimate of Vibration Frequency

The vibration frequency, ω_e, and the anharmonicity constant, $\omega_e x_e$, of YBr can be estimated using the relations developed by Kratzer [187] and Pekeris [15], respectively,

$$\omega_e = \sqrt{\frac{4B_e^3}{D_e}} \tag{8.2}$$

$$\omega_e x_e = B_e \left(\frac{\alpha_e \omega_e}{6B_e^2} + 1 \right)^2 \tag{8.3}$$

where B_e and D_e are the equilibrium rotational and centrifugal distortion constants and α_e is the vibration-rotation constant. Though these expressions are exact only for a Morse potential function, they do provide a reasonable estimate of the desired constants. An estimate of the uncertainty in the calculated values was obtained by determining ω_e and $\omega_e x_e$ from Eqs. (8.2) and (8.3) for YF and YCl using the molecular constants in Refs. 169 and 176, respectively. The percentage differences between the experimentally determined ω_e and $\omega_e x_e$ values and those calculated using the Kratzer and Pekeris relations are $\sim 0.5\%$ and $\sim 6\%$, respectively. The ω_e and $\omega_e x_e$ parameters were calculated for both $Y^{79}Br$ and $Y^{81}Br$ and are listed in Table 8.10. In the calculations, D_e was approximated as D_0, since the centrifugal distortion constants are not sufficiently well determined to calculate the vibrational dependence. B_e values from Method I and Method II (see Sec.

8.5.1) produced identical ω_e and $\omega_e x_e$ values, within the number of significant figures given. Vibration frequency and anharmonicity constant values determined in the laser-induced fluorescence study [175] and the theoretical study of Langhoff *et al.* [157] are also listed in Table 8.10. These values are for an unspecified isotopomer because features due to the individual species could not be resolved. The ω_e and $\omega_e x_e$ results from Fischell *et al.* [175] compare reasonably well with those derived from the FTMW results.

8.5.3 YBr Nuclear Quadrupole Coupling Constants

The ionic character of the Y-Br bond can be estimated from the bromine nuclear quadrupole coupling constant, $eQq(\mathrm{Br})$ using Eq. (2.71), which is repeated here for reference

$$i_c = 1 + \frac{eQq(\mathrm{Br})}{eQe_{410}(\mathrm{Br})}$$

The derivation of this expression is found in Sec. 2.5. The ionic character calculated for YBr is listed in Table 8.11 along with the bromine nuclear quadrupole coupling constants and calculated ionic characters of several related alkali metal bromides. All four compounds are very ionic and it can be seen by comparing the values of i_c that YBr is very similar in ionicity to the alkali metal bromides. A similar result has also been found for YCl [56].

8.6 Conclusion

The first high resolution study of the spectra of $Y^{79}Br$ and $Y^{81}Br$, and the first measurement of the nuclear spin-rotation structure for yttrium monofluoride, have been made by FTMW spectroscopy. Accurate rotational constants have been determined for yttrium monobromide and have been used to obtain an accurate equilibrium bond length. Nuclear quadrupole hyperfine parameters have been determined and used to compare

the ionic character of the Y-Br bond to that of the alkali metal bromides. Through a series of fits, the ^{19}F nuclear spin-rotation coupling constant of yttrium monofluoride has been determined. Discrepancies between the results of this study and those of other pure rotational studies have been investigated. The source of these discrepancies appears to be partially resolved hyperfine structure.

Table 8.1: Observed transitions of YF in the $v = 0$ and $v = 1$ vibrational states in MHz.

v'	J'	F'	v''	J''	F''	Observed Frequency[a,b]
0	1	3/2	0	0	1/2	17367.2044(−7)
0	1	1/2	0	0	1/2	17367.1450(−4)
1	1	3/2	1	0	1/2	17269.2718
1	1	1/2	1	0	1/2	17269.2128
0	1		0	0		17367.202
0	2		0	1		34734.210(8)
0	3		0	2		52100.882(−2)

[a] Results for hyperfine transitions are from present study. Other data taken from PPMODR study [173].

[b] Observed minus calculated frequencies from combined fit in parentheses, in units of least significant digit. Constants obtained in fit are listed in Table 8.5 under heading Combined Fit.

Table 8.2: Measured transition frequencies of $Y^{79}Br$ in $v = 0$ and $v = 1$ vibrational states.

Transition				$v = 0$	Obs. - calc.	$v = 1$	Obs. - calc.
J'	F'	J''	F''	/MHz	/kHz	/MHz	/kHz
2	3/2	1	3/2	7512.3489	0.9	7488.7459	0.4
2	5/2	1	3/2	7514.6779	-0.3	7491.3247	-1.2
2	7/2	1	5/2	7514.6873	0.3	7491.3357	0.9
2	1/2	1	1/2	7514.9342	0.2		
2	5/2	1	5/2	7517.8909	-0.0		
2	3/2	1	1/2	7518.1816	0.0		
3	3/2	2	3/2	11269.7894	0.4		
3	5/2	2	5/2	11270.7146	0.2	11235.5503	-0.1
3	7/2	2	5/2	11272.2519	-0.9	11237.2520	-0.7
3	9/2	2	7/2	11272.2621	0.7	11237.2619	0.4
3	3/2	2	1/2	11273.0349	-1.7	11238.1228	0.0
3	5/2	2	3/2	11273.0451	0.5	11238.1317	0.9
3	7/2	2	7/2	11275.4572	0.4		
4	5/2	3	5/2	15026.8330	-0.5		
4	7/2	3	7/2	15028.5591	-0.0		
4	9/2	3	7/2	15029.7309	-0.2	14983.0760	-0.2
4	11/2	3	9/2	15029.7399	0.2	14983.0846	-0.4
4	5/2	3	3/2	15030.0878	-1.3	14983.4736	-0.8
4	7/2	3	5/2	15030.0983	0.8	14983.4836	0.6
4	9/2	3	9/2	15032.9269	0.5		
5	11/2	4	9/2	18787.1446	-0.3	18728.8319	-0.7
5	13/2	4	11/2	18787.1537	0.2	18728.8420	0.6
5	7/2	4	5/2	18787.3489	-0.6	18729.0613	0.4
5	9/2	4	7/2	18787.3589	0.9	18729.0696	0.0
6	13/2	5	11/2	22544.4988	0.6		
6	15/2	5	13/2	22544.5062	-0.6		

Table 8.3: Measured transition frequencies of $Y^{81}Br$ in $v = 0$ and $v = 1$ vibrational states.

Transition				$v = 0$	Obs. - calc.	$v = 1$	Obs. - calc.
J'	F'	J''	F''	/MHz	/kHz	/MHz	/kHz
2	3/2	1	3/2	7414.5535	0.5	7391.4534	-0.2
2	5/2	1	3/2	7416.5039	-0.1	7393.6124	-0.4
2	7/2	1	5/2	7416.5134	0.1	7393.6220	-0.2
2	1/2	1	1/2	7416.7116	-0.9		
2	5/2	1	5/2	7419.1812	-0.5		
2	3/2	1	1/2	7419.4271	-0.3		
3	3/2	2	3/2	11122.8849	0.5		
3	5/2	2	5/2	11123.6571	0.1	11089.2082	0.5
3	7/2	2	5/2	11124.9487	-0.1	11090.6353	-0.3
3	9/2	2	7/2	11124.9581	0.1	11090.6452	0.3
3	3/2	2	1/2	11125.5978	-1.5	11091.3577	-0.5
3	5/2	2	3/2	11125.6091	1.1	11091.3679	1.0
3	7/2	2	7/2	11127.6178	0.6		
4	5/2	3	5/2	14830.8801	-0.5		
4	7/2	3	7/2	14832.3215	0.1		
4	9/2	3	7/2	14833.3086	-0.6	14787.5673	-0.7
4	11/2	3	9/2	14833.3188	0.4	14787.5776	0.4
4	5/2	3	3/2	14833.6036	-0.5	14787.8963	-0.4
4	7/2	3	5/2	14833.6135	0.3	14787.9060	0.3
4	9/2	3	9/2	14835.9692	0.8		
5	11/2	4	9/2	18541.6102	-0.2	18484.4390	0.2
5	13/2	4	11/2	18541.6201	0.5	18484.4477	-0.3
5	7/2	4	5/2	18541.7764	-0.9	18484.6248	-0.8
5	9/2	4	7/2	18541.7873	0.9	18484.6356	0.9
6	13/2	5	11/2	22249.8551	0.7		
6	15/2	5	13/2	22249.8626	-1.0		

Table 8.4: Molecular constants obtained by direct calculation for YF in MHz.

Parameter	Value[a]
ν_0[b]	17367.1846(13)
ν_1[b]	17269.2521(13)
$C_I(v=0)$	0.0396(9)
$C_I(v=1)$	0.0393(9)

[a] Error estimated from measurement uncertainty in parentheses.
[b] ν_v is the hypothetical unsplit $J = 1 - 0$ frequency of the vth vibrational state.

Table 8.5: Ground vibrational state molecular constants determined for YF in MHz.

Parameter	Direct Calc.[a,b]	Combined Fit[c]	PPMODR Refit[c,d]	PPMODR Lit.[c,e]
B_0	8683.60734(67)	8683.60658(41)	8683.6045(11)	8683.6156(11)
D_0	[0.007521]	0.006996(39)	0.007086(72)	0.007521(74)
C_I	0.0396(9)	0.03983(94)	[0.0396]	

[a] B_0 determined from hypothetical unsplit frequency ν_0 using D_0 from PPMODR study [173].
[b] Error estimated from measurement uncertainty in parentheses.
[c] One standard deviation in parentheses, in units of the least significant digit.
[d] Fit of three lines from PPMODR study, assigning each line as the most intense hyperfine component in each rotational transition. C_I was held fixed at the value determined in the $v = 0$ direct calculation.
[e] Taken from PPMODR study of Fletcher *et al.* [173].

Table 8.6: Molecular constants calculated for YBr in MHz[a].

Parameter	$Y^{79}Br$		$Y^{81}Br$	
	$v = 0$	$v = 1$	$v = 0$	$v = 1$
B	1878.741007(71)	1872.910362(97)	1854.185861(71)	1848.469305(97)
D	0.0004033(15)	0.0004004(25)	0.0003923(15)	0.0003923(25)
eQq(Br)	12.9352(16)	14.3349(45)	10.8017(16)	11.9683(45)
C_I(Br)	0.00858(12)	0.00877(20)	0.00918(12)	0.00921(20)

[a] One standard deviation in parentheses, in units of least significant digit.

Table 8.7: Calculated ratios of hyperfine parameters compared to nuclear and molecular properties of YBr.

	v=0	v=1	Eq.[a]	Lit.
$eQq(^{79}\mathrm{Br})/eQq(^{81}\mathrm{Br})$	1.1975(2)	1.1977(6)	1.1974(4)	1.19707(3)[b]
$C_I(^{79}\mathrm{Br})/C_I(^{81}\mathrm{Br})$	0.935(18)	0.952(30)	-	0.939995(2)[c]

[a] For method of calculation, see text Sec. 8.4.2.
[b] Ratio of electric quadrupole moments of ^{79}Br and ^{81}Br, taken from Ref. 2.
[c] Ratio of nuclear magnetic moments of ^{79}Br and ^{81}Br multiplied by inverse ratio of reduced masses of Y^{79}Br and Y^{81}Br, calculated using values in Ref. 120.

Table 8.8: Equilibrium parameters calculated for YBr[a,b].

Method I	$Y^{79}Br$	$Y^{81}Br$
B_e/MHz	1881.65633(9)	1857.04414(9)
α_e/MHz	5.83065(12)	5.71656(12)
r_e/Å	2.534613(1)	2.534612(1)
Method II	$Y^{79}Br$	$Y^{81}Br$
B_e/MHz	1881.64906(9)	1857.03701(9)
α_e/MHz	5.81901(12)	5.70515(12)
r_e/Å	2.534618(1)	2.534617(1)
Method III	$Y^{79}Br$	$Y^{81}Br$
B_e/MHz	1881.64906(9)	1857.03701(9)
α_e/MHz	5.81901(12)	5.0515(12)
r_e/Å	2.534617(1)	2.534616(1)

[a] For methods of calculation, see Sec. 8.5.1.
[b] Estimated uncertainties in parentheses, in units of least significant digit, derived from rotational constants, fundamental constants and reduced masses.

Table 8.9: Summary of equilibrium bond length estimates for YBr[a].

	Method I[b]	Method II[b]	Method III[b]	Ave.[c]	Lit. Theo.	Lit. LIF
r_e/Å	2.534613(1)	2.534618(1)	2.534617(1)	2.53462	2.605[d]	2.800[e]

[a] For description of methods see Sec. 8.5.1.
[b] Estimated uncertainties in parentheses, in units of least significant digit, derived from rotational constants, fundamental constants and reduced masses.
[c] Average of values obtained by three methods. The deviation of r_e from that obtained in the Born-Oppenheimer approximation is estimated to be on the order of 10^{-5} Å.
[d] r_e from Ref. 157.
[e] Value of r_e used in laser fluorescence study [175].

Table 8.10: Estimate of vibration frequency of YBr.

	$Y^{79}Br^{a,b}$	$Y^{81}Br^{a,b}$	Lit. Expt.[c]	Lit Theo.[d]
ω_e/cm^{-1}	271.1	269.5	268(2)	259
$\omega_e x_e/cm^{-1}$	0.66	0.65	0.8(2)	

[a] For description of calculations see Sec. 8.5.2.
[b] Uncertainties in ω_e and $\omega_e x_e$ are estimated to be $\sim 0.5\%$ and $\sim 6\%$, respectively.
[c] Results taken from Ref. 175. Features due to each of the isotopomers of YBr could not be resolved.
[d] Taken from Ref. 157.

Table 8.11: Calculated ionic character of $Y^{79}Br$ and related alkali metal bromides.

	$Y^{79}Br$	$^{23}Na^{79}Br$[a]	$^{39}K^{79}Br$[b]	$^{85}Rb^{79}Br$[c]
$eQq(^{79}Br)$/MHz	12.935	58.60801	10.2383	3.50
i_c/%	98.3	92.5	98.7	99.5

[a] Results taken from Ref. 124.
[b] Results taken from Ref. 125.
[c] Results taken from Ref. 188.

Bibliography

[1] C. H. Townes and A. L. Schawlow, *Microwave Spectroscopy* (Dover Publications, New York, 1975).

[2] W. Gordy and R. L. Cook, *Microwave Molecular Spectra*, No. XVIII in *Techniques of Chemistry*, 3rd ed. (John Wiley & Sons, New York, 1984), .

[3] Landolt-Börnstein, edited by W. Hüttner (Springer-Verlag, Berlin, 1967, 1974, 1982, 1992), Vol. II/4, II/6, II/14, II/19.

[4] G. Winnewisser, E. Herbst, and H. Ungerechts, in *Spectroscopy of the Earth's Atmosphere and Interstellar Medium*, edited by K. N. Rao and A. Weber (Academic Press, London, 1992), pp. 423–517.

[5] A. Omont, J. Chem. Soc. Faraday Trans. **89**, 2137 (1993).

[6] B. E. Turner, Astrophys. Space Sci. **224**, 297 (1995).

[7] E. Herbst, Ann. Rev. Phys. Chem. **46**, 27 (1995).

[8] T. J. Balle, E. J. Campbell, M. R. Keenan, and W. H. Flygare, J. Chem. Phys. **71**, 2723 (1979).

[9] T. J. Balle and W. H. Flygare, Rev. Scient. Instrum. **52**, 33 (1981).

[10] H. Dreizler, Mol. Phys. **59**, 1 (1986).

[11] J. R. Morton, Chem. Rev. **64**, 453 (1964).

[12] E. Hirota, *High-Resolution Spectroscopy of Transient Molecules*, Vol. 40 of *Springer Series in Chemical Physics* (Springer-Verlag, Berlin, 1985), .

[13] H. W. Kroto, *Molecular Rotation Spectra*, 2nd ed. (Dover Publications, New York, 1992).

[14] P. M. Morse, Phys. Rev. **34**, 57 (1929).

[15] C. L. Pekeris, Phys. Rev. **45**, 98 (1934).

[16] R. N. Zare, *Angular Momentum* (John Wiley and Sons, New York, 1988).

[17] C. H. Townes and B. P. Dailey, J. Chem. Phys. **17**, 782 (1949).

[18] Ch. Ryzlewicz, H.-U. Schütze-Pahlmann, J. Hoeft, and T. Törring, Chem. Phys. **71**, 389 (1982).

[19] T. A. Dixon and R. C. Woods, J. Chem. Phys. **67**, 3956 (1977).

[20] R. A. Frosch and H. M. Foley, Phys. Rev. **88**, 1337 (1952).

[21] W. Weltner, Jr., *Magnetic Atoms and Molecules* (Van Nostrand, New York, 1983).

[22] J. R. Morton and K. F. Preston, J. Magn. Reson. **30**, 577 (1978).

[23] N. F. Ramsey, *Molecular Beams* (Oxford University, London, 1956).

[24] T. R. Dyke and J. S. Muenter, in *Molecular Structure and Properties*, Vol. 2 of *International Review of Science, Physical Chemistry, Series 2*, edited by A. D. Buckingham (Butterworth and Co., London, 1975), pp. 27–92.

[25] C. Schlier, Fortschr. Phys. **9**, 455 (1961).

[26] C. Styger and M. C. L. Gerry, J. Mol. Spectrosc. **158**, 328 (1993).

[27] C. C. Costain, J. Chem. Phys. **29**, 864 (1958).

[28] J. H. Van Vleck, J. Chem. Phys. **4**, 327 (1936).

[29] B. Rosenblum, A. H. Nethercot, Jr., and C. H. Townes, Phys. Rev. **109**, 400 (1958).

[30] F. C. De Lucia, P. Helminger, and W. Gordy, Phys. Rev. A **3**, 1849 (1971).

[31] P. R. Bunker, J. Mol. Spectrosc. **35**, 306 (1970).

[32] P. R. Bunker, J. Mol. Spectrosc. **68**, 367 (1977).

[33] J. K. G. Watson, J. Mol. Spectrosc. **45**, 99 (1973).

[34] J. K. G. Watson, J. Mol. Spectrosc. **80**, 411 (1980).

[35] W. Gordy, Faraday Discuss. Chem. Soc. **19**, 14 (1955).

[36] U. Fano, Revs. Modern Phys. **29**, 74 (1957).

[37] J. C. McGurk, T. G. Schmalz, and W. H. Flygare, Adv. Chem. Phys. **25**, 1 (1974).

[38] H. Dreizler, Ber. Bunsenges. Phys. Chem. **99**, 1451 (1995).

[39] J.-U. Grabow and W. Stahl, Z. Naturforsch. Teil A **45**, 1043 (1990).

[40] Y. Xu, W. Jäger, M. C. L. Gerry, and I. Merke, J. Mol. Spectrosc. **160**, 258 (1993).

[41] I. Merke and H. Dreizler, Z. Naturforsch. Teil A **43**, 196 (1988).

[42] J. Haekel and H. Mäder, Z. Naturforsch. Teil A **43**, 203 (1988).

[43] A. E. Derome, *Modern NMR Techniques for Chemistry Research* (Pergamon, Oxford, 1987).

[44] R. D. Suenram, F. J. Lovas, G. T. Fraser, and K. Matsumura, J. Chem. Phys. **92**, 4724 (1990).

[45] Y. Ohshima and Y. Endo, Chem. Phys. Lett. **213**, 95 (1993).

[46] K. D. Hensel and M. C. L. Gerry, J. Chem. Soc. Faraday Trans. **93**, 1053 (1997).

[47] A. H. Firester, Rev. Scient. Instrum. **37**, 1264 (1966).

[48] T. G. Dietz, M. A. Duncan, D. E. Powers, and R. E. Smalley, J. Chem. Phys. **74**, 6511 (1981).

[49] V. E. Bondybey and J. H. English, J. Chem. Phys. **74**, 6978 (1981).

[50] R. E. Smalley, Laser Chem. **2**, 167 (1983).

[51] R. D. Suenram, F. J. Lovas, and K. Matsumura, Astrophys. J. **342**, L103 (1989).

[52] R. D. Suenram, G. T. Fraser, F. J. Lovas, and C. W. Gillies, J. Mol. Spectrosc. **148**, 114 (1991).

[53] C. E. Blom, H. G. Hedderich, F. J. Lovas, R. D. Suenram, and A. G. Maki, J. Mol. Spectrosc. **152**, 109 (1992).

[54] K. D. Hensel, C. Styger, W. Jäger, A. J. Merer, and M. C. L. Gerry, J. Chem. Phys. **99**, 3320 (1993).

[55] R. J. Low, T. D. Varberg, J. P. Connelly, A. R. Auty, B. J. Howard, and J. M. Brown, J. Mol. Spectrosc. **161**, 499 (1993).

[56] K. D. Hensel and M. C. L. Gerry, J. Mol. Spectrosc. **166**, 304 (1994).

[57] C. T. Scurlock, T. C. Steimle, R. D. Suenram, and F. J. Lovas, J. Chem. Phys. **100**, 3497 (1994).

[58] Y. Kawashima, R. D. Suenram, and E. Hirota, J. Mol. Spectrosc. **175**, 99 (1996).

[59] N. M. Lakin, T. D. Varberg, and J. M. Brown, J. Mol. Spectrosc. **183**, 34 (1997).

[60] Y. Kawashima, Y. Ohshima, Y. Endo, and E. Hirota, J. Mol. Spectrosc. **174**, 279 (1995).

[61] F. J. Lovas, Y. Kawashima, J.-U. Grabow, R. D. Suenram, G. T. Fraser, and E. Hirota, Astrophys. J. **455**, L201 (1995).

[62] U. Kretschmer, D. Consalvo, A. Knaack, W. Schade, W. Stahl, and H. Dreizler, Mol. Phys. **87**, 1159 (1996).

[63] D. E. Powers, S. G. Hansen, M. E. Geusic, A. C. Puiu, J. B. Hopkins, T. G. Dietz, M. A. Duncan, P. R. R. Langridge-Smith, and R. E. Smalley, J. Phys. Chem. **86**, 2556 (1982).

[64] M. Barnes, M. M. Fraser, P. G. Hajigeorgiou, A. J. Merer, and S. D. Rosner, J. Mol. Spectrosc. **170**, 449 (1995).

[65] D. C. Morton, J. F. Drake, E. B. Jenkins, J. B. Rogerson, L. Spitzer, and D. G. York, Astrophys. J. **181**, L103 (1973).

[66] D. C. Morton, Astrophys. J. **193**, L35 (1974).

[67] B. E. Turner, Astrophys. J. **376**, 573 (1991).

[68] M. Guélin, J. Cernicharo, C. Kahane, and J. Gomez-Gonzalez, Astron. Astrophys. **157**, L17 (1986).

[69] K. Kawaguchi, E. Kagi, T. Hirano, S. Takano, and S. Saito, Astrophys. J. **406**, L39 (1993).

[70] J. H. Goebel and S. H. Moseley, Astrophys. J. **290**, L35 (1985).

[71] J. A. Nuth, S. H. Moseley, R. F. Silverberg, J. H. Goebel, and W. J. Moore, Astrophys. J. **290**, L41 (1985).

[72] B. Begemann, J. Dorschner, T. Henning, H. Mutschke, and E. Thamm, Astrophys. J. **423**, L71 (1994).

[73] S. Takano, S. Yamamoto, and S. Saito, Chem. Phys. Lett. **159**, 563 (1989).

[74] H. A. Wilhelm, Iowa State College J. Sci. **6**, 475 (1932).

[75] M. Marcano and R. F. Barrow, J. Chem. Soc. Faraday Trans. **65**, 2936 (1970).

[76] H. M. Pickett, J. Mol. Spectrosc. **148**, 371 (1991).

[77] L. B. Knight, Jr., W. C. Easley, and W. Weltner, Jr., J. Chem. Phys. **54**, 322 (1971).

[78] M. A. Anderson, M. D. Allen, and L. M. Ziurys, Astrophys. J. **425**, L53 (1994).

[79] M. A. Anderson, M. D. Allen, and L. M. Ziurys, J. Chem. Phys. **100**, 824 (1994).

[80] M. A. Anderson and L. M. Ziurys, Chem. Phys. Lett. **224**, 381 (1994).

[81] C. M. Olmsted, Zeitschr. f. wiss. Phot. **4**, 293 (1906).

[82] O. H. Walters and S. Barratt, Proc. R. Soc. London A **118**, 120 (1928).

[83] F. Morgan, Phys. Rev. **50**, 603 (1936).

[84] R. E. Harrington, Ph.D. thesis, University of California, 1942.

[85] S. N. Puri and H. Mohan, Curr. Sci. **43**, 442 (1974).

[86] B. R. K. Reddy and P. T. Rao, Curr. Sci. **39**, 509 (1970).

[87] V. M. Rao, M. L. P. Rao, and B. R. K. Reddy, J. Phys. B **15**, 4161 (1982).

[88] D. P. Nanda and B. S. Mohanty, Ind. J. Pure Appl. Phys. **18**, 324 (1980).

[89] N. E. Kuz'menko and L. V. Chumak, J. Quant. Spectrosc. Radiat. Transfer **35**, 419 (1986).

[90] R. G. Sadygov, J. Rostas, G. Taieb, and D. R. Yarkony, J. Chem. Phys. **106**, 4091 (1997).

[91] F. Fethi, Ph.D. thesis, Universite de Paris XI, 1995.

[92] M. M. Patel and P. D. Patel, J. Phys. B **2**, 515 (1969).

[93] D. R. Lide, Jr., J. Chem. Phys. **42**, 1013 (1965).

[94] F. Wyse, W. Gordy, and E. F. Pearson, J. Chem. Phys. **52**, 3887 (1970).

[95] J. Hoeft, F. J. Lovas, E. Tiemann, and T. Törring, Z. Naturforsch. Teil A **25**, 1029 (1970).

[96] R. Honerjäger and R. Tischer, Z. Naturforsch. Teil A **29**, 342 (1974).

[97] F. C. Wyse and W. Gordy, J. Chem. Phys. **56**, 2130 (1972).

[98] J. Hoeft, T. Törring, and E. Tiemann, Z. Naturforsch. Teil A **28**, 1066 (1973).

[99] F. H. Crawford and C. F. Ffolliott, Phys. Rev. **44**, 953 (1933).

[100] E. Miescher, Helv. Phys. Acta **8**, 279 (1935).

[101] E. Miescher, Helv. Phys. Acta **9**, 693 (1936).

[102] H. G. Howell, Proc. R. Soc. London A **148**, 696 (1935).

[103] P. C. Mahanti, Ind. J. Phys. **9**, 369 (1935).

[104] C. G. Jennergren, Nature **161**, 315 (1948).

[105] C. G. Jennergren, Ark. Mat. Astr. Fys. **35A**, 1 (1948).

[106] R. S. Ram, K. N. Upadhya, D. K. Rai, and J. Singh, Opt. Pura Apl. **6**, 38 (1973).

[107] R. S. Ram, Spectrosc. Lett. **9**, 435 (1976).

[108] W. B. Griffith, Jr. and C. W. Mathews, J. Mol. Spectrosc. **104**, 347 (1984).

[109] H. Bredohl, I. Dubois, E. Mahieu, and F. Melen, J. Mol. Spectrosc. **145**, 12 (1991).

[110] U. Wolf and E. Tiemann, Chem. Phys. **119**, 407 (1988).

[111] P. E. Fleming and C. W. Mathews, J. Mol. Spectrosc. **175**, 31 (1996).

[112] S. R. Langhoff, C. W. Bauschlicher, Jr., and P. R. Taylor, J. Chem. Phys. **88**, 5715 (1988).

[113] D. Sharma, Astrophys. J. **113**, 219 (1951).

[114] A. Lakshminarayana and P. B. V. Haranath, Curr. Sci. **39**, 228 (1970).

[115] H. Bredohl, P. Danguy, I. Dubois, E. Mahieu, and A. Saouli, J. Mol. Spectrosc. **151**, 178 (1992).

[116] H. Uehara, K. Horiai, Y. Ozaki, and T. Konno, Chem. Phys. Lett. **214**, 527 (1993).

[117] W. J. Childs, D. R. Cok, and L. S. Goodman, J. Chem. Phys. **76**, 3993 (1982).

[118] W. J. Childs, D. R. Cok, G. L. Goodman, and L. S. Goodman, J. Chem. Phys. **75**, 501 (1981).

[119] M. Bogey, C. Demuynck, and J. L. Destombes, Chem. Phys. Lett. **155**, 265 (1989).

[120] I. Mills, T. Cvitaš, K. Homann, N. Kallay, and K. Kuchitsu, *Quantities, Units and Symbols in Physical Chemistry*, 2nd ed. (Blackwell Science, Oxford, 1993).

[121] K. Möller, H.-U. Schütze-Pahlmann, J. Hoeft, and T. Törring, Chem. Phys. **68**, 399 (1982).

[122] S. Pfaffe, E. Tiemann, and J. Hoeft, Z. Naturforsch. Teil A **33**, 1386 (1978).

[123] E. Tiemann, M. Grasshoff, and J. Hoeft, Z. Naturforsch. Teil A **27**, 753 (1972).

[124] J. Cederberg, D. Nitz, A. Kolan, T. Rasmusson, K. Hoffman, and S. Tufte, J. Mol. Spectrosc. **122**, 171 (1987).

[125] F. H. de Leeuw, R. van Wachem, and A. Dymanus, J. Chem. Phys. **50**, 1393 (1969).

[126] L. W. Avery, M. B. Bell, C. T. Cunningham, P. A. Feldman, R. H. Hayward, J. M. MacLeod, H. E. Matthews, and J. D. Wade, Astrophys. J. **426**, 737 (1994).

[127] T. J. Millar, J. Elldér, Å. Hjalmarson, and H. Olofsson, Astron. Astrophys. **182**, 143 (1987).

[128] B. E. Turner, T. C. Steimle, and L. Meerts, Astrophys. J. **426**, L97 (1994).

[129] B. Ma, Y. Yamaguchi, and H. F. Schaefer III, Mol. Phys. **86**, 1331 (1995).

[130] J. Cernicharo and M. Guélin, Astron. Astrophys. **183**, L10 (1987).

[131] L. M. Ziurys, A. J. Apponi, and T. G. Phillips, Astrophys. J. **433**, 729 (1994).

[132] M. A. Anderson and L. M. Ziurys, Chem. Phys. Lett. **231**, 164 (1994).

[133] M. Guélin, M. Forestini, P. Valiron, L. M. Ziurys, M. A. Anderson, J. Cernicharo, and C. Kahane, Astron. Astrophys. **297**, 183 (1995).

[134] E. Kagi, K. Kawaguchi, S. Takano, and T. Hirano, J. Chem. Phys. **104**, 1263 (1996).

[135] D. E. Powers, M. Pushkarsky, and T. A. Miller, 50th Ohio State University International Symposium on Molecular Spectroscopy (1995), paper RJ12.

[136] R. Rubino, C. C. Carter, J. M. Williamson, D. E. Powers, and T. A. Miller, 51st Ohio State University International Symposium on Molecular Spectroscopy (1996), paper TF04.

[137] C. W. Bauschlicher, Jr., S. R. Langhoff, and H. Partridge, Chem. Phys. Lett. **115**, 124 (1985).

[138] K. Ishii, T. Hirano, U. Nagashima, B. Weis, and K. Yamashita, Astrophys. J. **410**, L43 (1993).

[139] K. Ishii, T. Hirano, U. Nagashima, B. Weis, and K. Yamashita, J. Mol. Struct. (THEOCHEM) **305**, 117 (1994).

[140] S. Petrie, J. Phys. Chem. **100**, 11581 (1996).

[141] T. Hirano, K. Takano, T. Kinoshita, K. Ishii, and K. Yamashita, 52nd Ohio State University International Symposium on Molecular Spectroscopy (1997), paper RB01.

[142] C. Barrientos and A. Largo, J. Mol. Struct. (THEOCHEM) **336**, 29 (1995).

[143] S. Petrie, J. Chem. Soc. Faraday Trans. **92**, 1135 (1996).

[144] K. Kawaguchi, Y. Kasai, S. Ishikawa, and N. Kaifu, Publ. Astron. Soc. Japan **47**, 853 (1995).

[145] K. A. Gingerich, Naturwiss. **54**, 646 (1967).

[146] C. Thomson, Int. J. Quantum Chem. Symp. **10**, 85 (1976).

[147] J. S. Robinson, A. J. Apponi, and L. M. Ziurys, Chem. Phys. Lett. **278**, 1 (1997).

[148] M. Fukushima, 52nd Ohio State University International Symposium on Molecular Spectroscopy (1997), paper MH09.

[149] R. Essers, J. Tennyson, and P. E. S. Wormer, Chem. Phys. Lett. **89**, 223 (1982).

[150] C. J. Whitham, B. Soep, J.-P. Visticot, and A. Keller, J. Chem. Phys. **93**, 991 (1990).

[151] M. Douay and P. F. Bernath, Chem. Phys. Lett. **174**, 230 (1990).

[152] J. J. van Vaals, W. L. Meerts, and A. Dymanus, Chem. Phys. **82**, 385 (1983).

[153] J. J. van Vaals, W. L. Meerts, and A. Dymanus, J. Mol. Spectrosc. **106**, 280 (1984).

[154] J. J. van Vaals, W. L. Meerts, and A. Dymanus, Chem. Phys. **86**, 147 (1984).

[155] M. A. Frerking, W. D. Langer, and R. W. Wilson, Astrophys. J. **232**, L65 (1979).

[156] S. R. Langhoff and C. W. Bauschlicher, Jr., Ann. Rev. Phys. Chem. **39**, 181 (1988).

[157] S. R. Langhoff, C. W. Bauschlicher, Jr., and H. Partridge, J. Chem. Phys. **89**, 396 (1988), ; S. R. Langhoff, C. W. Bauschlicher, Jr. and H. Partridge, J. Chem. Phys. **89**, 7649 (1988).

[158] C. J. Cheetham and R. F. Barrow, Adv. High Temp. Chem. **1**, 7 (1967).

[159] J. L. Gole, in *Electronic Transition Lasers II: Proceedings of the 3rd Summer Colloquium on Electronic Transition Lasers, Snowmass, Colo. 1976*, edited by L. E. Wilson, S. N. Suchard, and J. I. Steinfeld (M. I. T. Press, Cambridge, Mass., 1977), pp. 136–165.

[160] J. A. Gole and C. L. Chalek, in *Proceedings of the Symposium of High Temperature Metal Halide Chemistry*, edited by D. L. Hildenbrand and D. D. Cubicciotti (Electrochemical Society, Princeton, N.J., 1978), pp. 278–309.

[161] H. C. Brayman, D. R. Fischell, and T. A. Cool, J. Chem. Phys. **73**, 4247 (1980).

[162] R. F. Barrow and W. J. M. Gissane, Proc. Phys. Soc. **84**, 615 (1964).

[163] R. F. Barrow, M. W. Bastin, D. L. G. Moore, and C. J. Pott, Nature **215**, 1072 (1967).

[164] E. A. Shenyavskaya, A. A. Mal'tsev, and L. V. Gurvich, Opt. Spectrosk. **21**, 680 (1966).

[165] E. A. Shenyavskaya, A. A. Mal'tsev, and L. V. Gurvich, Vestn. Mosk. Univ., Ser. 2, Khim. **22**, 104 (1967).

[166] E. A. Shenyavskaya and R. B. Ryabov, J. Mol. Spectrosc. **63**, 23 (1976).

[167] E. A. Shenyavskaya and L. V. Gurvich, J. Mol. Spectrosc. **68**, 41 (1977).

[168] L. A. Kaledin and E. A. Shenyavskaya, Mol. Phys. **70**, 107 (1990).

[169] L. A. Kaledin and E. A. Shenyavskaya, Mol. Phys. **72**, 1203 (1991).

[170] L. A. Kaledin, J. E. McCord, M. C. Heaven, and R. F. Barrow, J. Mol. Spectrosc. **169**, 253 (1995).

[171] J. Shirley, C. Scurlock, T. Steimle, B. Simard, M. Vasseur, and P. A. Hackett, J. Chem. Phys. **93**, 8580 (1990).

[172] J. E. Shirley, W. L. Barclay, Jr., L. M. Ziurys, and T. C. Steimle, Chem. Phys. Lett. **183**, 363 (1991), ; J. E. Shirley, W. L. Barclay, Jr., L. M. Ziurys and T. C. Steimle, Chem. Phys. Lett. **191**, 378 (1992).

[173] D. A. Fletcher, K. Y. Jung, C. T. Scurlock, and T. C. Steimle, J. Chem. Phys. **98**, 1837 (1993).

[174] G. M. Janney, J. Opt. Soc. Am. **56**, 1706 (1966).

[175] D. R. Fischell, H. C. Brayman, and T. A. Cool, J. Chem. Phys. **73**, 4260 (1980).

[176] J. Xin, G. Edvinsson, and L. Klynning, J. Mol. Spectrosc. **148**, 59 (1991).

[177] J. Xin, G. Edvinsson, and L. Klynning, Physica Scripta. **47**, 75 (1993).

[178] J. Xin, G. Edvinsson, L. Klynning, and P. Royen, J. Mol. Spectrosc. **158**, 14 (1993).

[179] J. Xin and L. Klynning, J. Mol. Spectrosc. **175**, 217 (1996).

[180] J. Xin, L. Klynning, and P. Royen, J. Mol. Spectrosc. **176**, 1 (1996).

[181] B. Simard, A. M. James, and P. A. Hackett, J. Chem. Phys. **96**, 2565 (1992).

[182] A. Bernard, S. Roux, and J. Verges, J. Mol. Spectrosc. **80**, 374 (1980).

[183] A. Bernard and R. Gravina, Z. Naturforsch. Teil A **39**, 27 (1984).

[184] K. P. Huber and G. Herzberg, *Molecular Spectra and Molecular Structure IV. Constants of Diatomic Molecules* (Van Nostrand Reinhold, New York, 1979).

[185] B. P. Fabricand, R. O. Carlson, C. A. Lee, and I. I. Rabi, Phys. Rev. **91**, 1403 (1953).

[186] A. Honig, M. Mandel, M. L. Stitch, and C. H. Townes, Phys. Rev. **96**, 629 (1954).

[187] A. Kratzer, Z. Naturforsch. Teil A **3**, 289 (1920).

[188] E. Tiemann, B. Hölzer, and J. Hoeft, Z. Naturforsch. Teil A **32**, 123 (1977).